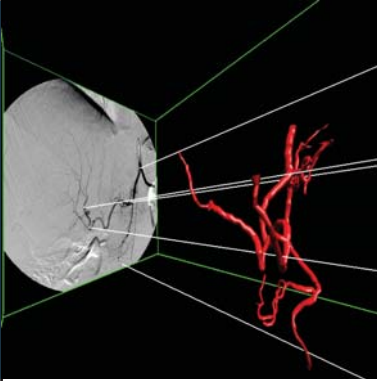


Computer Aided Medical Procedures
(CAMP)
Prof.Dr. Nassir Navab



Dissertation

2D-3D Registration of Vascular Images Towards 3D-Guided Catheter Interventions

Martin Groher



Fakultät für Informatik
Technische Universität München

2D-3D Registration of Vascular Images Towards 3D-Guided Catheter Interventions

Martin Groher

Vollständiger Abdruck der von der Fakultät für Informatik der Technischen
Universität München zur Erlangung des akademischen Grades eines

Doktors der Naturwissenschaften (Dr. rer. nat.)

genehmigten Dissertation.

Vorsitzender: Univ. Prof. Dr. Bernd Radig

Prüfer der Dissertation:

1. Univ. Prof. Nassir Navab, PhD
2. Prof. Dr. ir. Max A. Viergever,
University Medical Center Utrecht/Niederlande

Die Dissertation wurde am 20.09.2007 bei der Technischen Universität München
eingereicht und durch die Fakultät für Informatik am 18.03.2008 angenommen.

Abstract

Angiographic imaging is a widely used monitoring tool for minimally invasive vascular treatment and pathology access. Especially in deforming abdominal areas, the registration of pre- and intraoperative image data is still an unsolved problem, but important in several aspects. In particular, treatment time and radiation exposure to patient and physician can be significantly reduced with the resulting 2D-3D data fusion.

The focus of this work is to provide methods for the registration of 2D vascular images acquired by a stationary C-arm to preoperative 3D angiographic Computed Tomography (CT) volumes, in order to improve the workflow of catheterized liver tumor treatments.

Fast and robust vessel segmentation techniques are used to prepare the necessary graph data structures for a successful alignment. Here, we introduce restricted correspondence selection and iterative feature space correction to drive the proposed rigid-body algorithms to global and accurate solutions. Moreover, it is shown for the first time that the assignment of natural constraints on vessel structures allows for a successful recovery of a 3D non-rigid transformation despite a single-view scenario.

Based on these results, novel volumetric visualization and roadmapping techniques are developed in order to resolve interventional problems of reduced depth perception, blind navigation, and motion blur.

Keywords:

2D-3D Registration of Medical Images, Segmentation of Vascular Structures, Angiography

Zusammenfassung

Angiographische Bildgebung ist ein weitverbreitetes Verfahren zur Überwachung minimal-invasiver Gefäßbehandlungen. Vor allem in deformierbaren Bereichen des Abdomens stellt die Registrierung von prä- und intraoperativen Bilddaten noch immer ein ungelöstes Problem dar. Sie birgt jedoch einen großen Zugewinn, da durch die daraus resultierende Bildfusion insbesondere die Behandlungszeit und die Strahlungsbelastung sowohl für den Patienten als auch für den behandelnden Arzt reduziert werden können.

Der Fokus dieser Arbeit liegt auf der Entwicklung von Methoden zur Registrierung von 2D Vaskulärbildern, die mittels eines stationären C-Bogens aufgenommen werden, zu präoperativen 3D CT Angiographievolumen. Dadurch soll der Arbeitsablauf von Kathetereingriffen zur Behandlung von Lebertumoren verbessert werden.

Schnelle und robuste Gefäßsegmentierungstechniken werden angewandt, um die zur Registrierung notwendigen Graphenstrukturen vorzubereiten. Eine restriktive Korrespondenzauswahl sowie iterative Korrekturen eines Merkmalsraumes werden vorgestellt. Diese Techniken sind notwendig, um die in dieser Arbeit entwickelten rigiden Registrieralgorithmen zu globalen und akkuraten Lösungen konvergieren zu lassen. Darüber hinaus wird gezeigt, dass eine nichtrigide 3D Transformation unter der Verwendung nur eines einzelnen Blickwinkels berechnet werden kann, indem natürliche Beschränkungen auf die Bewegung von Gefäßen mathematisch formuliert und eingesetzt werden.

Basierend auf diesen Registrierungsergebnissen werden neue volumetrische Visualisierungsverfahren sowie "Roadmapping" Techniken entwickelt, um Interventionsprobleme wie verminderte Tiefenwahrnehmung, blinde Katheternavigation, und Bewegungsverzeichnungen zu lösen.

Schlagwörter:

2D-3D Bildregistrierung, Segmentierung von Vaskulärsystemen, Angiographie

Acknowledgments

First of all, I'd like to thank Professor Nassir Navab for the extraordinary supervision I received. Additional Saturday meetings in coffee shops, or nightly discussions via Skype are most probably not very common among doctor fathers - a privilege I appreciated very much.

I'd also like to thank all the people from CAMP, which (some more, some less) helped me achieve my research goals. In particular, I want to thank Andreas Keil for enduring my numerous attempts to discuss scale-spaces, filtering, or transformations, and Ben Glocker for proof-reading and the various discussions on balconies, or in pubs, which started with work but mostly ended somewhere totally different. I want to thank Darko Zikic for the most careful proof-reading, the ideas he shared, and the great time we had in our common office. Thanks to Pierre who visited me in the mornings even though I have the most remote office of all, and to Martin Horn for pimping all the multimedia. Also, I want to thank all the students that helped me during the time of my PhD work, especially Nicolas Padoy and Frederik Bender. I am also grateful for all the help and valuable explanations I got from my physician partners, in particular Tobias Jakobs, Ralf Hoffmann, and Tobias Waggerhauser. Of course, thanks to Siemens AX for their financial support, and to Klaus Klingenberg-Regn as well as Marcus Pfister for valuable input.

I'm very much obliged to my parents, who always supported me during my studies, and made this thesis possible in the first place. Their understanding and support was exceptional and priceless. I'm indebted to my sister Evi, who always knew how to motivate me, either by choosing the right words, or the right mountain to climb, or by simply sharing the same situation. Finally, I want to say thank you to Simone, who accompanied me during this (sometimes happy, sometimes troublesome) time. Thank you, Simone, for being with me during all the minor and major crisis that I faced in the last three years, thank you for encouraging me, cheering me up, and preventing me of loosing focus. Without any of you four this thesis would not have happened.

Contents

Brief Summary of the Thesis	xi
Outline of the Thesis	xiii
I. Introduction, Methodology, and State of the Art	1
1. Introduction	3
1.1. Problem Statement	4
1.1.1. Terminology	5
1.2. Angiography in the Clinic	7
1.2.1. Preoperative Imaging: CTA and MRA	7
1.2.2. Intraoperative Imaging: C-arms	8
1.3. A Registration System for Abdominal Catheterizations	10
1.3.1. Imaging for Liver Interventions	11
1.3.2. Justification for a 2D-3D Angiographic Registration	11
1.3.3. Medical and Technical Requirements	12
1.4. Contribution	13
2. Methodology	15
2.1. Images	15
2.2. Vessels in Medical Images	17
2.2.1. The Hessian in Vessel Analysis	17
2.2.2. Vessel Enhancement	19
2.2.3. Segmentation Initialization	20
2.2.4. Segmentation	21
2.2.5. Quantification	22
2.2.6. Suggestions for Method Selection	26
2.3. Medical Image Registration	27
2.3.1. Data Terms	28
2.3.2. Transformations	30
2.3.3. Correspondences	34
2.3.4. Optimization	36
2.4. 2D-3D Registration	38
2.4.1. Rigid 2D-3D Registration	39
2.4.2. Calibration	40
2.4.3. Error Analysis	41
3. State of the Art in 2D-3D Angiographic Registration	45

3.1. Intensity-based 2D-3D Registration	45
3.1.1. DRR Generation	46
3.1.2. Registration Algorithms	48
3.2. Feature-based 2D-3D Registration	50
3.2.1. Distance Functions	51
3.2.2. Optimizer-based Algorithms	52
3.2.3. ICP-based Algorithms	53
3.3. Hybrid 2D-3D Registration	55
3.4. Deformable 2D-3D Registration	57
3.5. Discussion	58
3.5.1. Initialization	58
3.5.2. Directions of Future Research	59
II. New Algorithms for 2D-3D Angiographic Registration	61
4. Clinical Application	63
4.1. Medical Excursion: Liver Vessel Systems	63
4.2. Treatment of Liver Tumors	64
4.3. Workflow of Transarterial Chemoembolizations	66
4.4. Feasibility of 2D-3D Registration	67
4.4.1. Data Availability	67
4.4.2. Challenges	68
4.4.3. State-of-the-Art Applicability to TACE	69
5. Rigid 2D-3D Registration of Angiographic Images	71
5.1. C-arm Model	71
5.2. Preprocessing	73
5.2.1. Segmentation	73
5.2.2. Extraction of Graphs	73
5.2.3. Graph Representation of Vessel Centerlines	75
5.3. Bifurcation-Driven 2D-3D Registration	76
5.3.1. Initialization	76
5.3.2. 4 DOF Optimization	77
5.3.3. Algorithm Evaluation	79
5.3.4. Discussion	81
5.4. Segmentation-Driven 2D-3D Registration	82
5.4.1. MLE with Labelmaps	83
5.4.2. The EBM Algorithm for Angiographic Registration	85
5.4.3. Algorithm Evaluation	88
5.4.4. Discussion	93
6. Deformable 2D-3D Registration of Angiographic Images	95
6.1. Method	97
6.1.1. Setting and Preprocessing	97

6.1.2.	Preliminaries and Notation	98
6.1.3.	The Model	99
6.1.4.	Difference Measure	100
6.1.5.	Length Preservation Constraint	100
6.1.6.	Diffusion Regularization and Bending Energy	101
6.1.7.	Position Retention Constraint	102
6.1.8.	Optimization Scheme	102
6.2.	Results and Evaluation	103
6.2.1.	Parameter Values and Smoothness Term	103
6.2.2.	Tests on Synthetic Data	104
6.2.3.	Real Data with Artificial Deformation	104
6.2.4.	Real Data with Natural Deformation	105
6.2.5.	Clinical Test	105
6.3.	Discussion	107
7.	Conclusion	111
7.1.	Workflow Integration	112
7.1.1.	Intraoperative Visualization	112
7.1.2.	Real-Time Breathing Correction	115
7.2.	Future Work	116
	Appendix	121
A.	Practical Considerations on Images	121
A.1.	Image Filtering	121
A.2.	Image Derivatives	122
A.3.	Linear Scale-Space	122
B.	Thin Plate Splines	125
B.1.	Special Spline Smoothing Problem	125
B.2.	Numerical Solution	126
B.3.	TPS for Feature-Based Deformable Registration	127
C.	Rotation Parameterization	129
C.1.	Euler Angles	129
C.2.	Gimbal Lock	129
C.3.	Euler Angles in Rigid Registration	130
D.	Real-Time Respiratory Motion Tracking	131
D.1.	Method	131
D.1.1.	Motion Model	131
D.1.2.	Approximation of Vessel Motion by Catheter Motion	131
D.1.3.	Motion Tracking on Enhanced Images	132
D.1.4.	Dynamic Template Update	132
D.2.	Results	133

D.2.1. Simulation Studies	133
D.2.2. Patient Studies	133
E. List of Symbols	137
F. List of Abbreviations	141
G. List of Publications	145
Bibliography	147

Brief Summary of the Thesis

In this thesis, we develop novel methods for the registration of angiographic 3D and 2D data sets. We focus on liver catheterizations, in particular Transarterial Chemo-embolizations (TACE) as a frequently used treatment for liver tumors, where a fusion of preoperative CTA and intraoperative DSA data can provide valuable information in terms of depth perception and intraoperative navigation, but also has to meet certain requirements for automation, speed, and accuracy. The contributions of this work are the proposal of a new CTA protocol for artery visualization in a TACE workflow, two novel rigid registration algorithms, and a method for deformable 2D-3D registration in a single-view scenario.

The introduction of a new CTA protocol to visualize liver arteries allows for a feature-based alignment, where the difficulties of vessel extraction, the correspondence problem in heterogeneous feature spaces, and non-rigid registration in a one-view scenario have to be overcome.

We will conceive two novel rigid registration algorithms, which were tailored to be robust against segmentation errors, different contrast propagation, and deformation changes.

The *bifurcation-driven registration* restricts the feature space to ramification points of the underlying vessel structure and reduces the number of outliers by iterative graph extraction on projected centerline images. By combining this technique with topological information of the vessel graphs, a new distance function is developed.

While the bifurcation-driven registration yields good results in many clinical cases, it also requires a minimal amount of user interaction intraoperatively. Thus, we develop a second technique that performs fully automatic during the intervention. The *segmentation-driven registration* combines 2D DSA segmentation with 2D-3D pose estimation using a probability map in order to consequently discard false positives in the two vascular systems. This probability map, embedded in a Maximum Likelihood formulation, proves to be beneficial in terms of accuracy (ca. 1.45 mm mean Projection Distance (mPD)) and robustness compared to hybrid methods, which avoid 2D segmentation. Since this enhanced feature space does not require an optimal segmentation, an automatic seed detection can be employed to provide an integration into intraoperative workflow without additional user interaction.

Both algorithms are evaluated on simulated as well as several clinical data sets, root mean square errors and target registration errors are measured, and Monte Carlo simulations are carried out to show the high accuracy and robustness of the proposed methods despite non-rigid motion.

A further issue that is addressed in this thesis is the refinement of a (sub-optimal) rigid vascular alignment in a non-rigid environment. A new *2D-3D deformable registration* algorithm is proposed that solves for a 3D deformation field using only the information of a single view. The minimization of an energy term based on the Eu-

clidean distance between corresponding points is rendered well-posed by incorporating natural and mathematically valid constraints of length preservation of vessel structures and smoothness of local transformations. A 3D deformation field can be computed thus, where even the displacement in projection direction is captured, improving the results of rigid 2D-3D registration considerably.

The integration of the computed results into interventional workflow will be addressed in the end of the work. Proper visualization techniques are developed to project roadmap information onto the current 2D image, or to visualize 2D catheter locations in 3D via correspondence information. After DSA acquisition, clinicians usually continue the navigation by means of fluoroscopic imaging. Tracking the apparent motion of the catheter in 2D allows for a propagation of the registration results to these subsequent images. Thus, registration results can be updated to the current clinical situation and intraoperative 3D visualization is not hampered by breathing motion.

Outline of the Thesis

This thesis is subdivided into two parts.

The first part provides an introduction, the methodological background, and a review of existing techniques.

The second part presents details on the clinical applications, new algorithms for 2D-3D registration, and a conclusion section with extensions and future work.

Part I: Introduction, Methodology, and Review

CHAPTER 1: INTRODUCTION

A general introduction into the problem, a description of angiographic devices used in medical imaging, and a justification for a 2D-3D registration system for angiographic treatments.

CHAPTER 2: METHODOLOGY

The methodological basis of this thesis, including vessel analysis, issues for medical image registration, and a focus on 2D-3D registration in a C-arm scenario.

CHAPTER 3: STATE OF THE ART IN 2D-3D ANGIOGRAPHIC REGISTRATION

A review of existing techniques for 2D-3D vascular image registration.

Part II: New Algorithms for 2D-3D Angiographic Registration

CHAPTER 4: CLINICAL APPLICATION

The clinical application that is focused in this work, Transarterial Chemoembolization. A short introduction in liver vessel systems and tumor treatment followed by a critical analysis in terms of challenges and applicability of state-of-the-art algorithms.

CHAPTER 5: RIGID 2D-3D REGISTRATION OF ANGIOGRAPHIC IMAGES

Two new algorithms for rigid 2D-3D registration. A one-click technique for registration based on bifurcation alignment aided by topological information, and a fully automatic method based on iterative segmentation and alignment using vessel probabilities.

CHAPTER 6: DEFORMABLE 2D-3D REGISTRATION OF ANGIOGRAPHIC IMAGES

A novel method for 2D-3D deformable registration of a vascular model to a single projection image.

CHAPTER 7: CONCLUSION

A short summary followed by a discussion of the integration of the registration algorithms into clinical workflow and future work.

Appendix

PRACTICAL CONSIDERATIONS ON IMAGES

Some implementation details for image analysis.

THIN PLATE SPLINES

A deformation model used for the deformable registration algorithm derived in the thesis.

ROTATION PARAMETERIZATION

A short summary of the chosen parameterization for 3D rotations.

REAL-TIME RESPIRATORY MOTION TRACKING

An algorithm for tracking and compensation of breathing motion apparent in fluoroscopic image sequences.

LIST OF SYMBOLS

The mathematical symbols used.

LIST OF ABBREVIATIONS

A list of abbreviations used throughout the work.

LIST OF PUBLICATIONS

All publications contributed to the scientific community during this work.

Part I.

Introduction, Methodology, and State of the Art

1. Introduction

Angiographic interventions or surgeries are performed on an every-day basis in many hospitals. Blood vessels, distributed throughout the body, have to be accessed for numerous medical procedures such as stenting of coronary arteries, treatment of stenoses in brain vessels, reduction of blood pressure, or embolization of tumor vessels to name a few. Nowadays, such treatments can be guided by angiographic imaging, supporting physicians in the assessment of instrument and blood vessel locations. In contrast to open surgery, treatments guided by angiographic images can be performed minimally-invasive, i.e. only a small incision is needed to inject instruments, which can be located and navigated by the use of the acquired images.

It is common in hospitals that images of patients are acquired before the treatment (preoperatively) for diagnosis and/or for procedure planning. These preoperative images are usually of high quality and are acquired in 3D (e.g. using Magnetic Resonance (MR) or Computed Tomography (CT) scanners). Imaging data acquired during medical procedures are of less quality, which means in this respect that they usually have a lower signal-to-noise ratio (SNR), and a lower dimensionality (2D slices or 2D projections instead of full 3D volumes). They usually have, however, a higher spatial resolution, which is due to the high zooming capabilities of intraoperative imaging devices. This intraoperative data is used to assess the state of instruments and patient anatomy over time. Even though recent advances in intraoperative imaging have brought 3D acquisitions into operating rooms (e.g. 3D rotational angiography) yielding nearly the same quality as preoperative scanners, they are - due to hard time constraints and high X-ray dosage - performed seldomly. Moreover, they do not capture the temporal aspect of the procedure, i.e. advancements of instruments or changes of anatomy due to deformation cannot be assessed by a static 3D scan.

The registration of pre- and intraoperative data sets would fuse patient anatomy information of superior quality with information capturing the current state of the operation. With this registration, new ways of intraoperative roadmapping and navigation can be introduced, the treatment can be sped up, and harmful radiation that physicians and patients are exposed to can be reduced. Such registration systems are already commercially available for surgery procedures, however, no angiographic registration system has been launched on the market yet. This is due to the difficulty to directly apply existing techniques (often based on external tracking) to vasculature deformed by internal organ movement. However, especially in deformable regions like thoracic or abdominal areas, the task of vascular image alignment, while challenging from a technical point of view, yields the maximal benefit for the operating physician, since navigating a catheter through moving structures requires a high level of dexterity, training, and anatomical knowledge.

Since angiographic images sometimes exclusively visualize blood vessels (e.g. dig-

itally subtracted angiography (DSA) images), an intuitive approach for this data fusion would use vessel features for alignment, which, to this end, would require a segmentation of pre- and intraoperative vasculature. Tools for vascular segmentation are commercially available, but are, up to this moment, only used for diagnosis and follow-up studies. Thus, these segmentation algorithms are not subject to hard time constraints and also require manual interaction, which cannot be afforded intraoperatively. However, preoperative data can be preprocessed with these tools yielding valuable information of vessel location and characteristics, which can be incorporated into the intraoperative registration.

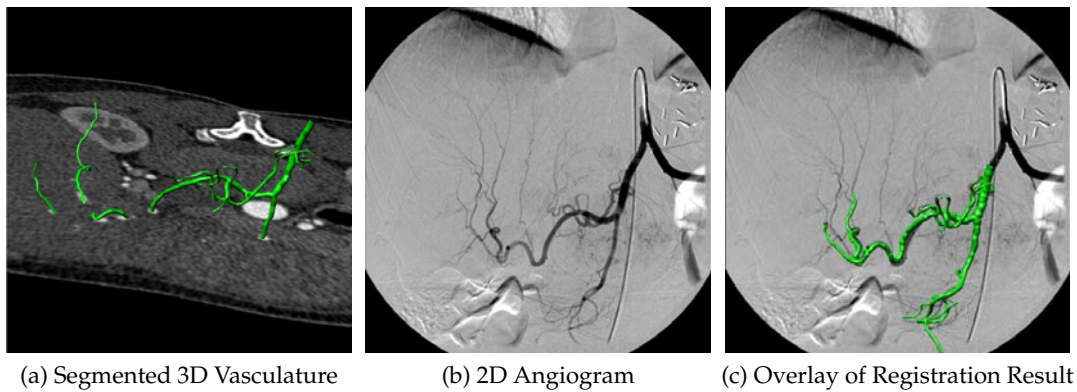


Figure 1.1.: Overview from the C-arm perspective of the problem addressed in this thesis: Given a 3D volume (a) and one 2D image (b) of vasculature, find the alignment of volume and image (c)

To summarize, different images are taken during medical procedures. Preoperative images show *detailed* information of anatomy, intraoperative images show *current* information of instruments and anatomy. The motivation for this work is that a fusion of these data sets would be very beneficial for treatments in many aspects. The treatment time can be reduced, as can be radiation exposure to patient and physician. A direct image fusion in areas that are subject to deformation is currently not possible with existing techniques, however, preprocessing can provide valuable information of anatomy preoperatively, which must not be discarded for the intraoperative alignment.

1.1. Problem Statement

In this thesis we address the problem of aligning angiographic 2D images of a single viewpoint to 3D volumes of the same object. In particular, we want to solve the *single-view 2D-3D registration* problem in the context of angiographic images. Since angiographic images visualize the human vessel system, such registration systems

make frequently use of vessel locations and characteristics. To this end, these systems require segmentation and quantification techniques. We concentrate our registration efforts on abdominal interventions, in particular liver catheterizations. These medical procedures raise the issue of anatomical deformation, which has not been addressed by existing solutions for 2D-3D registration yet. For a visual overview of our problem refer to fig. 1.1 for a visualization in a C-arm perspective and fig. 1.2 for an external illustration.

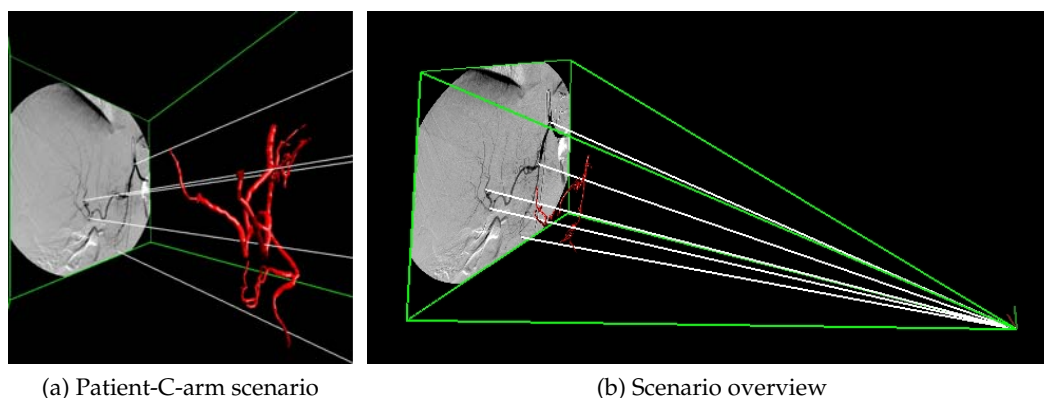


Figure 1.2.: External overview of the problem addressed in this thesis: Patient-C-arm scenario (a) the projective lines (white) must correlate 2D to 3D features of the patient vessel system. (b) overview figure of the patient-C-arm scenario

1.1.1. Terminology

We now give quasi-formal definitions of the basic terms that will be used within this work.

Definition 1.1 (Angiography) *A method to visualize blood vessels. The visibility of vasculature in images can either be achieved by the injection of a radiopaque substance (contrast agent) through a catheter into the vessel system¹ (Computed Tomography Angiography [CTA], intraoperative X-ray Angiography), or by a special acquisition sequence (Magnetic Resonance Angiography [MRA], Ultrasound Angiography).*

Within the scope of angiographic imaging it is also important to explain the term *fluoroscopy*, which is an X-ray procedure where 12-15 frames per second (FPS) are acquired. An image sequence can be assembled showing a “movie” of the anatomy of the patient in real-time. Fluoroscopic imaging is used to monitor instruments like catheters, organ movement, and vessel structures if combined with contrast injection.

¹since blood has the same radio-density as surrounding tissue

Definition 1.2 (Registration) *Registration is used to bring two or more images into spatial alignment, which are taken, for example, at different times, from different modalities, or from different viewpoints [19, 95].*

Definition 1.3 (Segmentation) *Image segmentation is the partitioning of an image into nonoverlapping regions that are homogeneous with respect to some characteristic such as intensity or texture [120, 52].*

Ambiguities Even though scientific terminology is tailored to uniqueness, there are always some ambiguities in the terms that are used by researchers. Moreover, since the work addresses different, highly interdisciplinary fields, misinterpretations of notation and terminology can arise easily. Thus, we would like to fix the meaning of certain terms that are used throughout this thesis. These are not mathematical definitions yet (for those, refer to chapter 2), but should make the semantics of certain terms clearer.

- *Image.* This term denotes not only 2D camera pictures, but all 2D, 3D, or 4D imaging data that can be acquired by appropriate devices. Hence, sequences (“movies”), or 3D volumes will be denoted as such, too.
- *Interventional and Operative.* In German hospitals it is important to distinguish between interventions and operations. Operations have higher requirements for sterility, whereas interventions are quasi-ambulant procedures where only operating physician, region of interest (ROI), and instruments have to be sterile. In this thesis, we do not have to distinguish between these two medical procedures, and use the term “operative” in the same context as “interventional”, e.g. preoperative meaning “before” the operation or intervention, and intraoperative meaning “during” the operation or intervention.
- *Roadmapping.* The term roadmapping is used in angiographic interventions for visualizing the path in the vasculature, through which a physician has to guide the catheter. It can be for example provided by an overlay of previously acquired contrasted images and currently acquired fluoroscopic image.

In the following, we give an insight into angiographic imaging modalities that are involved during medical treatments. In section 1.3 the work- and dataflow together with a short justification of a registration system for abdominal interventions is described, followed by a brief description of requirements. At the end of this chapter, we sum up all contributions made throughout this work: a new CTA protocol for liver catheterizations, a semi-automatic 2D-3D registration technique for angiographic interventions driven by anatomical features, a fully automatic 2D-3D registration technique driven by vessel probabilities, and an approach to the difficult problem of single-view 2D-3D *deformable* registration.

1.2. Angiography in the Clinic

Angiographic imaging has become essential for diagnosis and treatment. There are different techniques for pre- and intraoperative angiographic patient scanning, those of which are important for the task in this thesis will be covered in the following.

1.2.1. Preoperative Imaging: CTA and MRA

For diagnosis and planning of angiographic interventions, two modalities are commonly used, Computed Tomography Angiography (CTA) and Magnetic Resonance Angiography (MRA). Both acquire a sliced volume of the patient visualizing contrasted vessel structures as well as bone, organ, and tissue anatomy.

Computed Tomography Angiography CT is based on image reconstruction from X-ray beams. In a gantry ring, one or two X-ray sources rotate around the object². From different angles a fan-shaped beam of X-rays is emitted and captured by a detector ring (or row) consisting of 1-64 slices. For one X-ray, its mean attenuation according to the radio densities of the traversed object is recorded by a detector element. A sinogram³ is produced from which the densities at spatial positions can be reconstructed. Mainly, two methods are used for this reconstruction, filtered back projection (FBP) and the algebraic reconstruction technique (ART) [71].

With state-of-the-art CT scanners, CTA volumes can be acquired with a spatial resolution of $\leq 0.4 \times 0.4 \times 0.4 \text{ mm}^3$ voxels showing contrasted vessel of a diameter down to 0.35mm [43]. CT scanners can visualize the typical range of Hounsfield units (HU), i.e. from -1000 to 1000 HU, resembling the X-ray attenuation of air (-1000 HU, black) and bone (1000 HU, white).

CT Angiography is a method to visualize blood vessels by contrast injection during CT scanning. The contrast material (iodine, or barium liquid) is injected into a vein at the periphery (e.g. arm) and circulates with the blood through arterial and venous system. A region in the aorta is constantly scanned until a certain mean intensity (e.g. 150 HU) is reached, which triggers the scan to acquire the actual image (bolus tracking). More scans can be done after a certain delay time. Amount of contrast administered, bolus tracking, and delay time follow certain acquisition protocols that are fine-tuned to anatomy, patient, and disease [44].

Magnetic Resonance Angiography Magnetic Resonance Imaging (MRI) is not using the imaging properties of X-ray attenuation as does CT and is thus not hazardous in terms of ionizing radiation (X-rays). It acquires signals that are emitted from relaxation processes of proton spins whose phases were changed (excitation) by a radiofrequency pulse. Each tissue has a different number of protons, causing the emission of tissue-specific signals. In order to determine the spatial location of the

²in state-of-the-art machines, with a rotation speed of 0.33sec per gantry rotation

³a stack of 2D images, where a column in an image corresponds to the projection of n rays of a fan beam from one angle

signals, magnetic field gradients are applied for slice selection, row selection (phase encoding), and column selection (frequency encoding).

There are several MR Angiography techniques, some of them involving a contrast injection as CTA. Here, however, the contrast has to be paramagnetic extracellular, e.g. gadolinium. There are also fully non-invasive techniques for angiographic MR imaging by using the flow property of blood (Time-of-Flight MRA, Phase-Contrast MRA). See Figure 1.3 for an example of contrasted CTA and MRA slices.

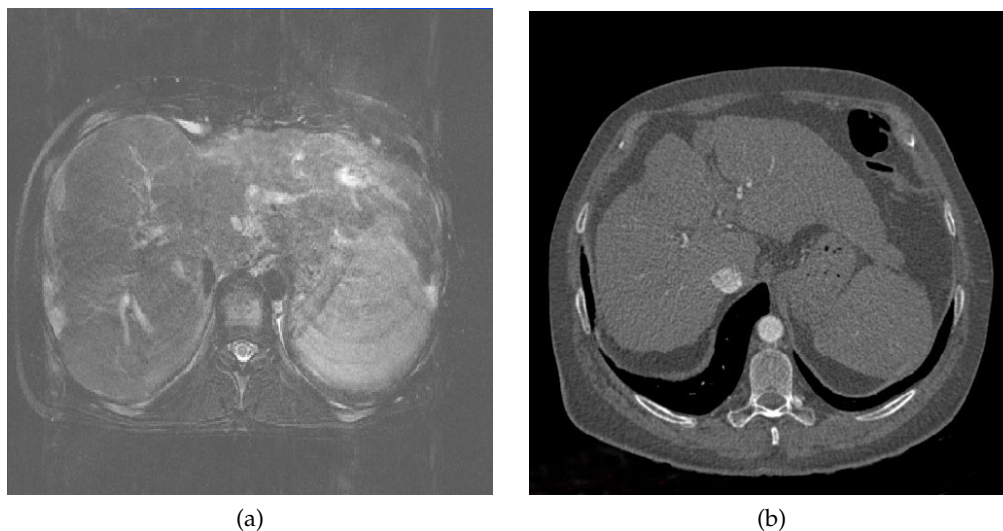


Figure 1.3.: MRA (a) and CTA (b) slice of a liver

1.2.2. Intraoperative Imaging: C-arms

During angiographic procedures, the most commonly used device is a so-called C-arm, a C-shaped machine with an X-ray source and a detector plane at the respective ends of the "C" (see Figure 1.4). A table is moved into the iso-center of the C on which the patient can be screened from different viewpoints by altering two possible angles, table position, and zoom. Similar to CT imaging, the physical law of radiation attenuation is used to produce images. In contrast to CT, where a fan beam is travelling through the object (creating only few lines of intensities), C-arms emit a cone-beam of X-rays that fills a 2D array with intensities. Different C-arms are available for intraoperative usage - leading from "basic" fluoroscopic devices to high-end cone-beam reconstruction C-arms yielding 3D volumes with CT-like image quality.

Since technical properties and thus image quality of C-arms differ, we will introduce a short categorization of existing C-arm devices according to their attributes. Mind that this will not be a thorough technical classification, it should just help to distinguish between properties that will be of importance for the task in this thesis, 2D-3D angiographic image registration.



(a) mobile C-arm with image intensifier



(b) floor-mounted stationary C-arm with image intensifier



(c) ceiling-mounted stationary C-arm with flat panel detector



(d) ceiling-mounted stationary C-arm with bi-plane imaging system

Figure 1.4.: Different C-arm imaging devices

- 2D and 3D:** The minimal functionality of C-arms that are currently used in hospitals covers fluoroscopic and digital subtraction image acquisition. Fluoroscopic imaging creates image sequences of about 12-15 FPS, whereas digitally subtracted angiograms (DSA) are acquired at a frame rate of ca. 5 FPS, where a non-contrasted X-ray image is subtracted from a contrasted one to visualize the vessels only. Many state-of-the-art C-arms perform an alignment (2D registration) of non-contrasted and contrasted view in order to reduce motion artifacts retrospectively [102]. The spatial resolution of fluoroscopic images or DSAs currently goes down to 0.13mm per pixel. Newer C-arms have the ability to perform a rotational run around the patient to acquire 150-500 projection images from different viewpoints. With cone-beam reconstruction techniques [144] 3D volumes can be computed in less than 1min with a spatial resolution of down to 0.4mm^3 , either visualizing 3D vasculature or intensity volumes

measured in Hounsfield units. Up to now, preoperative CT scanners still have a better Hounsfield resolution (every single unit is distinguishable) than intraoperative C-arms (every 5th unit is distinguishable) [136].

- **stationary and mobile:** There are systems that are fixed in the interventional room, either mounted to ceiling or floor, and mobile C-arms that can be moved on wheels. The price to pay for the higher spatial flexibility of mobile C-arms is the lower image quality especially for 3D reconstructions due to mechanical jittering during acquisition. For mobile devices, a geometric calibration step is necessary before each intervention in order to provide 3D acquisitions, whereas stationary systems require a geometric calibration every 6 months only.
- **mono- and biplane:** Stationary C-arm machines are equipped with one (mono-plane) or two (biplane) X-ray-source detector systems. The two image planes are usually related by a 90° rotation relative to each other. Especially minimally-invasive neurological surgeries are typically performed using biplane C-arms, whereas abdominal or cardiac procedures are usually monitored by mono-plane imaging systems. When using images from two views, 2D-3D registration, or reconstruction of instrument locations in 3D can be performed easier and more accurately.
- **flat panel and image intensifier:** There are two technologies used for transferring X-rays into gray values and producing digitized images. Image intensifier systems convert photons into electrons that are accelerated and produce photons that can be captured by a CCD camera. Flat panel systems transfer X-rays into light rays that are detected by elements (based on thin-film-transistor technology) with the size of a pixel. The flat panel technology has been introduced to overcome drawbacks in image intensifier systems. For example, image distortion, caused by a curve-to-plane warping and the earth magnetic field only emerge in image intensifier systems [133]. For calibration issues, and thus for the task of this work, 2D-3D registration, it is important to know about the presence of distortion in order to determine corresponding points of 2D image plane and 3D image.

After this general introduction to angiography as it is applied and used in the clinic, we focus on a more specific clinical scenario in the following section. This shall help to illustratively explain the problem, summarize a typical workflow, and derive requirements for a system of 2D-3D angiographic registration.

1.3. A Registration System for Abdominal Catheterizations

Due to the increasing capabilities of medical imaging devices, pre- as well as intraoperative imaging techniques are used for numerous different applications, e.g. neurosurgery, abdominal catheterizations, or needle biopsies. In fact, the focus of

this work lies on abdominal angiographic interventions, in particular liver catheterizations. Liver catheterizations capture many difficulties for the operating physician that are faced during angiographic interventions, as for instance motion blur of images or reduced intraoperative depth perception due to single-view systems.

In the following, we will give a brief summary of the imaging workflow that is typical to many abdominal angiographic interventions, especially the numerous different hepatic catheterizations. From this description, we will justify the necessity of 2D-3D registration and shortly summarize its most important requirements. With this section we want to motivate the task of 2D-3D registration and outline its major difficulties. A complete explanation of the focused clinical application, its purpose, data-, and workflow, as well as an extensive discussion of the challenges that are posed to a registration system will be postponed to chapter 4.

1.3.1. Imaging for Liver Interventions

The current workflow of catheter-based liver interventions (e.g. Transarterial Chemoembolizations (TACE), see chapter 4, or Transjugular Portosystemic Shunt (TIPS) procedures) usually includes the acquisition of one or more preoperative 3D data sets using CTA or MRA. There are different scan protocols for visualizing the region of interest and/or the vascular tree. These data sets are used before the procedure to assess region of interest (ROI), a path (or roadmap) through the vessel system to reach this ROI with a catheter, and possible complications due to, e.g., thrombus from former treatments.

In the current clinical workflow, this preoperative data is not made available during the intervention. Intraoperatively, the physician relies on the 2D projections of patient anatomy coming from fluoroscopic sequences (to visualize the current location of injected instruments) and DSAs (to get a better orientation of the vascular system). In most hospitals, only mono-plane C-arms are used for abdominal catheterizations in contrast to neuro surgery, where biplane systems are frequently utilized. 3D acquisitions are performed with injected contrast to get a 3D visualization of the current state of vessels and catheter. These acquisitions are hazardous in terms of radiation exposure for both physician and patient. Thus, they are usually performed at most twice per treatment. Moreover, the acquisition of a static 3D volume does not allow for fusion of subsequent angiographic images with the 3D vasculature due to liver motion induced by patient breathing.

1.3.2. Justification for a 2D-3D Angiographic Registration

Guided by 2D projections of one view only, it is sometimes difficult for the operating physician to find a path through the patient's vessel system. This is due to projection overlay and self-occlusion of vessel structures that run orthogonal to the image plane (*reduced depth perception*). Moreover, since contrast agent only stays inside the vessels for a short period of time, the catheter has to be navigated through the vessel system with only static or temporal additional information on vessel segments and

bifurcation points (*blind navigation*). The patient breathing changes the current position of the visualized instruments hampering the navigation additionally (*patient motion*).

In order to overcome these problems, a method shall be developed to transfer information from 2D to 3D and vice versa in order to increase depth perception and thus allow for a reduction of radiation exposure for patient and physician as well as a decrease in amount of contrast agent administered.

An accurate 2D-3D registration of pre- and intraoperative data allows for an overlay of projected vasculature with current 2D fluoroscopic images for roadmapping without new contrast injection. Moreover, back-projecting instrument locations to 3D in order to regard instruments and ROI from different viewpoints within a model of the entire vasculature can be achieved. An important application of 2D-3D registration in abdominal interventions is the initialization of motion compensation software to track breathing motion over time in fluoroscopic image sequences. If planned information (e.g. the location of region of interest, a path through the vessel system to reach it, etc.) is available in the 3D data to be registered, transferring this information to the current intraoperative situation can be offered through 2D-3D registration combined with motion tracking.

Since 3D data can be acquired on the same device used for 2D imaging, a 3D-3D registration algorithm together with a previous calibration step should achieve an accurate registration of preoperative 3D and intraoperative 2D data. However, due to patient breathing, a 2D-3D registration step is needed to compensate for this motion induced by respiration even if 3D data is available intraoperatively.

Active research on 2D-3D registration techniques for angiographic images has started in 1994, we will give an extensive review in chapter 3. Most of the existing techniques have not focused on regions that are subject to deformation but rather rigid regions (e.g. brain) to develop techniques for estimating the pose of the 3D image. Moreover, some of these algorithms require user interaction, e.g. a manual selection of vessel segments to be registered. Thus, the direct transfer of existing methods is difficult for the goal of this work, a fast and robust 2D-3D registration technique that can be used for abdominal interventions.

1.3.3. Medical and Technical Requirements

From the medical point of view, the requirements for a 2D-3D registration method that can be used in the clinic are as follows. First, during the intervention, the operating physician has to perform tasks quickly to reduce intervention time. Therefore, the method is subject to hard time constraints. Second, user interaction must be kept as low as possible in order to avoid distractions for the interventionalist from performing the actual medical procedure. Third, as there is a considerable amount of technical devices in a state-of-the-art operating room, the registration should only make use of available data, i.e. external devices should be avoided.

Technically, a registration software for angiography requires the following: First the viewpoint with which the 3D volume has to be projected in order to produce the same image as the current one is to be found (*rigid 2D-3D registration*). Second,

since contrast agent is administered globally in the preoperative case and locally in the intraoperative one, the visualized vasculatures differ in the actual structures that are displayed. Thus, the registration method must cope with this difference in the structure of interest (*robustness to outliers*). To this end, meaningful initialization techniques are also required to start an optimization of registration parameters near the global optimum. In abdominal procedures, breathing causes a motion, which has to be taken into account for any registration algorithm. This motion, as reported in the literature, contains a rigid and a non-rigid (deformable) part [151, 124]. Thus, as a third and last point, the rigid registration has to be robust to breathing changes, and an accurate registration shall be achieved by extending the method to deformable registration (*deformable 2D-3D single-view registration*).

1.4. Contribution

In the course of this work, several algorithms for vascular image registration and a new protocol for CTA acquisition have been contributed to the international scientific community of Medical Image Analysis . Here is a short summary together with the publications that resulted from the continuous research on 2D-3D angiographic image registration:

- Until now, 2D-3D registration of data from abdominal catheterizations was not possible due to the absence of a suitable preoperative scanning protocol. This issue is addressed by introducing an angiographic CT scanning phase [58]. The scan visualizes arteries similar to the vasculature captured with an intraoperative C-arm acquiring DSAs. With this new scan protocol and a suitable registration algorithm a strong link is created between radiologists and interventionalists by bringing preoperative patient and planning information to interventional workflow [106].
- A rigid registration algorithm is conceived to align 3D and 2D vessel structures segmented from abdominal CTA and DSA images respectively [59, 58]. With a minimal amount of user interaction, centerlines of vascular systems are extracted and graph representations are created from 3D and 2D data. By restricting the feature space on bifurcation points only and using topological information of the underlying graph structure, the method is able to compute the right pose accurately and robustly. A comparison to a state-of-the-art algorithm shows the good performance of the novel algorithm. Moreover, the results of this method enable the projection of a previously planned 3D roadmap onto the current DSA image for enhanced catheter guidance and data fusion.
- A hybrid registration technique is developed that rigidly aligns a 3D CTA vessel model to a 2D DSA image for liver catheterizations [57]. This method does not require user interaction intraoperatively and is thus particularly suitable for clinical use. Feature spaces are iteratively adjusted by the use of a probability map that links registration to 2D segmentation results. A Maximum

Likelihood formulation justifies the validity of the method. A novel technique for the creation of authentic simulated DSA images allows for accuracy and robustness tests in a controlled environment. Clinical tests as well as a new 3D roadmap visualization technique based on computed one-to-one correspondences show the high potential of this algorithm.

- For the first time, the difficult task of single-view 2D-3D deformable registration is addressed [165]. The approach addresses the inherent ill-posedness of the problem by incorporating a priori knowledge about the vessel structures into the formulation. The distance between the 2D points and corresponding projected 3D points is minimized together with regularization terms encoding the properties of length preservation of vessel structures and smoothness of the deformation.

2. Methodology

This section gives an overview of the theoretical background and methods for registering angiographic images. Basically, image registration tries to establish a path from input images, introduced in section 2.1, to an aligning transformation between them. Along this path there are several issues to resolve.

First, many methods have to extract features of interest to achieve the registration goal. In angiography, vessels are the features of major interest, whose extraction and quantification will be explained in section 2.2.

The second step is to establish a spatial relationship, a transformation, between the extracted features. This includes the finding of a one-to-one feature mapping, which is supposed to solve the correspondency problem. From corresponding features, a transformation can be computed by optimizing an energy term. The correspondency problem, the nature of energy terms and transformations, and optimization procedures will be the topic of section 2.3.

In section 2.4 we will refine the definition of image registration given in 2.3 to the particular case of 2D-3D registration and introduce a model with its parameters for the rigid case. We will also constrain the term rigid 2D-3D registration to the task of 2D-3D pose estimation, and give algorithms for testing, error analysis, and algorithm evaluation.

These four sections provide the methodological basis for the review of 2D-3D angiographic registration (chapter 3), and for the novel methods, which will be developed in Part II.

2.1. Images

Mathematically, an image \mathcal{I} is a function that maps a spatial location to a scalar value representing brightness or illumination:

$$\mathcal{I} : \Omega \rightarrow \mathbb{R}, \quad (2.1)$$

where $\Omega \subseteq \mathbb{R}^d$. Instead of brightness or illumination we use the term intensity throughout the thesis. Computer images are rasterized, i.e. spatial locations are distributed on a regular grid, the grid points are referred to as pixel/voxel. For simplicity, we will not use the term voxel, and indicate in the text if we address 2D, 3D, or higher dimensional images.

Linear Image Filtering The mathematical concept behind image filtering is the *convolution* of two functions f, g :

$$(f * g)(t) = \int_{-\infty}^{\infty} f(\tau)g(t - \tau)d\tau, \quad (2.2)$$

Images can be *enhanced* by filter application, e.g. a gradient filter enhances edges, a Gaussian filter smooths the image to suppress noise. Very often, a filter shall be applied to a derivative of an image, which can be achieved by building the derivative of the filter (which is usually smaller than the image) and filtering the image with the filter's derivative, reducing the overall computation cost (*differentiation commutes with convolution*) [141]. Moreover, accuracy can be increased since the derivative of the filter can usually be determined analytically.

Image Derivatives Images can be derived to extract gradient and Hessian of the underlying intensity-mapping function. Given an image \mathcal{I} , we will denote the gradient as $\frac{\partial \mathcal{I}}{\partial \mathbf{x}} = \nabla \mathcal{I}$, and the Hessian matrix as $\frac{\partial^2 \mathcal{I}}{\partial^2 \mathbf{x}} = \mathcal{H}_{\mathcal{I}}$.

Linear Scale-Space For image segmentation it is important to extract objects of different size from the image. Thus, segmentation algorithms often have to search for objects in all possible *scales*.

A concept which is often used for multi-scale representations of images is the linear scale-space introduced by Witkin [156] and thoroughly explored by Lindeberg *et al.* [86, 141]. Witkin proposed to treat scale as a further dimension of an image $\mathcal{I} : \Omega \rightarrow \mathbb{R}$:

$$\mathcal{T} : \Omega \times \mathbb{R}_+ \rightarrow \mathbb{R}, \quad (2.3)$$

where \mathcal{T} must fulfill the *causality* property [78], which basically means that new extrema must not be created in the scale-space representation. He also showed that moving along this scale dimension to point $s \in \mathbb{R}_+$ is equivalent to filtering an image with a Gaussian kernel with standard deviation $\sigma = s$ in order to suppress structures with a characteristic signal length of less than σ :

$$\mathcal{T}(\cdot, s) = G_\sigma(\cdot) * \mathcal{T}(\cdot, 0), \quad (2.4)$$

where G_σ is a Gaussian smoothing kernel with standard deviation $\sigma = s$ and zero mean,

$$G_\sigma(\mathbf{x}) = \frac{1}{(2\pi\sigma^2)^{N/2}} e^{-\mathbf{x}^\top \mathbf{x} / (2\sigma^2)}, \quad (2.5)$$

and $\mathcal{T}(\cdot, 0)$ is the original image data. The advantage of scale-space is to change scales on a fine-grained level and avoid localization errors since the resolution of the image is not altered, in contrast to e.g. image pyramids [22, 36]. It should be noted that intensity and its derivatives are decreasing functions of scale. For that, a normalizing factor can be introduced to make them comparable throughout scale-space, i.e.

$$\mathcal{T}(\cdot, s) = s^\gamma G_\sigma(\cdot) * \mathcal{T}(\cdot, 0), \quad (2.6)$$

where γ depends on the underlying model of shape and the feature (edges, corners, ridges) to be detected [80, 87].

In this section images were treated as continuous signals. Digitized images, however, have a discrete nature, which raises some issues in approximation and implementation of the aforementioned techniques. These issues can be found, shortly summarized, in appendix A.

2.2. Vessels in Medical Images

As already mentioned, many registration techniques need to work on features of interest, which are, in angiographic images, vascular structures. Even if so-called intensity-based methods (see 2.3.1) are used for angiographic image registration, vessels are usually extracted. In the following, we will give an introduction to enhancing vessels (see 2.2.2), initializing segmentation algorithms (see 2.2.3), which themselves will be subject to discussion in 2.2.4. For most methods, differential geometry analysis of the intensity mapping of vascular images is crucial, which is why an explanatory introduction of the Hessian matrix in angiographic images is given in 2.2.1. For the registration task, attaching attributes to segmented vasculature like centerline points, or vessel diameter is very important. Thus, the quantification of vascular structures will be focused on in 2.2.5.

Literature Lots can be found on vessel analysis from medical images, the body of research in this field is growing constantly. A good review up to 2002 is provided by Kirbas and Quek [76], a second one by Suri *et al.* [139, 140] considers vascular segmentation on MRA images. Techniques, however, are evolving still, and no exhaustive review has been published on this issue yet. The interested reader is referred to state-of-the-art sections of the latest works on vessel analysis, as there are for instance Gooya *et al.* [53], Schaap *et al.* [132], Manniesing *et al.* [98], or Yan and Kassim [159].

2.2.1. The Hessian in Vessel Analysis

The Hessian matrix of images plays a major role for model-based analysis of vessels. For the following explanation also refer to figure 2.1. Given a curvilinear structure in a 3D image (a tube) with radius r . A common assumption is that the intensity profile of a scan line orthogonal to the tube's axis follows a 1D Gaussian distribution with standard deviation $\sigma = r$, i.e. the highest (brightest) intensity is at the centerline of the vessel model¹. If we build the 2nd derivative of the intensity profile, we get a profile, which is minimal at the centerline point and has two zero-crossings at $\pm\sigma$, each at the border of the tubular structure. We can also transfer this intensity analysis to higher dimensions using the Hessian matrix. If we move the 3D image in scale space to $s = \sigma$ equal to the tube's radius, the *eigenvalues* ($\lambda_1 \leq \lambda_2 \leq \lambda_3$) and their associated *eigenvectors* ($\mathbf{v}_1, \mathbf{v}_2, \mathbf{v}_3$) of the Hessian at a point \mathbf{x} on the *centerline* of the tube have the following properties:

¹In fact, this is only true in scale-space where the appropriate smoothing step assures this intensity profile

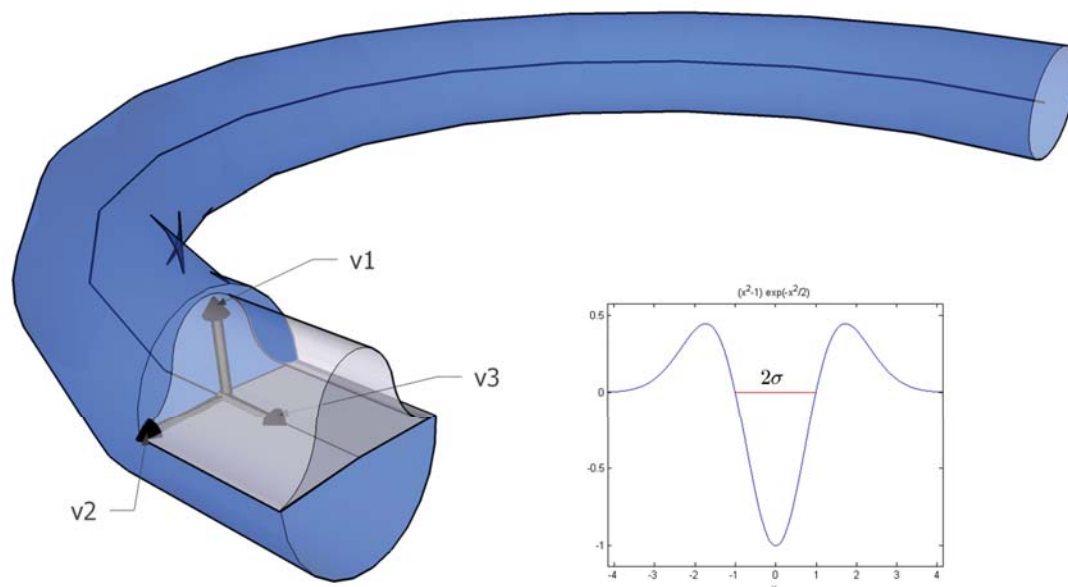


Figure 2.1.: A tubular model of a 3D vessel with a Gaussian intensity profile along a scanplane through the tube. The right image shows the 2^{nd} derivative of the Gaussian profile, where the doubled standard deviation, 2σ , connects the 2 zero-crossings.

- *Direction:* In a local neighborhood, the eigenvector associated with the largest eigenvalue (v_3) points in the direction of the tube.
- *Basis of orthogonal plane:* The two other eigenvectors $\{v_1, v_2\}$ form a basis of a plane that is orthogonal to the structure. The circle with center x and radius σ that lies in the plane spanned by these eigenvectors should describe the border of the vessel, i.e. the places with largest intensity change.²
- *Eigenvalue character:* On a centerline of a tube, λ_3 should be a positive value close to zero, λ_1 , and λ_2 negative, and of equal and high magnitude (minimal in a local neighborhood). Thus, when evaluated at arbitrary points y in the image, the eigenvalues give a good hint if y is on a centerline or not.

To summarize, with a proper analysis of Hessian eigenvalues we can detect candidate seeds of centerline points or enhance curvilinear structures in the image. With a proper usage of the eigenvectors, vessel walls can be detected and centerline points can be followed (on a 1D intensity ridge [40]). The same analysis as in 3D applies to 2D images, where one eigenvector vanishes and the orthogonal plane (formerly with basis $\{v_1, v_2\}$) collapses to a line (with direction v_1). The intensity profile can

²This is an approximative assumption since vessel sections can also be elliptic

also be inverted (i.e. dark instead of bright vessels), where a change of sign adjusts all algorithms based on Hessian analysis.

Hessian-based vessel analysis has its drawbacks as well. First, since scale-space is needed to operate on the Gaussian intensity profile, these methods are quite slow. Second, since 2D images only yield 2 eigenvalues for Hessian matrices, many derived filters (e.g. [47, 131, 98]) lose some criteria and can become unstable. Third, if the vessel radius becomes very small the computed eigenvalues become unstable.

2.2.2. Vessel Enhancement

Enhancing curvilinear structures in images is a crucial step for vessel segmentation and quantification. Especially if the segmentation algorithm does not take a model of a vessel into account, it is important to previously change intensities in order to sharpen vessel borders and reduce noise or artifacts in the background (see Figure 2.2).

For image and/or vessel enhancement, filters can be used to

- reduce noise in the image, typically Gaussian smoothing, or edge-preserving smoothing (e.g. anisotropic diffusion [119], or median filtering),
- remove background artifacts (e.g. bothat or tophat filtering [35, 34]), and
- enhance tubular structures (Hessian-based filters [47, 131, 91]).

Bothat and tophat filtering are based on grayscale morphology operators. The bothat filter applies a closing operation, that is a dilation (maximum filter), followed by an erosion (minimum filter). If an image with dark vessels³ is processed and the structure element is chosen to be larger than the largest vessel, the dilation should remove the vessels from the image and retain the background. Afterwards, the original image is subtracted from the closed version to get an image where non-vessel structures have been removed (see Figure 2.2b). The tophat filter [52] is the reversed version (original - opened image) of the bothat and creates the same output if applied to the inverted input image.

Hessian-based enhancements of tubular structures use, as explained above, the eigenvectors of the Hessian matrix to evaluate if a point is inside a curvilinear structure or not. For instance, Frangi *et al.* [47] create a *vesselness* image, where each pixel value contains the probability of belonging to a vessel or not (see Figure 2.2c). The filter calculates the exponential version of three (for 3D images) and two (for 2D images) eigenvalue-based criteria that distinguish curvilinear structures from other structures and noise. Manniesing *et al.* [98] encapsulate the vesselness filter of Frangi - adapted to be smooth also in the vicinity of zero - in a diffusion process to enhance tubular structures. An enhancement strategy similar to Frangi *et al.* is proposed by Sato *et al.* [131] deriving a response function from the ratios of combinations of eigenvalues. Lorenz *et al.* [91] propose to use the eigenvalues orthogonal to the vessel direction⁴ for enhancement combined with an edge-indicator in order to avoid

³as for example DSA images

⁴their arithmetic mean in 3D

detection of step edges. A comparison of Frangi, Sato, and Lorenz filters and the choice of normalization parameter γ in linear scale-space is described in Olabarriaga *et al.* [109].

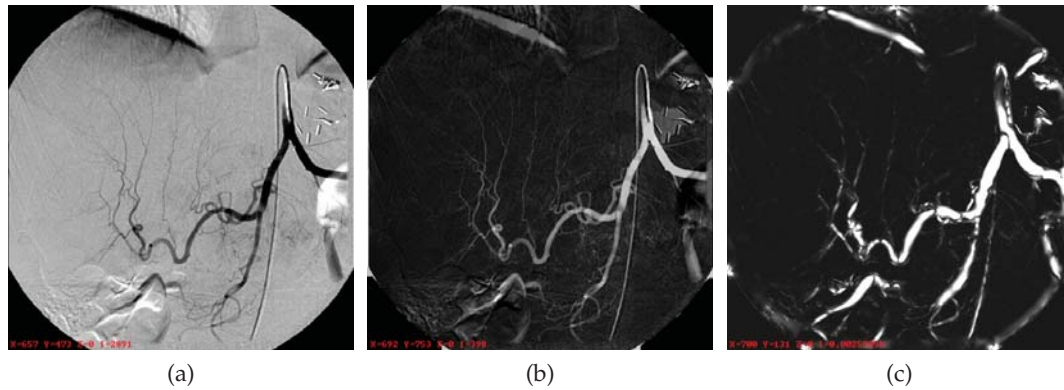


Figure 2.2.: Different enhancement filters applied to a DSA image (a). (b) shows a bothat filtered image, (c) shows a vesselness image as proposed by Frangi *et al.* [47]

2.2.3. Segmentation Initialization

Initialization of segmentation algorithms is crucial for automatic vessel analysis. A manual initialization can be acceptable for preoperative image data, however, intraoperatively, user interaction should be avoided. While some papers rely on a manual initialization subject to refinement (manual clicks in the vicinity of the centerline that are automatically shifted to the centerline), there are several methods to automatically detect candidates for centerline pixels.

Krissian *et al.* [80] detect pixels that are likely to lie on a 3D tubular centerline by requiring the two small eigenvalues v_1, v_2 of the Hessian to be negative.

An interesting approach by Can *et al.* [25] that is not based on Hessian analysis is to use an oriented filter, which is a mixture of a derivative (for edge detection) and a mean filter (for robustness against noise). Since the direction of the tube cannot be inferred by design as in the Hessian-based analysis, the filter must be evaluated in any direction (discretized with 16 different ones). Moreover, since scale-space is not involved, the filter is shifted outwards in a local neighborhood of the inspected point to account for vessel width. In each step, the filter is evaluated and certain criteria are checked. The criteria, derived from responses of two opposite edge detectors yielding a maximal value at the borders of the vessel, assure that the point where the filter is evaluated is a centerline point.

2.2.4. Segmentation

If we pick up definition 1.3 from chapter 1, segmentation is the partitioning of the image domain Ω into sets $S_k \subset \Omega$, which satisfy

$$\Omega = \bigcup_{k=1}^K S_k \quad (2.7)$$

where $S_k \cap S_j = \phi$ for $k \neq j$ and each S_k is connected [120].

In our scenario, we only have two classes, S_0 , the background, and S_1 , the vascular object, i.e. segmentation yields binary images. Segmentation will also be called *labeling*, where a label (*object* or *background* label in our scenario) is assigned to a pixel if it is a part of the vascular object, or the background, respectively, see Figure 2.3.

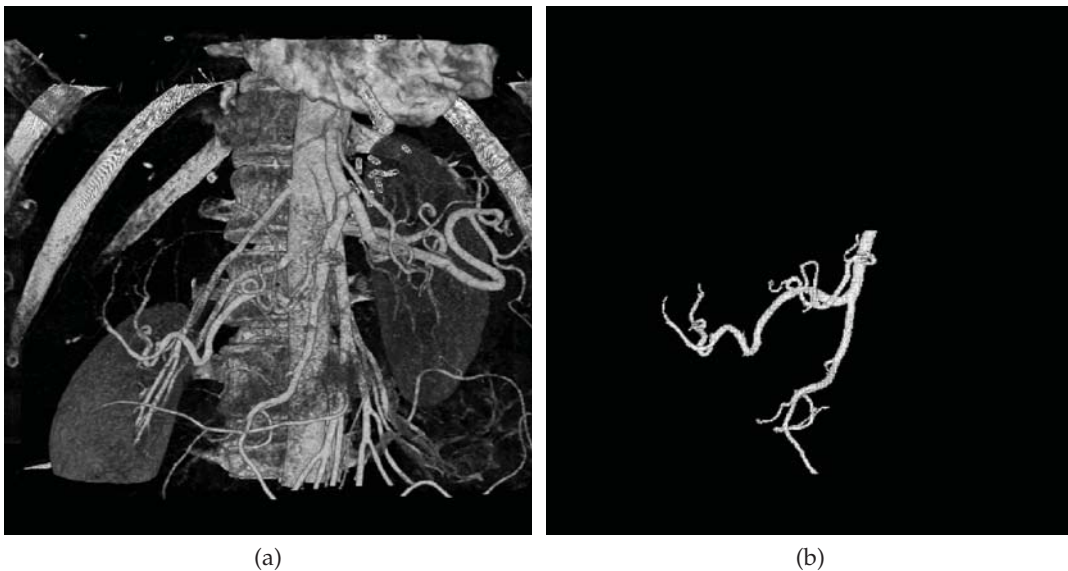


Figure 2.3.: (a) a volume rendering of a 3D CTA scan, (b) the segmented liver vasculature.

We identify two classes of segmentation algorithms that are interesting in our context, techniques based on Thresholding and Level Set methods.

Thresholding-Based Segmentation Methods Thresholding is a simple segmentation algorithm that assigns object labels to pixels with an intensity that lies within a specific range. The borders (thresholds) of this range can be determined manually or automatically as proposed for vessel segmentation of MRA TOF images by Wilson and Noble [155]. They model pixel intensities with different probability distributions and iteratively solve for a classification using a Gaussian mixture model and the EM algorithm [37].

Condurache *et al.* [34] propose a hysteresis thresholding method, which computes a hard and a weak threshold and shifts pixels from the low confidence level (given by the weak threshold) to the high confidence level (given by the hard threshold) via adjacency.

Region Growing or Connected Thresholding only considers pixels in the intensity range, which lie within the neighborhood of a seed point. It is suitable for segmentation of topologically connected objects, which generally can be assumed for vessel structures. Selle *et al.* [134] propose a region growing technique for vascular images, where the intensity range to be considered is automatically determined by sampling thresholds and calculating the point in threshold space where the number of pixels with object label significantly increases. At this point, it is assumed that the region growing “breaks out” of the vascular structure and accumulates surrounding tissue.

Level Sets Segmentation based on active contours [72, 158] has become famous in Computer Vision and Medical Image Analysis. The intuition behind active contours is to define a curve (the contour) and let it evolve in time depending on internal (smoothness) and external (image) forces. While early models use a parametric representation of the curve, Level Set methods [111, 26, 28] implicitly represent a curve as the zero Level Set of a higher dimensional function.

A Level Set method based on the evolution of a 1D curve in 3D for vessel segmentation has been proposed by Lorigo *et al.* [92], where the focus particularly lay on the extraction of small vessels that cannot be found by mere thresholding. A general problem of Level Set methods evolving 2D surfaces for elongated structures is their tendency to leakages where no high gradient is given. Deschamps *et al.* [38] introduce a freezing value for pixels indirectly proportional to their distance to the starting seed point. If a point is very near the starting point but still on the evolving surface of the curve, it is assumed to be at a vessel border and it is set fixed. Nain *et al.* [104] incorporate a soft shape prior into the Level Set formulation that penalizes leakages. The prior is based on a filter yielding a large response if evaluated in a segmented region with a radius larger as the largest expected vessel radius.

Current research on vessel segmentation using Level Sets tries to localize small vessels in MRA data sets continuing the work of Lorigo *et al.* [92]. Yan and Kassim [159] propose a Level Set formulation based on capillary forces in order to extract small vessels in MRA data. Their energy functional consists of several energy terms derived from the physics of capillarity. Gooya *et al.* [53] combine the Chan-Vese active contour model [28] with the maximization of the product of two statistical distances and a flux maximization flow as proposed by Vasilevskiy and Siddiqi [149].

2.2.5. Quantification

Quantification of vessel structures is a main issue for feature-based registration of angiographic images and a proper visualization. The main characteristics of vasculature that are subject to extraction are:

- *Centerline*: Since vessels have the structure of a tube, we are interested in its

centerline, i.e. the 1D curve that describes the geometric shape of the vessels.

- *Branching points*: The topology of vessel structures is described by bifurcations. Vessels often have a tree-like shape, where junctions are distinct and can thus be used for registration.
- *Diameter*: The width of the vessel tubes at all locations is an important criterion for matching and visualization.

For some applications, such as classification of stenosis width, an estimate of the vessel wall is desired [46], which we will not cover since the registration task does not require models of the vessel wall. Given segmented vessel structures, methods have been developed to extract all the aforementioned information. However, there are also direct methods, which quantify vessels based on grayscale information circumventing the sometimes tedious and error-prone segmentation steps. The quantification of both segmented and grayscale images will be discussed in the following.

Centerlines from Segmented Images Given binary images, centerlines can be computed by producing a *skeleton* as introduced by Blum [14], who constituted the well-known *medial axis transform* (MAT). A skeleton represents the medial axis, which is the set of centers and radii of the maximal disks that are contained within the object. There is a considerable body of research on skeletonization algorithms [13, 17]. Fast approximative algorithms have been proposed for skeletonization, usually referred to as topological *thinning* algorithms [82]. Thinning algorithms remove points from the segmented object if their deletion does not lead to topology change or shrinkage of the segmented object.

An effective thinning algorithm particularly tailored for tubular structures is proposed by Palagyi [113] (see Figure 2.4c). This sequential algorithm iteratively tests *border*⁵ points whether they are *simple*⁶ and *non-final*⁷, in which case they get removed. Special care is taken to symmetrically thin the structure by processing only one direction (north, south, east, west, and, for 3D, also bottom, and top) at a time.

A similar approach was proposed by Selle *et al.* [134] who guarantee the symmetric thinning by only removing simple points in the current pass if they have the same value in a Euclidean distance map [16] (see Figure 2.4a) computed on the segmentation.

In general, skeletonization algorithms do not yield the centerline of tubular structures, but introduce spurious branches, which have a smaller length than the diameter of the vessel in which they are located (see Figure 2.4c). In order to remove these spurious branches, the analysis of a distance map can be used. For instance, branches with a length smaller than 2 times the diameter of the outgoing bifurcation can be deleted. Or, as proposed in Selle *et al.* [134], pixels of the thinned structure whose

⁵A point with object label is called border if it is 6-adjacent (in 3D, 4-adjacent in 2D) to at least one background point

⁶A point is called simple if its removal does not change the shape's topology. For a formal definition refer to [97]

⁷A point is called non-final if it has more than one object neighbor

gradient magnitude in the distance map of the segmentation is not near to zero can be discarded, assuming that only centerline pixels lie on a prominent intensity ridge of the map.

Ridge Detection and Traversal Since we are often only interested in centerlines and vessel diameters, approaches have been proposed to directly extract this information from greyscale images without segmenting the image.

Referring to the figure of a tube model (Figure 2.1), the intensity profile on a scan-plane orthogonal to the tube describes a *1D intensity (height) ridge* in 2D [40]. In 3D, there is also a 1D ridge following the centerline of the tube, but cannot be visualized as easily as the 2D pendant. Such ridges can be detected and traversed in the direction of the tube. The detection of intensity ridges on images can also be interpreted as finding the medial axis on grayscale images, as proposed by Wang *et al.* [153] for 2D images. Here, the MAT is based on maximal gradient responses from opposing boundaries (*gradient medial axis transform, GRADMAT*).

The group around S. Pizer laid the theoretic foundations of the detection of 1D intensity ridges⁸ by formally defining *medialness* for grayscale images, thus extending the definition of Blum [14]. Similar to Wang *et al.* [153], a measure for medialness can be derived by accumulating responses from opposing boundaries [121]. The measure is maximal at ridge points and thus suitable for detection.

Ridge traversal is achieved by moving along the ridge's tangent direction, which can be approximated by the largest eigenvalue of the Hessian matrix [6].

The detection and traversal of ridges in vessel shapes yield the centerlines of the vessels, directly inferring a quantification of vessel structures, see Figure 2.4b. Ridge detection is run in linear scale-space where the standard deviation of the Gaussian filter σ is equal to the radius of the vessel whose centerline has been detected. Since ridge detection and traversal yields two of three quantification results of vessel analysis without explicitly segmenting the structure, it has received a lot of attention in the Medical Image Analysis community.

For ridge detection, usually gradient and Hessian information of the image is mixed (gradient for extremum/boundary detection, Hessian eigenvectors for directional information). Given a 3D image \mathcal{I} , the gradient $\nabla\mathcal{I}$, the Hessian $\mathcal{H}_{\mathcal{I}}$, their eigenvalues $(\mathbf{v}_1, \mathbf{v}_2, \mathbf{v}_3)$ together with their corresponding ordered eigenvalues $\lambda_1 \leq \lambda_2 \leq \lambda_3$. As pointed out in the discussion in section 2.2.1, a ridge point has to fulfill certain conditions in an intensity profile with bright vessel structures [40]

- (i) *Eigenvalues*: The eigenvalues of the eigenvectors orthogonal to the tube must be negative.

$$\lambda_1 \leq 0 \text{ and } \lambda_2 \leq 0 \quad (2.8)$$

- (ii) *Optimum*: The ridge point must be an intensity maximum in the directions orthogonal to the tube. Thus, the projection of the gradient at a ridge point

⁸Together with the scales (radii) where they have been detected, 1D intensity ridges were also dubbed as cores [50]

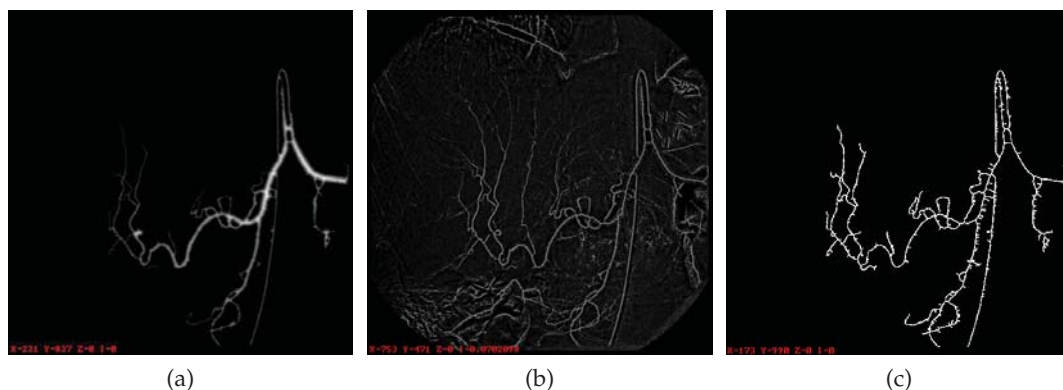


Figure 2.4.: (a) 2D Distance Map of a segmented DSA image (original: Figure 2.2a), (b) ridges responses as described in Koller *et al.* [79], (c) thinned image applied to a segmentation of (a) using the method of Palagyi *et al.* [113].

onto the directions $(\mathbf{v}_1, \mathbf{v}_2)$ must be zero at scale s for a tube with radius s :

$$\mathbf{v}_1^\top \nabla \mathcal{I} = 0 \text{ and } \mathbf{v}_2^\top \nabla \mathcal{I} = 0 \quad (2.9)$$

Using these criteria, ridge points and thus vessel centerlines can be detected [6]. In 2D, only two instead of four criteria are tested.

Approaches by Koller *et al.* [79] and Krissian *et al.* [80] derive a filter response from gradient and Hessian. Both methods use the fact that the gradient should be high at the boundaries of the tubular structure, if it is measured orthogonal to the axis of the tube. At scale s , they measure the rate of intensity change along a direction orthogonal to the tube by

$$R(\mathbf{x}) = \min (\nabla \mathcal{I}(\mathbf{x} \pm s\mathbf{v}_{1|2})^\top \mathbf{v}_{1|2}), \quad (2.10)$$

in [79] and

$$R(\mathbf{x}) = \int_{\alpha=0}^{\alpha=2\pi} \nabla \mathcal{I}(\mathbf{x} \pm s\mathbf{v}_\alpha)^\top \mathbf{v}_\alpha, \quad (2.11)$$

where $\mathbf{v}_\alpha = \cos \alpha \mathbf{v}_1 + \sin \alpha \mathbf{v}_2$ in [80].⁹

Again, the same criteria and response functions can be applied to 2D images, collapsing the circle described by \mathbf{v}_α to a line and probing two points $(\mathbf{x} \pm s\mathbf{v}_1)$ on this line.

The approach by Frangi *et al.* [46] finds ridges by fitting a 1D B-spline curve (which is created manually) to the underlying data using an active contour model [72]. Internal forces account for smoothness of the curve while external forces attract the curve toward a maximal vesselness filter response [47] and thus an intensity ridge.

The drawback of methods based on intensity ridges is that branching points cannot be detected easily since the filter responses are not high and ridge criteria do not hold at bifurcation points.

⁹In both Equations \mathbf{v}_i must be normalized.

Detection of Branching Points Detecting the bifurcations of vessel structures is of major interest for registration algorithms, since junctions represent distinct features, which can be used for matching. Given a segmented or thinned vasculature and a seed point, a wave can be defined propagating through all object pixels and testing for connectivity of the front. This *wave propagation* algorithm has been proposed by Zahlten *et al.* [162] for the use in hepatic vessel analysis. Size and direction of the wave have to be computed in each step if no centerline was extracted before.

Fridman *et al.* [50] detect branches with a cornerness measure derived from the image gradient and the main direction of curvature (eigenvector \mathbf{v}_3 of the Hessian). The removal of false positives can be achieved by monitoring absence of a rapid change of medialness responses in a local neighborhood of the current ridge point.

Krissian *et al.* [80] detect junctions in vessel structures by analyzing the distance of adjacent vessel segments. If the distance between the endpoint of a vessel and the axis of a second vessel is smaller than the radius of the second vessel, a junction has been detected and the vessel segments are connected.

Diameter Computation Approaches that operate in linear scale-space have the nice side-effect that the standard deviation of the current Gaussian kernel, σ , at which a maximal response or ridge is detected, is equal to the radius of the vessel at that ridge point [86].

If the centerline has been extracted from a segmented image, we can also measure the diameter using a distance map [16] yielding the Euclidean distance to a contour of the segmentation (Figure 2.4a). If we assume, due to errors in the extraction process, that the centerline point is not located exactly in the middle of the segmented tube, we can optimize the diameter computation by searching for the highest value on the distance map perpendicular to the centerline direction.

2.2.6. Suggestions for Method Selection

The choice of the right vessel analysis method is very dependent on modality and purpose. Current research is focused on detection of small vessels in 3D (mostly MRA and CTA) images, where the purpose is mostly visualization and diagnosis. When it comes to intraoperative navigation (and feature-based registration), fast methods have to be used that require little interaction and deliver results of reasonable quality also on 2D images, whose vessel extraction is, due to lower SNR and dimension and thus less information, not easier.

The purpose also chooses the method since a segmentation is only required in visualization and measurements on vessel walls, while for registration tasks, a quantitative analysis yielding topology (in terms of bifurcations), centerlines, and vessel diameter, is often sufficient (which can be achieved without segmentation as in ridge traversal techniques).

Thresholding or region growing methods are usually computationally efficient and yield decent segmentation results on 2D and 3D vascular images. However, region growing requires seed point initialization and both techniques suffer from the absence of a model, which often leads the algorithm to oversegmentation. A

conservative choice of the threshold can avoid this effect, but the result will not give the complete vascular tree making these methods not very suitable for a diagnostic purpose. Combining thresholding techniques with the appropriate (model-based) filter enhancement and an automatic seed point detection can circumvent these drawbacks in order to have a good trade-off between computational efficiency and accuracy.

A general problem in Level Set and Ridge Traversal methods is to deal with ramification locations. At these points, sharp corners¹⁰ are penalized by the Level Set approach since the low curvature of an evolving curve or surface is not given. Moreover, the inherent possibility of topology changes of Level Set methods, making them so powerful, is not desired in the context of vessel analysis assuming vessel structures to be connected. Ramifications cannot be detected by ridge traversal methods since the intensity ridge is not distinct at these locations. Thus, such methods tend to require several starting seeds or reinitialization phases, which, to this end, cause further user interaction. The computational cost of Level Set methods and multi-scale approaches must not be underestimated since time is a critical issue especially intra-operatively. Both methods tend to require the fine-tuning of a number of parameters that need to be adjusted for each modality. However, the ability to deal with smaller vessel branches, which cannot be located by thresholding-based techniques, make Level Set and Ridge Traversal methods interesting due to their accuracy: the local injection of contrast and magnification yields vessels in 2D whose corresponding 3D vessels are very small. Their detection in 3D would improve 2D-3D registration algorithms in accuracy and robustness.

2.3. Medical Image Registration

After the introduction of vessel extraction and quantification techniques, which provide the features for angiographic registration, the process of using these features for alignment, i.e. registering the underlying images will be focused.

Definition The process of image registration tries to find a transformation between two or more images. In this thesis, we will constrain the registration task to two images, the more general registration of multiple images, also referred to as mosaicking, will not be discussed.

Definition 2.1 (Registration of 2 Images) *Given two images $A : \Omega_A \rightarrow \mathbb{R}$ and $B : \Omega_B \rightarrow \mathbb{R}$ and a set of admissible transformations $\varphi : \Omega_A \rightarrow \Omega_B$, image registration is the computation of a transformation φ' that aligns A to B such that a certain comparison criterion, an energy \mathcal{E} , is minimized:*

$$\varphi' = \arg \min_{\varphi} \mathcal{E}. \quad (2.12)$$

¹⁰which usually occur at these junctions

The choice of the energy depends on the set of admissible transformations. The energy \mathcal{E} , also called *error*, or *cost function*, always contains a *data term* \mathcal{D} , which measures the quality of fit of the two data sets given a transformation. Moreover, as will be discussed in section 2.3.2, \mathcal{E} can impose constraints on the set of admissible transformations if it is not restricted by a model. The notion of *correspondency* is strongly related to image registration. The input data must have corresponding information in order to compute the transformation and evaluate a data term. Establishing these correspondences depends on the technique chosen to register the images and will be discussed in section 2.3.3. Since we try to find a minimum of a function (\mathcal{E}), we also need to incorporate some kind of optimization into our registration algorithm. Suitable techniques will be addressed in section 2.3.4. Section 2.4 will provide details of the necessary modifications and extensions that have to be applied when moving to multi-dimensional registration, in particular 2D-3D registration.

Literature A good introduction into basic concepts and algorithms of medical image registration is given in the book *Medical Image Registration* [61]. A thorough categorization of registration techniques is presented by Maintz and Viergever [95] in their *Survey of Medical Image Registration*. An interesting work is also the book *Numerical Methods for Image Registration* [103], showing registration concepts from a rather mathematical and general, but comprehensive and thorough point of view.

2.3.1. Data Terms

Image Registration can be approached in at least two different ways. Either image features are extracted and the registration is performed based on the extracted spatial information. This approach is referred to as *feature-based* registration. The second technique directly performs the registration on the image intensities without requiring a previous feature extraction step. We usually speak of *intensity-based* registration to address the latter approach. The difference between intensity- and feature-based registration is the choice of data term \mathcal{D} .

Similarity Measures Intensity-based techniques use the intensity mapping of the images to define a *similarity measure* (SM) as data term \mathcal{D}_S . If $H_A = \{h_A | h_A : \Omega_A \rightarrow \mathbb{R}\}$ and $H_B = \{h_B | h_B : \Omega_B \rightarrow \mathbb{R}\}$ are spaces of images \mathcal{A} and \mathcal{B} respectively, a similarity measure can be described as

$$\mathcal{D}_S : H_A \times H_B \rightarrow \mathbb{R} \quad (2.13)$$

For these similarity measures to be evaluated, the image must be transformed together with its intensities, which brings up the issue of interpolation. Correspondency is assumed to exist at every pixel location in an overlapping region, and the similarity measure calculates the quality of fit given this correspondency induced by transformation φ . Usually three categories are distinguished between similarity measures: *difference-based measures* calculating a function of the difference of intensity at each location, *correlation-based measures* computing the statistical correlation of

intensities¹¹, and *entropy-based measures*, determining the amount of signal entropy between the two images¹². For a good overview and mathematical definitions of similarity measures, refer to [62].

Distance Measures Feature-based methods typically minimize a *distance measure* \mathcal{D}_D accumulated over all extracted features $\mathcal{F}_i^A \in \Pi_A, i = 1 \dots n$, and $\mathcal{F}_j^B \in \Pi_B, j = 1 \dots m$, where Π_A, Π_B are feature spaces of \mathcal{A}, \mathcal{B} , respectively. \mathcal{D}_D is usually defined via a metric $d(\cdot, \cdot)$ induced on the feature spaces, and an operator \mathcal{C} assigning correspondences:

$$\mathcal{D}_D = \sum_{i=1}^n d(\mathcal{F}_i^A, \varphi(\mathcal{C}(\mathcal{F}_i^A, \{\mathcal{F}_j^B\})))^2, \quad (2.14)$$

where $\{\mathcal{F}_j^B\} \subset \Pi_B$ is a finite subset of features from image \mathcal{B} , and $\mathcal{C}(\mathcal{F}_i^A, \{\mathcal{F}_j^B\}) = \mathcal{F}_k^B$, if feature \mathcal{F}_i^A corresponds to feature \mathcal{F}_k^B . Correspondences can be established in a previous step, or during the registration procedure (see section 2.3.3). Mind that features can be anything extractable from images, for which a distance function can be defined and correspondence can be established. Common features in medical image registration include points, lines, (parameterized) curves, or (triangulated) surfaces.

Commonly used distance measures are *Euclidean* and the more general *Mahalanobis* distance, both defined on points in Euclidean space \mathbb{R}^n . Since most features can be sampled by points, these are the most frequently used distance measures for Medical Image Analysis and will thus be formally introduced.

Definition 2.2 (Euclidean distance) *The Euclidean distance of two points $\mathbf{X} = (x_1, \dots, x_n)^\top$ and $\mathbf{Y} = (y_1, \dots, y_n)^\top$ is defined as*

$$d(\mathbf{X}, \mathbf{Y})_2 = \sqrt{(\mathbf{X} - \mathbf{Y})^\top (\mathbf{X} - \mathbf{Y})} = \sqrt{(x_1 - y_1)^2 + \dots + (x_n - y_n)^2}. \quad (2.15)$$

Note that two points must have the same dimension for the Euclidean distance to be evaluated.

The Mahalanobis distance takes the statistical distribution of points into account. Intuitively, this distance emphasizes the statistical contribution of the different entries of two points in \mathbb{R}^n to the distance measure. *Weighting* factors of the entries, expressed by their (co-) variances, are included in the distance measure.

Definition 2.3 (Mahalanobis distance) *Given two points $\mathbf{X} = (x_1, \dots, x_n)^\top$ and $\mathbf{Y} = (y_1, \dots, y_n)^\top$, interpreted as random vectors with covariance matrix $\Sigma \in \mathbb{R}^{n \times n}$, the Mahalanobis distance is given by*

$$d(\mathbf{X}, \mathbf{Y})_\Sigma = \sqrt{(\mathbf{X} - \mathbf{Y})^\top \Sigma^{-1} (\mathbf{X} - \mathbf{Y})} \quad (2.16)$$

¹¹making the measure independent of linear intensity changes

¹²particularly suitable for inter-modality registration

Of course, the choice of the distance measure should match with the chosen features to align. For instance, the distance of curves in \mathbb{R}^n can be measured with the Hausdorff or the Fréchet distance [2]. However, since such distance measures are sometimes costly to compute (e.g. they require a parameterization) or are sensitive to outliers, and since all geometric features can be sampled by a set of points, very often only the sum of the distances of each point in \mathcal{F}^A to the nearest point in \mathcal{F}^B is calculated. If \mathcal{F}^A can be sampled by set $\{\mathbf{X}_i\}, i = 1, \dots, n$, and \mathcal{F}^B can be sampled by set $\{\mathbf{Y}_j\}, j = 1, \dots, m$, a distance can be defined by

$$D(\{\mathbf{X}_i\}, \{\mathbf{Y}_j\}) = \sum_{i=1}^n \min_j d(\mathbf{X}_i, \mathbf{Y}_j), \quad j = 1, \dots, m, \quad (2.17)$$

where $d(., .)$ is the Euclidean or Mahalanobis distance. Moreover, building a distance map [16] of special distance metrics is not possible as they are not defined on all points on a grid resembling an image. Thus, improvements in performance via distance look-up, which are important for many feature-based registration methods, are very difficult to achieve when not using point-based distance measures.

To summarize, intensity-based methods are approaches defined by means of similarity and interpolation, while feature-based methods are techniques defined by means of distance and correspondence.

2.3.2. Transformations

In general, we can distinguish between *global* transformations, where φ follows a pre-defined global model, and *local* transformations, where φ is less restricted by design, but the energy \mathcal{E} constrains its behavior.

Global Transformations There are a number of transformation models used in Medical Image Analysis, which define a mere *global* transformation, discarding any deformation movement in data sets. We will briefly introduce the most important mono-dimensional mappings. The projection, a global transformation mapping from a higher to a lower dimension, will be subject to more attention in section 2.4 as it is the focus of this work. The other models are introduced since the 2D-3D model can be derived from them.

If a global transformation model is used, the set of admissible transformations is constrained by design and the energy term \mathcal{E} from Equation (2.12) only contains the data term \mathcal{D} , rendering the registration problem as:

$$\varphi' = \arg \min_{\varphi} \mathcal{D}. \quad (2.18)$$

A simple transformation model relies on the assumption of a global rigid movement. That is, all objects that ought to be registered do not change shape, only their pose changes. Moreover, objects in the observed scene change their pose accordingly. Thus, the transformation can be casted as a global rotation and translation, which is applied to all points $\mathbf{X} \in \Omega_A$ in the image domain:

$$\varphi(\mathbf{X}) = \mathbf{R}\mathbf{X} + \mathbf{t}, \quad (2.19)$$

where \mathbf{R} is a rotation matrix and \mathbf{t} a translation vector. In 3D, $\mathbf{R} \in SO(3)$ can be defined via different parameterizations, e.g. Euler angles, unit quaternions, or axis-angle representation. These parameterizations express the three degrees of freedom (DOF) either by three parameters, or by four parameters and an additional constraint. Details of parameterizations are not immediate subject to discussion in this section. However, since the choice of rotation parameterization is important for implementation issues of the proposed methods, we refer the reader to appendix C, where our choice of parameterization, Euler Angles, is justified. A 3D rigid transformation sums up to 6 DOF (3 for rotation, 3 for translation). Sometimes, an isotropic scaling factor is also added to the rigid model in order to account for different pixel sizes of \mathcal{A} and \mathcal{B} . We will discard this scaling since we assume \mathcal{A} and \mathcal{B} to be resampled adequately, or their extracted features to be given in mm.

There are other global transformation models, which soften the rigidity constraints of Equation (2.19).

The *affine* transformation model allows for shearing and anisotropic scaling additional to the rigid transformation. It is often used as a local approximation of a projective warp.

The *projective* transformation model¹³ is the most general global *linear* transformation and is simply a linear mapping that must be invertible. This definition is also called a *homography* as defined e.g. in [66].

As described by Rueckert [63], there are also non-linear global models, but they are not frequently used in Medical Image Analysis and are thus not discussed.

Except for the rigid model, there is in general no reason why medical data should transform according to a more general global model. Using these less restrictive global models in image registration is either an approximation to the more general set of local transformations that describe e.g. tissue deformation, or applied to very special problems like pixel size correction [67] or gantry angle estimation [138]. However, since deformable registration (and thus local transformation models) has received more attention and is better understood, current works tend to either use the most restrictive rigid model to register objects that do not change shape (as, e.g., bones) or to initialize a deformable refinement, or they use the most general local transformations (introduced below) to register deformable objects.

Local Transformations In contrast to global transformation models, local transformations do not restrict the movement of spatial locations in the first place.

By applying local transformations, which are also called displacement fields, spatial locations can be transformed (*displaced*) arbitrarily, which emphasizes the ill-posedness¹⁴ for the registration process using these types of transformations. In

¹³not to be mixed up with the projection transformation model

¹⁴Informally defined, a registration problem is ill-posed if a) no solution exists, or b) it has no unique solution, or c) if small changes in input lead to large changes in output. For a formal definition of well-posedness and its contrary refer to [60]

order to counteract this inherent ill-posedness, restrictions are imposed on the transformations. These restrictions shall avoid “unnatural” transformations, i.e. a tearing or folding of spatial locations must not happen.

A mathematical way of defining transformations that fulfill these restrictions is the notion of *diffeomorphism*, see for example [84, 18]:

Definition 2.4 (Diffeomorphism) *Given two manifolds M and N , a bijective map f is a C^r diffeomorphism if both $f : M \rightarrow N$ and its inverse $f^{-1} : N \rightarrow M$ are r times continuously differentiable.*

From this definition, we can deduce a local behavior of diffeomorphisms, which is more intuitive for our means:

Theorem 2.5 (Local behavior of diffeomorphisms) *If U and V are two open subsets of \mathbb{R}^n , a differentiable map f from U to V is a diffeomorphism at point \mathbf{x} if*

- (1) f is bijective
- (2) the derivative of f at \mathbf{x} is invertible (has a non-zero determinant of the Jacobian)

Theorem 2.5 can be shown via the theorem of inverse functions, but is not within the scope of this thesis.

The bijection assures an invertibility of f , while the invertibility of the derivative assures a smoothness of the mapping. Of course, a projection can never be a diffeomorphism since its derivative cannot be invertible.

In practice, these diffeomorphisms are rather difficult to construct and impose on different transformations. Thus, the diffeomorphic rule is sometimes loosened and transformations are only required to be sufficiently smooth, i.e. the derivative of the transformation is to be “well-behaved”, but φ and its derivatives are not necessarily invertible. This smoothness criterion is incorporated into the energy \mathcal{E} additionally to the data term and Equation (2.12) becomes

$$\varphi' = \arg \min_{\varphi} \mathcal{D} + \alpha \mathcal{S}, \quad (2.20)$$

where \mathcal{D} is the data term depending on the input data, and \mathcal{S} is a smoothing term imposing constraints on the set of admissible transformations φ . The scalar α is a *regularization* parameter controlling the influence of the smoothing criterion.

Typically, the smoothing term \mathcal{S} is a function of the derivatives of φ . A popular choice of \mathcal{S} is the *diffusion regularization term* [154, 103] penalizing for the sum of the first derivatives of φ :

$$\mathcal{S}_D = \sum_{i=1}^n \int_{\Omega} \|\nabla \varphi^{(i)}\|^2, \quad (2.21)$$

where $\nabla \varphi^{(i)} \in \mathbb{R}^n$ is the gradient w.r.t. \mathbf{X} of the transformation in dimension i .¹⁵

¹⁵Mind that φ is a vector-valued function, and its first derivative is a Jacobian matrix $\mathbf{J} \in \mathbb{R}^{n \times n}$.

Since the diffusion regularization term is sensitive to affine transformations, which is not desired in some scenarios (where the unknown transformation also includes a rigid part, for example a rotation), a regularization term that penalizes the *curvature* of the displacement field has been proposed

$$\mathcal{S}_C = \sum_{k=1}^n \int_{\Omega} \sum_{i=1}^n \sum_{j=1}^n \left| \frac{\partial^2 \varphi^{(k)}}{\partial x_i \partial x_j} \right|^2, \quad (2.22)$$

where $\frac{\partial^2 \varphi^{(i)}}{\partial x_i \partial x_j}$ is the the second derivative with respect to x_i and x_j . This regularization term is often called *bending energy* [128] or *Thin-Plate energy functional* (see Appendix B, Equations (B.3) and (B.4)) and inherently permits affine transformations, since $\mathcal{S}_C(\mathbf{A}\mathbf{x} + \mathbf{t}) = 0$. This term must not be mixed up with a so-called *curvature regularization term*, $\sum_{i=1}^n \int_{\Omega} |\Delta \varphi^{(i)}|^2$, as proposed by Fischer and Modersitzki [42], which leaves out the mixed terms of the second derivatives and is an approximation to \mathcal{S}_C ¹⁶.

Other regularization terms have been proposed in the literature, partly based on physical properties, but are not subject to discussion here. For a summary of frequently used regularization terms, refer to [103].

In Medical Image Analysis, diffeomorphisms and their (regularizing) approximations are called *deformations*, thus the term *deformable registration*.

Parametric vs Non-parametric Transformations We can distinguish between transformations expressed with or without parameters, raising the terms *parametric* and *non-parametric* registration.

Parametric transformations use *models* of a transformation which are expressed with a set of (few) parameters. If these parameters are known, they can be put into the transformation model and all spatial locations can be transformed. Global transformations are always based on models and thus belong to this class of transformations.

Particularly suitable for feature-based deformable registration are Thin Plate Splines (TPS), and their diffeomorphic extension, *Geodesic Interpolating Splines* [24], since they can register features with arbitrary locations, are minimizing the Euclidean (or Mahalanobis) distance between features, and keep the transformation smooth by minimizing the Thin Plate energy functional. See Appendix B for mathematical derivation, numerical computation, and application of TPS to Medical Image Analysis.

There are also other models that are often used for deformable registration. Free Form Deformations (FFD) are used to interpolate transformations defined on a regular grid. B-spline interpolants [128], also shown to yield diffeomorphisms [30, 127], are typically used for intensity-based registration, since they offer a smooth interpolation with local support¹⁷. Due to their local support, FFDs only yield meaningful deformations if a set of features is well distributed over the whole image domain. Thus FFDs are not very suitable for feature-based registration.

¹⁶ Δ is the Laplace operator, i.e. the sum of second derivatives without the mixed terms

¹⁷meaning that a grid node only influences the transformation in a local neighborhood

Non-parametric transformations do not consider a model of the transformation, but only address the transformation φ as a function. Solving for this function is the task of image registration. Since the energy of Equation (2.12) depends on φ , \mathcal{E} becomes a *functional*, which is to be minimized. The minimization of functionals, which includes the calculus of variations, is not in the scope of this thesis, but the reader is referred to Modersitzki [103] for introduction and to Zikic [164] for a numerical solution of this problem.

2.3.3. Correspondences

With transformation φ' from Equation (2.12) we want to reestablish the *correspondency* between images \mathcal{A} and \mathcal{B} . Correspondency can be specified in terms of anatomical corresponding features, image-based feature correspondences, or pixel correspondences.

As already mentioned, in intensity-based approaches, correspondency is assumed to be given at every pixel location in a region where the two images overlap, i.e. $\Omega_{\mathcal{A},\mathcal{B}} = \{\mathbf{x} \in \Omega_{\mathcal{B}} | \varphi^{-1}(\mathbf{x}) \in \Omega_{\mathcal{A}}\}$ [61], and fully depends on the given transformation. That means a pixel location of the first image corresponds to the nearest pixel location of the transformed second image.

In feature-based approaches, the correspondence problem is more important and is thus subject to discussion in the following. Here, correspondency can be¹⁸ regarded as being dual to transformation: Given two sets of features $\mathcal{F}^{\mathcal{A}} \in \Pi_{\mathcal{A}}$ extracted from \mathcal{A} and $\mathcal{F}^{\mathcal{B}} \in \Pi_{\mathcal{B}}$ extracted from \mathcal{B} . If correspondency is given for $\mathcal{F}^{\mathcal{A}}$, $\mathcal{F}^{\mathcal{B}}$, usually we can determine the transformation φ . Vice versa, if φ is given, we can establish correspondences for the whole image domains $\Omega_{\mathcal{A}}, \Omega_{\mathcal{B}}$, and hence for $\mathcal{F}^{\mathcal{A}}$, $\mathcal{F}^{\mathcal{B}}$. A good review of existing algorithms for finding feature correspondences can be found in Chui *et al.* [31].

Mathematically, the problem to solve is to find a bijective or one-to-one mapping between the feature sets $\mathcal{F}^{\mathcal{A}}, \mathcal{F}^{\mathcal{B}}$. This problem was casted as a *graph matching* or *quadratic assignment* problem by Shapiro and Haralick [135], see also Gold and Rangarajan [51].

Given two graphs $G = (V_G, E_G)$ and $g = (V_g, E_g)$, where $V_G = \mathcal{F}^{\mathcal{A}}$ and $V_g = \mathcal{F}^{\mathcal{B}}$, and E_G, E_g express a relationship of features, which lie in the *same* feature set¹⁹. We want to find a bijective mapping $f : V_G \rightarrow V_g$, such that the relationships of corresponding features are most similar, i.e. we want to find \mathbf{M}, \mathbf{M}' that minimize

$$- \sum_a \sum_b \sum_i \sum_j M_{ai} M'_{bj} C_{aibj}, \quad (2.23)$$

where \mathbf{M} and \mathbf{M}' are permutation matrices, i.e. $M_{ai} = 1$ if feature $\mathcal{F}_a^{\mathcal{A}}$ corresponds to $\mathcal{F}_i^{\mathcal{B}}$ and $M'_{bj} = 1$ if $\mathcal{F}_b^{\mathcal{A}}$ corresponds to $\mathcal{F}_j^{\mathcal{B}}$, respectively, otherwise they are 0. $C_{aibj} = 0$ if $(a, b) \notin E_G$ or $(i, j) \notin E_g$, otherwise they express a cost of how good the relationships of the two feature tuples fit.

¹⁸loosely

¹⁹Such a relationship can for instance express the geometric or topological configuration of a feature set.

The problem of quadratic assignment is \mathcal{NP} -hard, which is basically due to the comparison of relationships. The Computer Vision community has come up with different methods to circumvent the graph matching. We can distinguish between two different classes of approaches.

Feature Descriptors Instead of comparing relationships, one can compare a scalar cost C_{ij} yielding the *quality of correspondence* between two features $\mathcal{F}_i^A, \mathcal{F}_j^B$. This reduces the graph matching problem to a weighted bipartite graph matching or linear assignment problem (LAP). Now, we want to minimize the cost

$$- \sum_i \sum_j M_{ij} C_{ij}, \quad (2.24)$$

which can be solved in polynomial time [115]. The cost matrix \mathbf{C} can be established using feature descriptors, which, in order to be suitable for feature-based registration, usually have to be translation-, rotation-, scale-, and in the case of 2D-3D registration projection-invariant. Feature descriptors have become rather popular in the Computer Vision community [93, 85, 8], however, they are not frequently used in Medical Image Analysis. This is most probably due to higher variations of input data, and the rather restricted applicability of feature descriptors fulfilling all the aforementioned invariants.

Alternating Approaches By using the “duality” between transformation and correspondency, different methods have been proposed to alternate between correspondence detection and transformation estimation. Most of these approaches use a closest point distance measure (Equation (2.17)) to update the correspondency, and then reestimate the transformation. These closest point distance measures are not optimal in the sense of linear assignment, but they are generally faster, easier to implement, and yield a good approximation to the solution of Equation (2.24). Two algorithms that are frequently used in the Medical Image Analysis community are the *Iterative Closest Point* (ICP) algorithm proposed by Besl and McKay [11] and Zhang [163], and the *Robust Point Matching* (RPM) algorithm proposed by Chui and Rangarajan [31]. Due to its applicability to 2D-3D registration and its nice theoretical properties, we will have a closer look at the former method.

The Iterative Closest Point Algorithm The task is to rigidly register two sets of 3D²⁰ features (surfaces, curves, point clouds) sampled by point sets $\mathbf{X}_i \in \mathcal{F}^A, i = 1, \dots, n$ and $\mathbf{Y}_j \in \mathcal{F}^B, j = 1, \dots, m$. To this end, we want to find rotation \mathbf{R} and translation \mathbf{t} to minimize the energy

$$\mathcal{E} = \frac{1}{2} \sum_{i=1}^n \sum_{j=1}^m A_{ij} d(\mathbf{X}_i, \mathbf{R}\mathbf{Y}_j + \mathbf{t})^2, \quad (2.25)$$

where \mathbf{A} is a permutation matrix.

²⁰Naturally, 2D features can also be aligned with the ICP

The algorithm first updates \mathbf{A} using a closest point operator (for instance Equation (2.17)) and then estimates the transformation given these correspondences (for example with a closed-form solution of the absolute orientation problem [147]). These two steps are repeated until the update of the transformation is smaller than a pre-defined threshold.

It can be shown [11] that this algorithm always converges. Moreover, as shown by Granger and Pennec [55], if the distance measure $d(\cdot, \cdot)$ of Equation (2.25) is the Mahalanobis distance, and if the measurement error is assumed to be Gaussian, the ICP is a Maximum Likelihood estimator. In its pure form, the ICP requires a rather good initial estimate to converge to the right solution if outliers²¹ are present. Attempts have been made to increase the robustness of the ICP by discarding points through statistical analysis [163], perturbing the locations of points in one feature set by random noise [116], or estimating the probability of the correspondences and casting the ICP as an EM algorithm [55].

Mind that the ICP must not be mixed up with *naive* approaches where a cost function with unknown correspondences is optimized (compare for example [1, 88]). In the latter case, in one iteration of the optimization, the correspondency is newly determined, and a cost function (energy) is *evaluated once* with these correspondences. The ICP, however, determines the correspondency and then *optimizes* the error (energy term) based on these correspondences in a single iteration. Only after the algorithm has found a minimum, the correspondency is reestimated. The minimization of the error in each iteration assures the convergence of the ICP, whereas convergence of naive approaches is not guaranteed.

2.3.4. Optimization

Since Equation (2.12) requires a minimization of a function \mathcal{E} , numerical optimization is an important issue for medical image registration. Some registration algorithms offer a closed-form solution by design²², or a simple iterative scheme where convergence is guaranteed.

Most of the algorithms, however, make use of optimization algorithms. These algorithms solve the registration problem iteratively by refinement of parameters such that the energy term \mathcal{E} decreases and becomes minimal. Depending on the energy term, parameter-based optimization is achieved using direct methods and gradient-based methods. Besides these methods, especially non-parametric registration problems can also be solved by building up a time-dependent or fixed-point iterative scheme directly on the energy formulation (2.12), which is repeated to obtain a steady-state solution [103].

Direct Methods Direct optimization methods try to find a global minimum by sampling the parameter space. Especially for energy terms that change their number

²¹features that have no corresponding one in the other data set

²²for example a TPS registration (see appendix B)

of input measurements, these methods are used instead of gradient-based optimizers. The sampling can be done in different ways.

The by far easiest method is a *Best Neighbor* approach, where the energy is evaluated at all neighbors of a point in parameter space. The neighbor yielding the lowest energy value is the next sampling point. These steps are repeated until no further improvement of \mathcal{E} can be found at the neighbors of the sampling point, which is assumed to be the global minimum in parameter space. Of course, this method needs a good initialization value since it is prone to fall into local minima.

A better way of sampling the parameter space to find a global optimum is the *Downhill Simplex Method* [107]. In an n -dimensional parameter space, a simplex (a set of $n + 1$ points in this space) is created and certain operations can be applied to it in order to find a global optimum. Depending on the values at all $n + 1$ points, the simplex can be reflected, expanded, or contracted in order to shrink, enlarge, or move the search region. If the simplex is shrunk smaller than a threshold, the algorithm assumes to have found an optimum and returns the point of the simplex yielding the smallest energy value.

There are other direct methods, like simulated annealing, genetic optimization, Powell's Method, etc. For a good reference refer to *Numerical Recipes in C* [123]. For registration tasks, the Downhill Simplex method performs a rather good job if gradient usage is not intended.

Gradient-Based Methods Gradient-based optimization algorithms look for the optimum by analyzing the gradient, of the energy term \mathcal{E} , sometimes in combination with its second derivative. At the optimum, the gradient should be zero. Starting from an initial estimate \mathbf{p}_0 , a parameter update is computed in each iteration until the gradient vanishes (and the algorithm converges)²³.

For a function $F : \mathbb{R}^m \rightarrow \mathbb{R}$ to be optimized and a starting point $\mathbf{p}_0 \in \mathbb{R}^m$, we can give a generic gradient-based algorithm:

Algorithm 1 Gradient-Based Optimization

Given a function F and a starting point \mathbf{p}_0

```

p ← p0
repeat
  calculate parameter update  $\Delta\mathbf{p}$  from  $F$  and its derivatives
  update parameters:  $\mathbf{p} \leftarrow \mathbf{p} + \alpha\Delta\mathbf{p}$ 
until  $\|\Delta\mathbf{p}\| < \varepsilon$ 

```

The important step is the calculation of the parameter update $\Delta\mathbf{p}$. The parameter α determines how far to move in the direction determined by $\Delta\mathbf{p}$. If not too time-consuming, α is determined via a line search along $\Delta\mathbf{p}$.

A method that assures linear convergence (i.e. in each step the error reduces linearly) is the *gradient descent method*. Here, the update is determined by the negative

²³This test is usually performed via the magnitude of the update

gradient direction (direction of steepest descent):

$$\Delta \mathbf{p} = -F'. \quad (2.26)$$

A method that assures quadratic convergence (but is computationally expensive) is the *Newton method*. Here, F' is approximated with its Taylor expansion

$$F'(\mathbf{p} + \Delta \mathbf{p}) = F'(\mathbf{p}) + F''(\mathbf{p})\Delta \mathbf{p} + \mathcal{O}(\|\Delta \mathbf{p}\|^2) \quad (2.27)$$

$$\approx F'(\mathbf{p}) + F''(\mathbf{p})\Delta \mathbf{p}. \quad (2.28)$$

From this, and from the assumption that $F'(\mathbf{p}_{\min}) = 0$ at the minimum \mathbf{p}_{\min} of F , we get the update Equation by solving for $\Delta \mathbf{p}$

$$F''(\mathbf{p})\Delta \mathbf{p} = -F'(\mathbf{p}). \quad (2.29)$$

Note that the second derivative can be near to singular at some points in parameter space, which makes the Newton algorithm less robust.

Very often, energy terms are defined by a squared norm of a vector-valued function \mathbf{f} , i.e.

$$F = \frac{1}{2}\|\mathbf{f}(\mathbf{p})\|^2, \text{ where } \mathbf{f} = (f_1, \dots, f_m)^\top. \quad (2.30)$$

Here, we can also apply the gradient-descent and Newton method by computing gradient and Hessian:

$$F'(\mathbf{p}) = \mathbf{J}(\mathbf{p})^\top \mathbf{f}(\mathbf{p}), \text{ and } F''(\mathbf{p}) = \mathbf{J}(\mathbf{p})^\top \mathbf{J}(\mathbf{p}) + \sum_{i=1}^m f_i(\mathbf{p})f_i''(\mathbf{p}), \quad (2.31)$$

where \mathbf{J} is the Jacobian of function \mathbf{f} .

From Equation (2.31) we can deduce an update step approximating Newton's step, which does not require the costly computation of the second derivative. Solve for $\Delta \mathbf{p}$ in Equation

$$\mathbf{J}^\top \mathbf{J} \Delta \mathbf{p} = -\mathbf{J}^\top \mathbf{f}. \quad (2.32)$$

This method is called the *Gauss-Newton method*, which sometimes gives quadratic convergence as the Newton method.

There are also other algorithms for gradient-based optimization, for a nice overview and description see *Methods for Non-Linear Least Squares Problems* [94].

2.4. 2D-3D Registration

Now that basic methodology of medical image registration has been introduced, we can proceed to the description of 2D-3D registration concepts. After introducing the general pinhole camera derived from Computer Vision, we will focus on the particular scenario of intraoperative C-arms and explain calibration (section 2.4.2) and error analysis (section 2.4.3) in this context.

We refine the definition of section 2.3, registration of 2 images, to the particular case of 2D-3D registration:

Definition 2.6 (Projective 2D-3D Registration) Given two images $A : \Omega^3 \rightarrow \mathbb{R}$ and $B : \Omega^2 \rightarrow \mathbb{R}$, where $\Omega^3 \subset \mathbb{R}^3, \Omega^2 \subset \mathbb{R}^2$ and a set of admissible transformations $\varphi : \Omega^3 \rightarrow \Omega^2$, 2D-3D registration is the computation of a transformation φ' that aligns A to B such that a certain comparison criterion, an energy \mathcal{E} , is minimized:

$$\varphi' = \arg \min_{\varphi} \mathcal{E}. \quad (2.33)$$

2.4.1. Rigid 2D-3D Registration

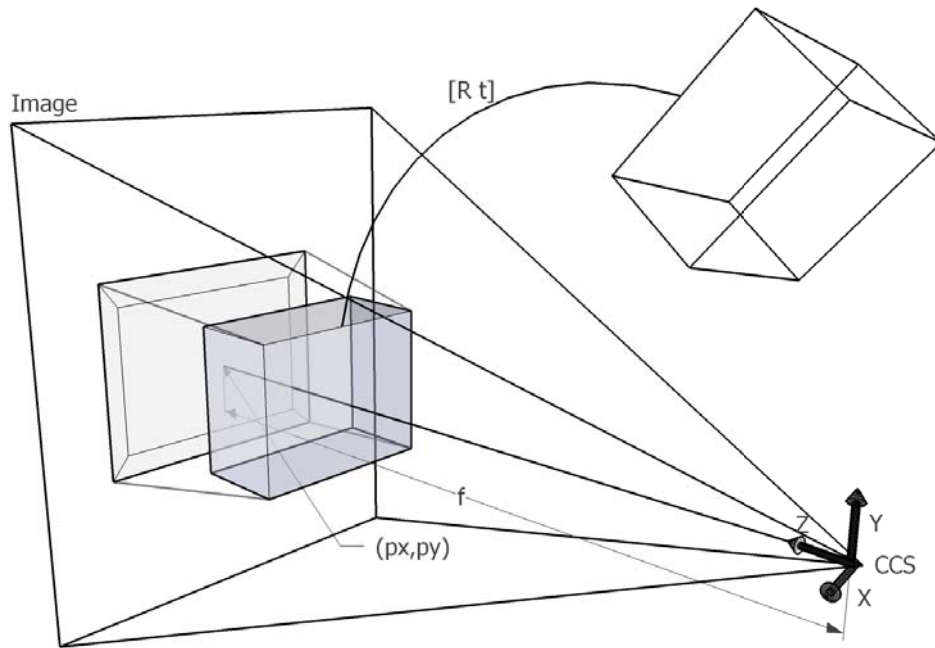


Figure 2.5.: 2D-3D setup

The transformation φ now includes a perspective projection, which is defined by a matrix $\mathbf{P} \in \mathbb{R}^{3 \times 4}$ that maps a homogeneous 3D point $\hat{\mathbf{X}} = [\mathbf{X}, 1]^T \in \mathbb{P}^3$ to a homogeneous 2D point $\hat{\mathbf{x}} \in \mathbb{P}^2$

$$\hat{\mathbf{x}} = \mathbf{P}\hat{\mathbf{X}}, \quad (2.34)$$

where $\mathbf{X} \in \mathbb{R}^3$.²⁴

Usually, the matrix \mathbf{P} is modelled by a *pinhole camera model* and can be decomposed into *intrinsic* and *extrinsic* parameters:

$$\mathbf{P} = \mathbf{K}[\mathbf{R}|\mathbf{t}]. \quad (2.35)$$

²⁴ $\mathbb{P}^2|3$ are projective spaces as defined e.g. in [66]

For an illustration of the meaning of the parameters, refer to Figure 2.5. The *calibration matrix* \mathbf{K} encapsulates the intrinsic parameters and is generally defined by

$$\mathbf{K} = \begin{bmatrix} f_x & s & p_x \\ 0 & f_y & p_y \\ 0 & 0 & 1 \end{bmatrix}. \quad (2.36)$$

Here, f_x and f_y account for the focal length in metric coordinates, i.e. $f_x = fm_x$, $f_y = fm_y$, where f is the focal length in pixel coordinates and m_x, m_y are the dimensions of a pixel in metric coordinates in x - and y -direction, respectively. The entry s denotes a skew factor accounting for non-rectangular pixels and is set to zero in most of the cases. The point $(p_x, p_y)^\top$ is the so-called *principal point* and denotes the intersection of the positive z -axis of the camera coordinate system (CCS, whose origin is located at the center of projection) with the image plane.

The matrix $[\mathbf{R}|\mathbf{t}]$ encapsulates the extrinsic parameters, which is a rigid transformation (see section 2.3.2) moving all 3D points from the *world coordinate system* (WCS)²⁵ to the CCS.

Estimating \mathbf{P} is referred to as *rigid 2D-3D registration*. Note that this estimation is a non-linear task, since a perspective division must be carried out when going from homogeneous to inhomogeneous points, which are the actual image coordinates. In fact, if the rows of \mathbf{P} are denoted by

$$\mathbf{P} = \begin{bmatrix} \mathbf{p}_1^\top \\ \mathbf{p}_2^\top \\ \mathbf{p}_3^\top \end{bmatrix} \quad (2.37)$$

the actual projective mapping function $f_{\mathbf{P}} : \mathbb{R}^3 \rightarrow \mathbb{R}^2$ is given by

$$\mathbf{x} = f_{\mathbf{P}}(\mathbf{X}) = \left(\frac{\mathbf{p}_1^\top \hat{\mathbf{X}}}{\mathbf{p}_3^\top \hat{\mathbf{X}}}, \frac{\mathbf{p}_2^\top \hat{\mathbf{X}}}{\mathbf{p}_3^\top \hat{\mathbf{X}}} \right)^\top. \quad (2.38)$$

2.4.2. Calibration

In normal camera systems the intrinsic parameters do not change and have to be determined one time only in a calibration step. For C-arms, phantoms with implanted fiducials are typically imaged to recover the projection matrices and thus the intrinsic parameters in an off-line calibration step [89]. C-arms typically provide 2-3 zoom factors with different focal lengths, all of which must be calibrated separately. The calibration reduces the rigid 2D-3D registration to the estimation of the extrinsic parameters, which is also referred to as *2D-3D Pose Estimation*.

However, care has to be taken in 2D-3D registration of X-ray images coming from a C-arm. Due to the C-arm's heavy weight, mechanical bendings of the C-structure account for changes in the intrinsic parameters as the C-arm angulation changes. This effect is increased if mobile C-arms are used. For a stationary C-arm Gorges *et al.* [54]

²⁵also called the *object coordinate system*

reported an error of the y -entry of the principal point, p_y , while p_x and f remained stable during angulation changes. Thus, the intrinsic parameter p_y depends on the chosen angle from which the X-ray is acquired, which has to be taken into account for rigid 2D-3D registration. As already mentioned in 1.2.2, state-of-the-art C-arms provide a 3D reconstruction technique to produce 3D DSAs, or CT-like slices. For that, a calibration is carried out for all angulations of the C-arm from which projections are taken for reconstruction. These positions are thoroughly calibrated [105].

The physical setup of C-arm devices introduces a *distortion* of the images due to detector geometry and earth magnetic field as described in 1.2.2. For 2D-3D registration, this distortion has to be corrected, which can be achieved by fitting a high-degree polynomial to phantom data [161]. However, newer C-arms based on flat-panel technology do not produce distorted images, discarding the necessity of distortion correction.

In summary, due to flat-panel technology and the information gained by a multiple-view calibration step for 3D reconstruction, intrinsic parameters can be assumed to be given for almost every angulation.

In the following, the term “rigid 2D-3D registration” will be interpreted as the recovery of viewpoint or pose parameters, essentially the rigid transformation $[\mathbf{R}|\mathbf{t}]$ aligning WCS to CCS. Thus, the number of parameters to solve for is 6 in the rigid case, i.e. 3 for rotation and 3 for translation. Mind that the rigid 2D-3D registration in the case of calibrated images tries to find a 3D transformation $\varphi : \Omega_{\mathcal{A}}^3 \rightarrow \Omega_{\mathcal{A}'}^3$. The actual projective mapping is part of the energy \mathcal{E} and is usually incorporated into the data term.

2.4.3. Error Analysis

Several issues have to be addressed for evaluating the quality of a registration algorithm, and for performing thorough tests to analyze the error. Usually, one has to first cope with the creation of a reference solution to which the solution provided by the proposed algorithm can be compared. Then, a reasonable error measure has to be applied to assess the quality of fit (*accuracy*) of the registration compared to the reference. This error measure should be as independent as possible from the energy used for optimization. Last but not least, the *robustness* of the algorithm has to be shown, i.e. how it behaves in special situations, how often it converges to the right solution when applied with different input, and how much disturbance can be introduced until the registration fails.

Creating Ground Truth and Gold Standard For error assessment, it is important to have a reference registration, i.e. registration parameters that are assumed to be “correct”.

For this, one can create a simulation: A previously known transformation is applied to a 3D image, which is then projected to artificially produce a 2D image. Then, this transformation has to be recovered from the registration algorithm using 3D image and produced 2D image. In this case, our reference registration is called a *ground*

truth registration, since we know the exact transformation. The problem in ground truth creation is to create an artificial projection which simulates a real 2D projection as much as possible (modeling noise, projected anatomy, etc.).

Another possibility to create a reference registration is to use a *gold standard algorithm* for the problem. For 2D-3D registration, usually reference registrations are created by implanting fiducials into the image and running a gold standard point-based registration with known correspondences. Another (less invasive) possibility is to (manually) determine corresponding landmarks (e.g. bifurcations in vessel trees in the case of angiographic registration) and again performing a point-based registration.

One of the currently favored approaches for a gold standard is to use a 3D reconstruction from the C-arm and perform a 3D-3D registration to the input 3D image to yield transformation \mathbf{T}_{3D-3D} . Due to the optimized calibration of C-arms, the projection matrices are known for all images from which the 3D reconstruction was created. Given one of these 2D views, its projection matrix $\mathbf{P} = \mathbf{K}[\mathbf{R}|\mathbf{t}]$, and the transformation \mathbf{T}_{3D-3D} , a “gold standard transformation” is given by

$$\mathbf{T}_{gold} = \begin{bmatrix} \mathbf{R} & \mathbf{t} \\ \mathbf{0} & 1 \end{bmatrix} \mathbf{T}_{3D-3D}. \quad (2.39)$$

This evaluation method only works if a 3D-3D registration algorithm is available, which allows for a calculation of a transformation. Usually, however, alignment of 2 3D images is regarded to be an easier problem than 2D-3D registration and thus, the creation of such a reference registration is accepted even in deformable regions.

The reference registration can also be produced by an expert by manually altering the transformation parameters. This is only possible in the case of rigid registration, since local changes can hardly be assessed even by clinical experts. Moreover, providing a suitable user interface to model more than 6 DOF is not a trivial task.

Accuracy Measurements Certain issues have to be addressed to define an error for single-view 2D-3D registration.

First, it is important to know that in all C-arm systems, the imaged object lies between the X-ray source and the detector system, making an error assessed in 3D smaller than the error assessed in the image plane²⁶.

Second, the transformation perpendicular to the image plane is more difficult to solve for and has to be assessed separately.

Van de Kraats *et al.* [148] have proposed a standardized protocol to assess the error in 2D-3D registration (for an illustration see Figure 2.6). They propose to use previously defined 3D image points $\{\mathbf{X}_i\}$, $i = 1, \dots, n$ (e.g. sampled throughout the volume of interest) to assess the mean *target registration error* (mTRE)

$$mTRE = \frac{1}{n} \sum_{i=1}^n d(\mathbf{T}_{reg} \hat{\mathbf{X}}_i, \mathbf{T}_{gold} \hat{\mathbf{X}}_i), \quad (2.40)$$

²⁶Mind that it is only reasonable to give the error in mm, not in pixel, which is generally no problem for all C-arm systems since they provide the size of a pixel in mm

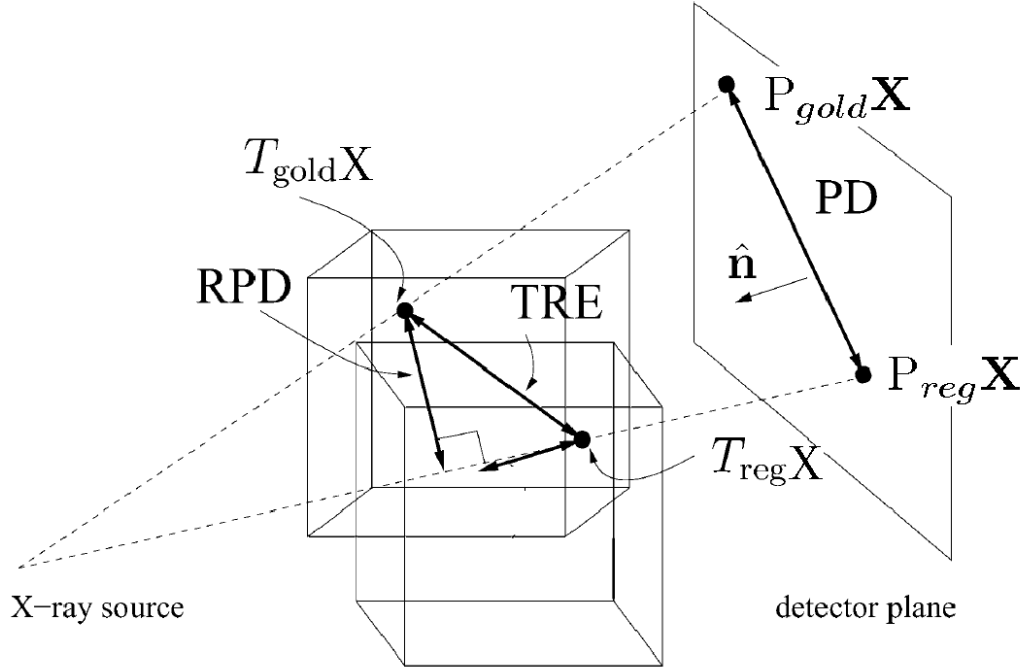


Figure 2.6.: Different Accuracy Measures. Reproduced from van de Kraats *et al.* [148]

where $d(\cdot, \cdot)$ is the Euclidean distance of the inhomogeneous representation of points, and T_{reg} is a registration computed with the algorithm to be tested.

Moreover, to assess an error without the bias in projection direction, v.d. Kraats *et al.* propose to use a mean *reprojection distance* (mRPD),

$$mRPD = \frac{1}{n} \sum_{i=1}^n d_L(L_i, T_{gold} \hat{\mathbf{X}}_i), \quad (2.41)$$

where L_i is the ray connecting $\mathbf{P}_{reg} \hat{\mathbf{X}}_i$ and the center of projection, and $d_L(\cdot, \cdot)$ is the distance of a point to a line in 3D. Evaluating the pixel error of the points \mathbf{X}_i is also suggested, called the mean *projection distance*

$$mPD = \frac{1}{n} \sum_{i=1}^n d(\mathbf{P}_{reg} \hat{\mathbf{X}}_i, \mathbf{P}_{gold} \hat{\mathbf{X}}_i). \quad (2.42)$$

Additionally to the protocol by van de Kraats *et al.*, the *root mean square error* (RMSE) in all the parameters is often evaluated, i.e. for a parameter Θ , which has been estimated m times, the mean distance to the parameter value of the gold standard registration Θ_{gold} is evaluated

$$RMSE = \sqrt{\frac{1}{m} \sum_{j=1}^m (\Theta_j - \Theta_{gold})^2} \quad (2.43)$$

Moreover, mean and standard deviation of all parameter differences are important values, especially the standard deviation, telling about the quality of the mean and thus the RMSE. Van de Kraats *et al.* reason that this error evaluation can be misleading since the translation values are dependent on the center of rotation. However, if the center of rotation coincides with the origin of the WCS, these values are not “rotation-biased” and give a good hint of the accuracy of all parameters, which, in a global transformation model, are important to interpret. For local transformations, there are usually too many parameters to reasonably interpret the RMSE and standard deviation. Thus, RMSE and standard deviation should only be assessed in rigid 2D-3D registration, which sometimes gives a better insight into the algorithm’s behavior than analysis of mTRE, mPD, or mRPD.

Robustness Assessment Robustness assessment tries to evaluate an algorithm with respect to reproducibility in different scenarios with controlled disturbances. Central to all robustness measurements is to create a set of different scenarios and test whether the algorithm can reach the right solution.

Usually, a representable amount of different instances of transformations is created and the algorithm is invoked. These are called Monte Carlo simulations. The transformations can be categorized into different ranges and the registration can be evaluated by the range until which it is still successful (the so-called *capture range*). In this context, a “successful” registration must be defined, which is a fixed threshold of the accuracy error function, usually inspired by clinical partners²⁷. The range should be defined in terms of the error with which the accuracy is measured. For instance, if the error is assessed using the mTRE, instances of the transformation must be created such that the mTRE lies within a certain range. An easier method is when the RMSE in the registration parameters is assessed, where only displacements in a certain range have to be added to all parameters.

Of course, creating different scenarios also involves testing the algorithm on different data sets. However, the amount of different patient data to be tested to yield a reliable claim on the inter-patient reproducibility is usually never achieved in the literature.

²⁷Depending on the clinical application, an algorithm has to be accurate in terms of submillimeters or several millimeters

3. State of the Art in 2D-3D Angiographic Registration

In the previous chapter, vessel extraction and registration methodology was introduced. Now, we will have a look at the state of the art of registration of angiographic 3D images to 2D projections.

A review of algorithms for *rigid* 2D-3D registration of angiographic images will be given in sections 3.1, 3.2, and 3.3 as they have been proposed in the literature.

The necessary methods like volumetric intensity projection and distance function interpretation will be provided in the respective sections.

This chapter concludes with a short summary of the few 2D-3D non-rigid registration algorithms and a discussion, where future directions of research in this field will be highlighted.

3.1. Intensity-based 2D-3D Registration

As already mentioned in 2.3.1, intensity-based registration evaluates a similarity measure directly on the intensity mapping of the images. In 2D-3D registration, however, the dimensions of the two images differ, so either the 2D projection must be backprojected into space to compare it with the 3D image intensities, or the volume has to be projected to compare it with the 2D image intensities.

The former approach is usually used if more than one view is provided, and reconstruction of intensities is feasible, compare, e.g. Tomažević *et al.* [142]. Since we are more interested in 2D-3D registration based on a single view and since there is no work addressing multi-view 2D-3D registration on *angiographic* images via reconstruction, we will ban approaches based on backprojection from the discussion.

The latter approach, projecting the volume and evaluating a similarity measure in 2D, will be discussed in the following. The projection of the volume's intensities has to be carried out such that the physical process of X-ray imaging is simulated. This simulated or reconstructed 2D image from 3D intensities is called a *Digitally Reconstructed Radiograph*, DRR. DRR generation can be particularly achieved when using CT images to align them with 2D X-ray images since their acquisition follows the same laws of attenuation of radio densities. However, as we will see below, also MR data can be used to produce DRRs for angiographic registration if adequately segmented.

The process of 2D-3D intensity-based registration can then be summarized as an optimization (see 2.3.4) of parameters Θ over an energy term. The energy evaluation reads as defined in algorithm 2.

Algorithm 2 Energy Evaluation of Image-Based 2D-3D Registration

Given a 3D image \mathcal{A} and a 2D image \mathcal{B} , and parameters Θ
 create a DRR from \mathcal{A} using the projection matrix \mathbf{P}_Θ to produce \mathcal{A}_{DRR}
 evaluate a similarity measure $SM(\mathcal{A}_{DRR}, \mathcal{B})$

Below, we will have a closer look at DRR generation for angiographic images, and in section 3.1.2 we detail algorithms for 2D-3D rigid intensity-based registration as they have been proposed in the literature.

3.1.1. DRR Generation

X-ray Imaging The ionizing property of X-ray beams is used by CT(A) and intra-operative devices such as C-arms to acquire images. Images can be produced by radiation since different materials *interact* with the emitted energy of an X-ray beam¹ in a different way, according to the material's radio density. If a material interacts with the energy, part of the energy is lost during traversal. This "loss of energy" is called *attenuation* and can be physically described by the Lambert-Beer law for attenuation of radiation through a medium: Given an initial energy E_0 of an X-ray source, the remaining energy E of a ray traversing an object is given by

$$E = E_0 e^{-\int \mu(\mathbf{x}) d\mathbf{x}}, \quad (3.1)$$

where $\mu(\mathbf{x})$ is the attenuation coefficient of the object at point \mathbf{x} .

CT Hounsfield units CT intensities are measured in Hounsfield units, i.e. intensity values normalized by the attenuation of water:

$$H = \frac{\mu - \mu_W}{\mu_W} 1000, \quad (3.2)$$

where μ is the attenuation coefficient of a certain material, and μ_W that of water. Putting this equation into Equation (3.1), we get [117]

$$E_{DRR} = E_0 e^{-\int \left(\frac{H(\mathbf{x})\mu_W}{1000} + \mu_W \right) d\mathbf{x}}. \quad (3.3)$$

This formulation can be used to create DRRs from CT images.

Image Formation Using Equation (3.3)² and a projection matrix \mathbf{P} , an image can be created by casting rays from the center of projection through every pixel of the image plane and following the ray through the volume (see Figure 3.1). If a voxel is hit

¹The energy of an X-ray beam must not be mixed up with the energy used for minimization. This will be indicated by using different notations.

²To reduce the computational cost, usually its logarithm is used

during traversal, its Hounsfield value is contributing to the integral³. Since usual X-ray images are of size 512×512 or 1024×1024 pixels, this image formation process is computationally expensive. However, speed-ups can be achieved by approximating ray casting through blending of a 3D texture mapped volume, or by shifting ray casting to the Graphics Processing Unit (GPU) [75]. Other techniques adapted from the Computer Graphics community have been proposed for fast DRR generation [129, 12].

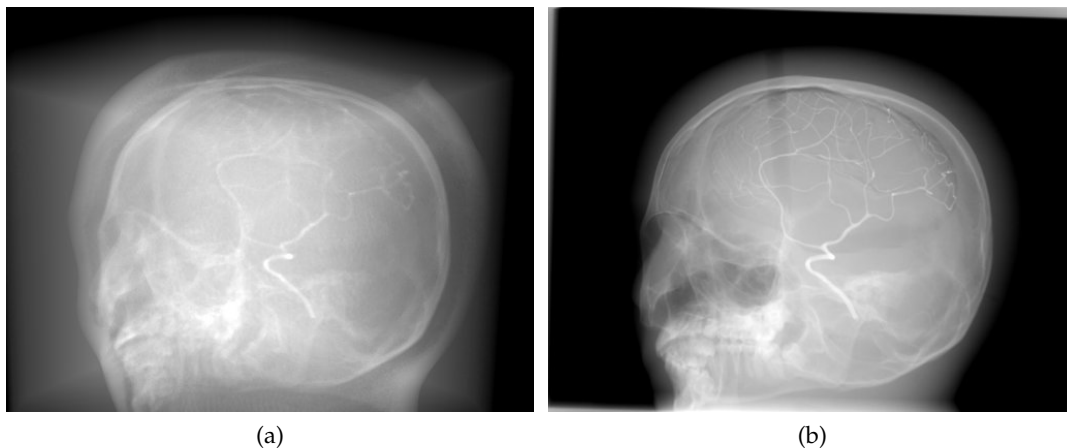


Figure 3.1.: (a) A DRR generated from a CTA volume, (b) a real fluoroscopic image (inverted).

Radiometric Calibration For DRR generation, the energy E_{DRR} has to be further processed to simulate the traversal of electrons through the intensifier, or the flat panel detector imaging process. Only after this processing, the intensity \mathcal{I}_{DRR} can be assigned to pixels. Different models have been suggested for simulation, but none can be favored since they are not modeling the physical process of image formation. Moreover, CT machines have a different effective energy with which images are acquired compared to intraoperative devices. Thus, different *transfer functions*⁴ are applied to the volume intensities in order to simulate different effective energy levels of CT image acquisition and intensifier/flat panel physics. An estimation procedure of the transfer function's parameters, a *radiometric calibration*, can be carried out to make the DRR most similar to a real radiograph as proposed by Khamene *et al.* [75].

DRR Generation for Angiographic Data For contrasted vessels, a logarithmic relationship can also be established between the remaining energy E_{DRR} and the resulting intensity, i.e. $\mathcal{I}_{DRR} = \log[E_{DRR}]$ [117, 81]. Thus, the intensity \mathcal{I}_{DRR} can be

³which is approximated by a sum in the discrete setting

⁴A transfer function is a mapping of intensity values to a color map

assumed to be proportional to the length L of the path traversed through the 3D vessel and the contrast material's density ξ [68]

$$\mathcal{I}_{DRR} \propto \mu \int_L \xi(\mathbf{x}) d\mathbf{x}, \quad (3.4)$$

where μ is the attenuation coefficient of the contrast material.

Mind that this equation only holds inside a contrasted vessel, surrounding tissue cannot be modeled thus. That is, in order to produce DRRs for angiographic data, a vascular segmentation is usually necessary as a pre-processing step. However, since the density of contrast material can also be measured in MRA voxel intensities, and since μ can be estimated by radiometric calibration, MRA images can be used for DRR generation as well as CTA images.⁵ Most methods for intensity-based 2D-3D registration of MRA data approximate this DRR generation with a Maximum Intensity Projection (MIP), where only the voxel on the ray with the highest intensity contributes to the pixel intensity. On the one hand, this method is prone to error caused by noise compared to a full integration over all vessel voxels on the ray. On the other hand, however, no segmentation of the 3D vasculature is needed to produce DRRs.

3.1.2. Registration Algorithms

In the following, intensity-based 2D-3D rigid registration algorithms will be reviewed. All methods will be described by the input data their algorithms work on, the DRR generator which is used, the similarity measure defining the energy term, and the optimization technique to reach a global optimum. Execution times and accuracy are hard to compare due to different hardware, non-standardized evaluation protocols, and different input data. However, they are reported to give an impression on runtime and performance, the reader is referred to the original publications for a thorough explanation on experiments.

An extensive study of different similarity measures for 2D-3D registration of CT to (non-contrasted) X-ray images can be found in Penney *et al.* [118]. The definition of all measures described below can be found in this publication and mathematical details will be left out thus.

Hipwell, McLaughlin, and Byrne Hipwell *et al.* [68] builds on the study of Penney *et al.* [118] to register cerebral angiograms (DSAs) to brain Phase Contrast MRA data. Input data are DSAs and different segmentations of the cerebral vasculature visible in the MRA image. DRRs were generated by raycasting using Equation (3.4). Hipwell *et al.* found out that gradient-based (gradient difference (GD), gradient correlation (GC)) and pattern intensity (PI) similarity measures perform best for the registration of angiographic data.

⁵In fact, this is just an approximative assumption since MRA vessel intensities can change due to e.g. flow property and are not as uniform as in CTA data. Establishing a real physical relationship of MRA vessel intensities and contrasted X-ray intensities is not a trivial task.

Gradient-based similarity measures compare the gradient images of the input data $\nabla\mathcal{A}_{DRR}$ and $\nabla\mathcal{B}$ and the registration is thus driven by aligning vessel contours. Pattern Intensity compares patches in the intensity difference images in an asymptotic function. Hipwell *et al.* used a Best Neighbor algorithm for optimization, execution time of the algorithm was ca. 5min on a 1.2-GHz AMD CPU.

McLaughlin *et al.* [100, 101] compared the algorithm proposed by Hipwell *et al.* with the ICP algorithm adapted to 2D-3D registration of angiograms as proposed by Kita *et al.* [77] (see 3.2.3). Only the gradient difference similarity measure was used in this study. While the intensity-based approach proved to be more accurate, the ICP approach was more robust in the cases where only few dominant vessel structures were visible. A drawback of Hipwell's method is execution time. While the ICP approach by Kita *et al.* took 20 sec, the gradient-difference approach took more than 14 min in average.

Byrne *et al.* [23] used Hipwell's registration technique to align 3D rotational angiography images (3D DSAs, acquired by subtracting a native 3D reconstruction from a contrasted 3D reconstruction) images to 2D DSAs for neuro interventions. The registration is performed on images with downsampled resolution, gaining a speed-up to ca. 33 sec (measured on a 1.7 GHz Intel CPU) with similar accuracy compared to a registration on original images. Since the data sets came from the same imaging device, accuracy (measured with the reprojection distance (RPD), see 2.4.3) could be improved from 1.6 mm reported by Hipwell *et al.* to 1.3 mm.

Kerrien Kerrien *et al.* [73] register 3D DSAs to 2D DSAs for neuroradiological interventions.

They propose a method where a first estimate of the rigid transformation parameters is computed by a calibration of the C-arm, providing a good estimate of calibration matrix \mathbf{K} , distortion coefficients, and the rotation angles, but a bad estimate of translation parameters \mathbf{t} [74].

Then, they refine the in-plane translation (t_x and t_y) by using a normalized cross correlation (NCC) similarity measure, which measures the correlation of each pixel pair and thus the degree of linear relationship of the intensities. As DRR, they use a Maximum Intensity Projection (MIP) created from the 3D DSA.

After the registration based on NCC, the assumption to be in the vicinity of the true pose allows for a modified optical flow technique to optimize for rotation and translation parameters. By using the depth information of the MIP points (only the voxel with highest intensity is used for projection and is thus unique) and the image constancy assumption [69], the 6 rigid transformation parameters can be estimated and optimized.

The optimization technique chosen for NCC optimization is an exhaustive search of translation parameters perpendicular to the image plane (i.e. x - and y -translation). The optical flow optimization is done by matrix inversion to solve for a least-squares solution.

A manual assessment of the error showed an accuracy of 1.5mm of the registration algorithm, execution time was within 90 sec on a Sun UltraSparc workstation.

A drawback of this method is its restriction to the registration of 3D images that have been acquired by the same machine as the 2D X-ray images.

Dey and Napel Dey and Napel [39] present a method based on DRR generation of subvolumes and Monte Carlo optimization. They test their algorithm on 3D DSAs of a pig brain to be registered to the fluoroscopy images the 3D image was reconstructed from. The focus of the work is the test of two different similarity measures, Pattern Intensity (PI) and Mutual Information (MI) as well as two different optimization techniques, Powell's method and a strategy based on Monte Carlo sampling. Moreover, a truncation of the volume to a subvolume was justified to produce, with proper normalization, a similar DRR as if the entire volume is used.

The Monte Carlo optimization randomly follows a direction in parameter space, if the energy decreases, this direction is taken, if it increases, an acceptance probability is evaluated by an annealing scheme and the direction is again taken, if this probability is above a randomly chosen threshold. This optimization is carried out on a downsampled level, whereas its result is used for an initial estimate of a Powell optimization on the fine level.

Since Monte Carlo optimization is rather slow, this method takes ca. 4-7 min on a Pentium M 1.7 GHz. Accuracy was evaluated on the reference registration given by the machine calibration through a subvolume target registration error (see 2.4.3), and was at 2.37 mm. Accuracy and registration success using PI was slightly better compared to MI experiments.

	Input	DRR	SM	Opt.	Time	Accuracy
Hipwell '03 [68]	PC MRA & 2D DSA	raycast	GD,GC PI	Best Neighbor	5 min	1.6mm
Byrne '04 [23]	3D DSA & 2D DSA	raycast	GD	Best Neighbor	33 sec	1.3mm
Kerrien '99 [73]	3D DSA & 2D DSA	MIP	NCC & opt. flow	exhaustive & mat. inversion	90 sec	1.5mm
Dey '06 [39]	3D DSA & 2D Angio	norm. raycast	PI, MI	Monte Carlo & Powell	4-7 min	2.4mm

Table 3.1.: Summary of intensity-based 2D-3D rigid registration algorithms

Table 3.1 summarizes the gist of all presented intensity-based algorithms.

3.2. Feature-based 2D-3D Registration

For this class of rigid registration algorithms, features are extracted in order to align the images. In angiographic registration, vessels and their attributes are exclusively used as features for 2D-3D registration since they are the dominant structure in the images and usually represent the region of interest (e.g. for catheter navigation).

Feature-based methods are said to be more robust since data terms evaluating a geometric distance do not get trapped as easily in local minima as similarity-based

data terms. However, they usually are less accurate, which is due to a propagation of the error introduced during preprocessing (segmentation) compared to intensity-based algorithms (see Figure 3.2).

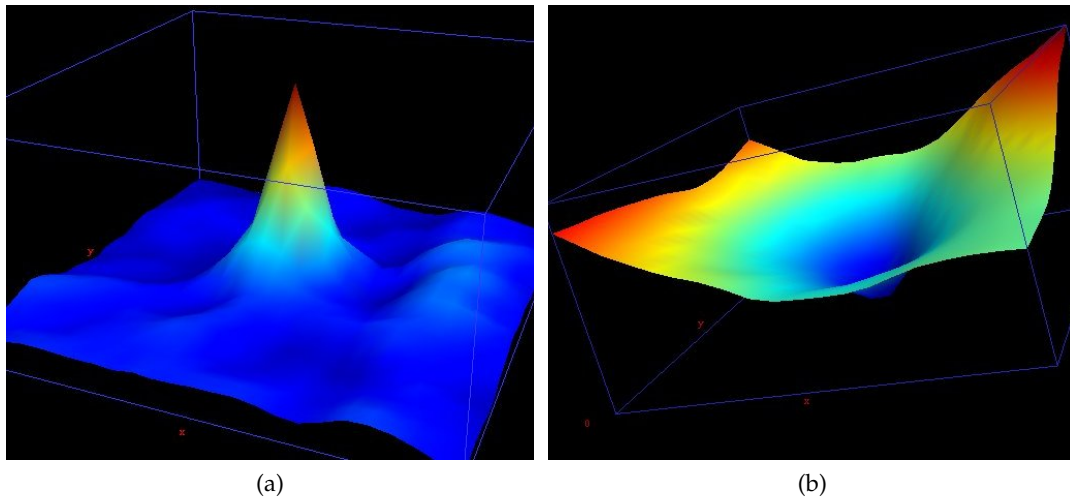


Figure 3.2.: A plot of a data term of (a) an intensity-based registration (SM: Gradient Correlation), and (b) a feature-based registration (on vessel centerlines). Two parameters (x and y translation) are plotted against the data term values. (a) has a sharp global optimum, but some local optima, (b) has less local optima, but not a very sharp global optimum. Thus, intensity-based algorithms are more accurate, but have a smaller capture range, while feature-based approaches have a higher capture range, but are usually less accurate.

Vessel extraction and quantification techniques have already been detailed in 2.2. Once vessel features have been found, the issues that have to be addressed for a successful 2D-3D registration are the search for correspondences, a formulation of a distance-based energy function, and the optimization strategy used to reach an optimum.

Basically, there are two approaches that have been followed by researchers. Either an energy formulation based on distances of (sampled) and corresponding curves (vessel centerlines) is established and optimized (see section 3.2.2), or the ICP algorithm is adapted to 2D-3D curve registration (section 3.2.3).

3.2.1. Distance Functions

Establishing a distance function between features is necessary for feature-based 2D-3D registration algorithms. In general, the error can be evaluated in 2D by projecting 3D features and computing a *pixel error*, or it can be evaluated in 3D by backprojecting 2D features and computing a closest point on the backprojection rays and the corresponding 3D features (*object error*). In C-arm systems, the imaged object is

located between X-ray source and detector plane, i.e. the object error will usually be smaller than the pixel error. Other than the magnitude, there is no difference between the two errors.

Pixel Error Given a calibration matrix \mathbf{K} , and corresponding points $\{\mathbf{X}_i \leftrightarrow \mathbf{x}_i\}$, we want to find a transformation $\mathbf{T} = [\mathbf{R}|\mathbf{t}]$, such that an energy in 2D (pixel error)

$$\mathcal{E} = \sum_{i=1}^n d(f_{\mathbf{KT}}(\mathbf{X}_i) - \mathbf{x}_i)^2 \quad (3.5)$$

is minimized. $f_{\mathbf{KT}}$ is the projection function as defined in Equation (2.38), $d(., .)$ is the Euclidean or Mahalanobis distance (Equations (2.15) and (2.16)).

In fact, the underlying model for minimizing this energy is based on the assumption that measurement noise occurs in the 2D points only, and that 3D points are exact. Pixel error minimization using the Mahalanobis distance is a Maximum Likelihood estimator of 2D-3D registration if measurement error occurs in 2D features only.

Reprojection Error A more general model, which also accounts for measurement errors in 3D points minimizes the energy (reprojection error)

$$\mathcal{E} = \sum_{i=1}^n d(f_{\mathbf{KT}}(\tilde{\mathbf{X}}_i) - \mathbf{x}_i)^2 + d(\tilde{\mathbf{X}}_i - \mathbf{X}_i)^2, \quad (3.6)$$

where not only the parameters of \mathbf{T} , but also the entries of the estimated points $\tilde{\mathbf{X}}$ are included in the set of parameters and subject to optimization [108]. Mind that $\tilde{\mathbf{X}}$ only has to be computed once via backprojection, then its entries are used as parameters in the optimization process.

Once correspondency has been found between vessel features, the reprojection error can also be minimized instead of the pixel error. Reprojection error minimization using the Mahalanobis distance is a Maximum Likelihood estimator of 2D-3D registration if measurement error occurs in 2D and 3D features.

3.2.2. Optimizer-based Algorithms

We will now discuss particular feature-based algorithms as they have been proposed in the literature. Regarding these algorithms, we will highlight the input data, the distance function, how to establish correspondency, the chosen optimization method and, as in the intensity-based case, time and accuracy of the methods.

Alperin Alperin *et al.* [1] were the first to address the problem of 2D-3D angiographic registration. They propose a retrospective technique, where previously extracted vessel segments of brain MRA and contrasted X-ray data are aligned by centerline point distance minimization. The vessel centerline extraction is performed

by manual determination of segment endings and a vessel tracking algorithm connecting the two. Correspondences are found by intersection of lines perpendicular to the X-ray vessel segment direction at each centerline point with the projected MRA segment. The averaged distance of all centerline point pairs is taken as energy term to be minimized. Outliers are taken care of by evaluating the fraction of non-intersecting lines to intersecting lines and adding a weighting factor if this fraction becomes larger. For this correspondence search, the vessel segment must be pre-aligned, which is achieved manually. Brent's optimizer for multiple dimensions is used to reach a minimum of the energy.

Accuracy was 0.6mm using 4 vessel segments for registration evaluated with the cost function of the algorithm⁶, where the runtime (on a IBM RISC 6000/730) was 1min per segment.

Liu and Bullitt Liu *et al.* [88] and Bullitt *et al.* [21] register centerline curves of 2D DSA of the brain to 3D vasculature extracted from MRA images. The 2D segmentation is driven by cores as proposed by Pizer *et al.* [121], the 3D vessels are extracted using Aylward's algorithm [6] (for both methods see 2.2.5).

Liu *et al.* first describe the "near-projective invariance" of centerline curves and thus justify why these curves may be used to achieve a registration of the underlying vasculature. Projective invariance means in this context that the centerline of a 2D vessel projection equals a projected centerline extracted from a corresponding vessel of a 3D volume. Near-projective invariance means that this invariance is not guaranteed everywhere on the vessel tree: At overlays the curve extracted in 2D differs from the projected 3D curve.

A distance function, which is similar to that proposed by Alperin *et al.* (apart from the weighting factor) is optimized once corresponding centerline curve segments have been manually assigned. In Liu's algorithm, the correspondence search is carried out only once. Afterwards, correspondency is assumed to be given for point pairs, and a gradient-based optimization method (Newton) is utilized to minimize the error in 2D.

Execution time of the algorithm was ca. 2-5min on a HP 712/80 workstation. The accuracy of this method depends on the number of corresponding vessel segments chosen to be aligned. For clinical data it was assessed visually.

3.2.3. ICP-based Algorithms

Introducing a perspective projection $f_{\mathbf{P}}$ into Equation (2.25), we can adapt the ICP algorithm to 2D-3D registration:

$$\mathcal{E} = \frac{1}{2} \sum_{i=1}^n \sum_{j=1}^m A_{ij} d(\mathbf{x}_i, f_{\mathbf{P}}(\mathbf{X}_j))^2, \quad (3.7)$$

⁶which is generally a bad idea, since it makes evaluation results biased to the cost function. For a discussion on error analysis see 2.4.3

where \mathbf{A} is a permutation matrix. The reprojection error can be incorporated likewise but has not been addressed in 2D-3D feature-based registration.

The task now is to establish correspondences, i.e. update the permutation matrix \mathbf{A} in the first step of the algorithm. Then, a distance can be minimized via a 2D-3D pose estimator.

Feldmar Feldmar *et al.* [41] register 3D DSA data to 2D DSAs of brain vasculature.

They first define corresponding point triplets by attributing centerline points (extracted using Malandain's algorithm [96]) with properties that are invariant under perspective projection. They state two bitangent line properties, which must be satisfied if triplets of points $\{\mathbf{X}_1, \mathbf{X}_2, \mathbf{X}_3\}$ and $\{\mathbf{x}_1, \mathbf{x}_2, \mathbf{x}_3\}$ correspond.

Then, they iteratively choose potentially corresponding triplets and run a 2D-3D pose estimation using a P3P⁷ estimation technique [65].

Once a satisfactory transformation has been found, the algorithm repeats these two steps until a convergence criteria is reached. This technique is guaranteed to yield the least-squares solution to Equation 3.7 with given \mathbf{A} .

For further improvement, Feldmar *et al.* use an Extended Kalman filter to calculate the covariance matrix of the estimated parameters in $[\mathbf{R}|\mathbf{t}]$ and propagate it to get the covariance matrix for every point correspondence $\mathbf{R}\mathbf{X} + \mathbf{t} \leftrightarrow \mathbf{x}$. Using the Mahalanobis distance, the impact of point correspondences that are very unlikely is reduced in the estimation process.

A further improvement of the algorithm is the use of tangent information in the distance metric $d(., .)$. By defining a distance on 4D points $(x, y, \tan_x, \tan_y)^\top$, closest points can be assigned easier. However, tangent information is not rotationally invariant, i.e. a good initial estimate of \mathbf{R} must be provided for the 4D points to be accurately matched. Mind that the estimation of the motion (the P3P) must also use the 4D distance, which can be computed with the Extended Kalman Filter.

Their clinical experiments showed an improvement of the mean pixel error to 0.83 pix of the matched points⁸, which was achieved in 20 sec on a DEC workstation.

Kita Kita *et al.* [77] register a 3D vessel model extracted from MRA using the algorithm of Wilson and Noble (see 2.2.4) to 2D DSA data of cerebral vessels. An initialization step finds rotation using C-arm device information and translation using template matching of a projected vessel curve and the intensities of the DSA (the vessel curves are translated such that the summed intensity of the DSA at the projected sampling point locations is as small as possible).

Then, an automatic thresholding is carried out to retrieve parts of the centerline of the DSA. The thresholding is driven by the location of the projected 3D centerline.

The core of the algorithm provides a territory-based correspondence search. At each point of the projected centerline a region growing is started simultaneously

⁷P3P means Perspective 3-Point Problem and stands for the computation of the pose $\mathbf{R}|\mathbf{t}$ from a triplet of corresponding 2D and 3D points $\{\mathbf{X}_1, \mathbf{X}_2, \mathbf{X}_3\} \leftrightarrow \{\mathbf{x}_1, \mathbf{x}_2, \mathbf{x}_3\}$

⁸Evaluating an error on the points with which the algorithm estimated the transformation is biased in terms of spatial locations. Preferably, the error assessment is done on points not used for the registration, see 2.4.3

and stopped if another region has advanced there already. In these regions only, the correspondence search with a closest point operator is carried out. This reduces the probability that points projected on overlap or very near to each other establish wrong correspondences and drive the registration to a wrong solution.

The pose estimation is carried out by separating rotation and translation estimation and linearizing the rotation matrix using approximative unit quaternion representation. The correspondence search and pose estimation steps are iterated until convergence (the chosen threshold is not explicitly stated in the original publication). Thus, the pixel error based on the Euclidean distance is minimized in an ICP manner.

On a SUN IPX/ULTRA1 workstation, the algorithm took 5-6 sec, accuracy was assessed manually.

Table 3.2 summarizes all issues of feature-based approaches for 2D-3D rigid registration.

	Input	Distance Function	Corr.	Opt.	Time	Accuracy
Alperin '94 [1]	MRA & 2D DSA	2D Euclidean	perpendicular intersections	Brent	1 min per segment	0.6 mm
Liu '98 [88]	MRA & 2D DSA	2D Euclidean	perpendicular intersections	Newton	2-5 min	—
Feldmar '95 [41]	3D DSA & 2D DSA	2D/4D Mahalanobis	bitangent properties	ICP	20 sec	0.83 pix
Kita '98 [77]	MRA & 2D DSA	2D Euclidean	region based	ICP	5-6 sec	—

Table 3.2.: Summary of feature-based 2D-3D rigid registration algorithms

3.3. Hybrid 2D-3D Registration

There are a number of methods that make use of both approaches, i.e. mix feature-based and intensity-based techniques. Whenever there is a mixture of intensities and spatial locations, or distance and similarity, we call a method hybrid. In the following, they will be shortly presented.

Chan Chan *et al.* [27] register vessel models of Phase Contrast MRA data to DSA images of the brain. The 3D model is generated by thresholding and skeletonization. Radii are associated to all centerline points by a distance map of the segmentation. In each step of the iterative algorithm, they project all centerline points of the MRA vasculature together with a sphere with the same radius as the vessel at this centerline point and assign the highest intensity value to all points inside the projected sphere. All other pixels get the lowest intensity value to create a binary image. They optimize the sum-of-squared-difference (SSD) similarity measure between the projected centerline image and an inverted DSA. For optimization they use Powell's direction set method.

The achieved root mean square error of the method lies within 1.7mm measured by manually selected landmarks. Execution time is 20-40 sec.

The creation of a binary image from centerline pixels and spheres approximates a DRR. However, the technique is using quantitative information (centerline points, vessel diameter) for creating a 2D projection. Thus, the accuracy of the method is more dependent on the segmentation and centerline extraction similar to feature-based approaches.

Vermandel Vermandel *et al.* [150] register brain MRA volumes to 2D DSA images. In a first step, a 3D and 2D segment of the vasculature is extracted via region growing (see section 2.2.4). The segments must contain the same vessel structures. To evaluate the energy, a binary image is generated by projecting the 3D segmentation onto the image plane, and the sum of squared differences (SSD) is evaluated between two binary images. The 6 parameters are optimized using a hybrid simulated annealing (HSA) scheme [130]. An accuracy between 1-2mm, which is comparable to intensity-based approaches could be achieved, unfortunately, the runtime is not reported. The accuracy was evaluated with the RPD error, see 2.4.3.

Turgeon Turgeon *et al.* [145] register ECG-gated 2D heart angiograms to 3D preoperative angiographic data and is thus one of the few works addressing 2D-3D rigid registration in a deformable region. The 3D data set is first thresholded to yield a segmentation from which a triangulated mesh is produced using the Marching Cubes algorithm [90]. The 2D segmentation is computed using Koller's algorithm (see 2.2.5). In a simulated clinical environment, the 3D mesh is projected to form a binary image, which is compared to the 2D segmented vasculature using a mixture of correlation and entropy similarity measure (Entropy Correlation Coefficient, ECC). A Downhill-Simplex strategy is used to optimize for the rigid registration parameters.

An extensive study is provided including single- and dual-view registration in the same and different heart phases on simulated and clinical images. A 3D error was assessed by measuring the average distance of corresponding vessel centerline points of reference registration and computed registration. For single-view registration, average execution time was 32 sec and an error of 1.6mm could be achieved in the same heart phase. In a different phase with present deformation, however, the algorithm exceeded the threshold for a successful registration, which was set to 5mm.

Jomier One last but interesting approach is the model-to-image registration proposed by Jomier *et al.* [70] for navigation in TIPS surgery. As Turgeon's work, this method is employed in a deformable region, but without gating information. For registering a 3D MRA image to two 2D DSAs a 3D model of the vasculature is first extracted using Aylward's technique [6]. The projection of the model is directly com-

pared to the 2D DSA image intensities via the energy term

$$\mathcal{E} = \frac{1}{\sum_{i=1}^N r_i} \sum_{i=1}^N r_i \mathcal{I}_{\sigma=r_i}(\varphi(\mathbf{X}_i)), \quad (3.8)$$

where N is the number of extracted 3D centerline points \mathbf{X}_i , and r_i are their associated *projected* radii. $\mathcal{I}_{\sigma=r_i}$ is the 2D DSA smoothed by a Gaussian kernel with standard deviation σ .

Since vessels are dark objects in DSA images, this metric is subject to minimization. The Gaussian blurring with radius r_i assures that vessels with a smaller radius than r_i get a higher response. Moreover, by multiplying the response with r_i , the alignment is driven by vessels with larger diameter.

For optimization Jomier *et al.* chose a sequential technique optimizing for one parameter at a time comparable to Powell's direction set method. Accuracy and robustness was assessed via Monte Carlo studies yielding mean and standard deviation of the distances of all 6 parameters to reference parameters. The reported accuracy (compared against a reference registration computed by Liu's algorithm [88]) lay between $0.9 \pm 1.2mm$ for translations and $0.9 \pm 1.9^\circ$ for rotations; the runtime of the algorithm is less than 20 sec on a 2.2GHz Pentium 4 CPU.

Table 3.3 addresses the main issues of all hybrid approaches. Additional to optimization technique, accuracy, runtime, and input data, distance function or similarity measure used, and the integration of original intensities into the registration process are listed.

	Input	(Dis-)Similarity	Orig. Int.	Opt.	Time	Accuracy
Chan '04 [27]	PC MRA & 2D DSA	SSD	No	Powell-Brent	20-40 sec	1.7 mm
Vermandel '03 [150]	MRA & 2D DSA	SSD	No	HSA	—	1-2 mm
Turgeon '05 [145]	3D DSA & 2D DSA	ECC	Yes	Downhill Simplex	32 sec	1.6 mm
Jomier '06 [70]	MRA & 2 2D DSA	intensity at centerline point	Yes	1D param search	<20 sec	$\mathbf{t} : < 2.1mm$ $\mathbf{R} : < 2.8^\circ$

Table 3.3.: Summary of hybrid 2D-3D rigid registration algorithms

3.4. Deformable 2D-3D Registration

There is not much work on deformable 2D-3D registration, especially using only one view. This is due to the inherent two-folded ill-posedness of the problem:

- First, the set of admissible transformations must be constrained to yield "reasonable" deformations, which can be achieved by constructing a diffeomorphism or by imposing smoothness constraints (see section 2.3.2).

- Second, the displacement in ray direction, i.e. in z-direction of the CCS cannot be assessed from one view. Thus, the problem of single-view 2D-3D deformable registration has an infinite number of solutions.

Some work can be found on non-rigid registration of a statistical model created from CT images to *two or more* views of non-contrasted X-ray images [45, 9, 160]. Having two views and the relative transformation between them, the displacement in ray direction can be resolved and the ill-posedness of the problem is reduced to one issue only. The work by Yao and Taylor [160] also assess the registration accuracy when only one view is available, but the result is not convincing (A volume overlap of ground truth and deformed structure of only 64 % could be achieved).

Penney [117] extended his algorithm for 2D-3D rigid registration by deformations, where rigid structures are incorporated. His intraoperative X-ray image showed several vertebrae of the spine, each of them undergoing a different rigid transformation. His goal was to transform the volume to incorporate all rigid transformations and interpolate in between them. First, the single vertebrae were registered separately to their projections to yield rigid transformations \mathbf{T}_i . Then, control points were set in the centroids of the vertebrae. These control points were used for computing a Thin Plate Spline (see Appendix B), where the affine part was replaced by a combination of the matrices \mathbf{T}_i . This algorithm worked well for registration of more than one rigid structure, but is likely to fail when the structure itself is deforming.

Up to this moment, no work could be found on *angiographic* 2D-3D deformable registration in the literature. We will see in chapter 6, however, that a deformable registration is possible on these data sets even if only one view is available.

3.5. Discussion

In the last sections we have reviewed all relevant contributions to the field of 2D-3D registration with respect to angiographic images. We have listed intensity-based, feature-based and hybrid approaches for *rigid* 2D-3D registration. Moreover, we have shortly summarized all methods found on 2D-3D non-rigid registration, all of them operating in a multiple-view scenario, or vastly lacking accuracy.

In this section, the issue of initialization will be discussed, since it is crucial for the applicability of the previously presented methods in clinical treatments. To finish this review, possible directions of future research in angiographic 2D-3D registration will be given.

3.5.1. Initialization

Initialization is an important issue for the applicability of registration algorithms in clinical treatment. During C-arm procedures, time is a crucial factor, and a manual pre-alignment of the 3D image to the currently acquired 2D projection is not desirable.

All algorithms that align 3D DSA to a 2D DSA acquired on the same machine have an inherent initial registration estimate due to calibration. As the C-arm has to be calibrated for 3D DSA reconstruction, the projection matrices of all views involved in the reconstruction are known. If the 2D DSA is acquired from a view not contributing to the reconstruction, an interpolation can yield a good initial alignment. However, if the DSA is not acquired in the vicinity of a calibrated viewpoint, these algorithms need to be initialized manually. Since typical reconstruction views are only those with a secondary (lateral) angle close to zero, changing this angle leads to a loss of initial alignment in these methods.

The approach by Feldmar *et al.* [41] has the advantage that the pose estimation can be carried out from any viewpoint. However, finding reliable correspondences especially when using the 4D points involving tangency need a good initial estimate since tangency is not projectively invariant. Without the extension to 4D points, however, the bitangent properties and the pose estimator can yield a good pose from any initial one.

Kita *et al.* [77] explicitly summarizes an initialization step. While a rough first estimate of the rotation parameters for \mathbf{R} and t_z come from a calibration step, the in-plane translation (t_x, t_y) is found via template matching. The initialization step is thus fully automatic.

All the other methods need a manual pre-alignment before the registration algorithm can be invoked.

3.5.2. Directions of Future Research

The problem of 2D-3D registration of angiographic images in rigid areas, such as brain vasculature, can be said to be solved. As described above, algorithms have been proposed that perform reasonably fast, and have been tested for accuracy and robustness thoroughly. A rigid registration in abdominal or thoracic areas, where deformation occurs, has not been studied extensively and will be most probably subject to research in the upcoming years. The behavior of algorithms to non-rigid movement has to be analyzed in terms of accuracy and robustness.

In the last few years, advancements in 3D cone beam reconstruction made it possible to acquire not only 3D DSA but 3D images with CT-like quality intraoperatively. Since these images are acquired on the same machine, they are registered to the views they are reconstructed from by calibration. Due to the time pressure during a treatment physicians will still plan procedures before the operation on preoperatively acquired scans. Region of interest, catheter paths, and complication assessment can be planned then. In this scenario, a 3D-3D registration of preoperative data to an intraoperative reconstruction can make a 2D-3D registration easier.

2D overview DSAs as well as 2D contrasted fluoroscopy sequences will still be acquired during catheter injection and advancement. Usually, the 2D DSA is not acquired from the exact same location as a view used for reconstruction. Moreover, and more importantly, abdominal imaging always involves deformation due to breathing or patient movement. Both externally induced motions can cause misalignments of 3D image and 2D DSA/Fluoro, too.

Efforts will be made to provide a fully automatic fusion of preoperatively planned information and intraoperative monitoring information into the high resolution 3D intraoperative scan. This will include the development of fast and automatic 3D-3D angiographic registration algorithms (as proposed e.g. by [5, 4, 29, 83]) aligning pre- and intraoperative reconstructions as well as the incorporation of 2D-3D algorithms to update this registration. Moreover, in order to backproject monitored instruments to 3D, 2D-3D deformable registration, motion compensation, and 2D catheter tracking will become of importance. The integration of prior information (e.g. type of treatment, instruments used) into registration and tracking algorithms will be a major issue in the near future.

Part II.

New Algorithms
for
2D-3D Angiographic Registration

4. Clinical Application

In part I angiography as it is used in the clinic has been introduced, concepts for 2D-3D registration have been explained, and 2D-3D registration algorithms for angiographic images have been reviewed. Chapter 1 has given a general motivation and justification for a registration system that can be used for abdominal catheterizations.

Now, we want to have a closer look at a particular abdominal procedure, Chemoembolizations of liver tumors. After shortly introducing medical indication and procedure (4.1, 4.2, and 4.3), we will illustratively use this intervention to show feasibility, difficulties, and issues of 2D-3D registration in section 4.4. Moreover, we will critically examine all previously reviewed alignment methods for applicability in abdominal chemoembolization and thus liver catheterizations.

In the remainder of part II, two rigid and one deformable registration algorithms will be presented particularly tailored to meet the requirements of catheterized interventions in abdominal areas. Chemoembolization data will always be used to show their applicability on real data sets.

4.1. Medical Excursion: Liver Vessel Systems

The liver, as the second largest organ of the human body, plays a major role in metabolism and also serves a number of functions for storage and detoxification. Thus, there is a considerable amount of blood traveling through the liver in order to deliver nutrients or for being “washed” from toxics. There are four vessel trees in the liver. One is the liver arterial tree or hepatic artery delivering oxygen-rich blood from the aorta to the liver. The arterial vessels have a diameter between $1\text{mm} - 5\text{mm}$. Two venous systems are located in the liver, the hepatic veins that drain blood from the liver, and the portal venous system starting with the portal vein that carries nutrition-enriched blood from the small intestine to the liver. Hepatic veins have a diameter between $6\text{mm} - 12\text{mm}$, whereas the portal venous system usually covers a range from $6\text{mm} - 17\text{mm}$. All vessels end up in capillaries with a diameter down to $5\mu\text{m}$. As can be deduced from the respective sizes, the portal vein plays the major role in blood supply for the liver. Approximately 75% of the blood flow to the liver comes from the portal venous system, about 25% comes from the hepatic artery. A fourth vessel system is the hepatic duct as part of the biliary system, which transports bile from the liver to the gallbladder. An illustration of the liver vessel systems is shown in Figure 4.1¹.

¹From The Merck Manual of Medical Information - Second Home Edition, p. 787, edited by Mark H. Beers. Copyright 2003 by Merck & Co., Inc., Whitehouse Station, NJ. Available at: <http://www.merck.com/mmhe/sec10/ch133/ch133a.html>. Accessed July 12th 2007.

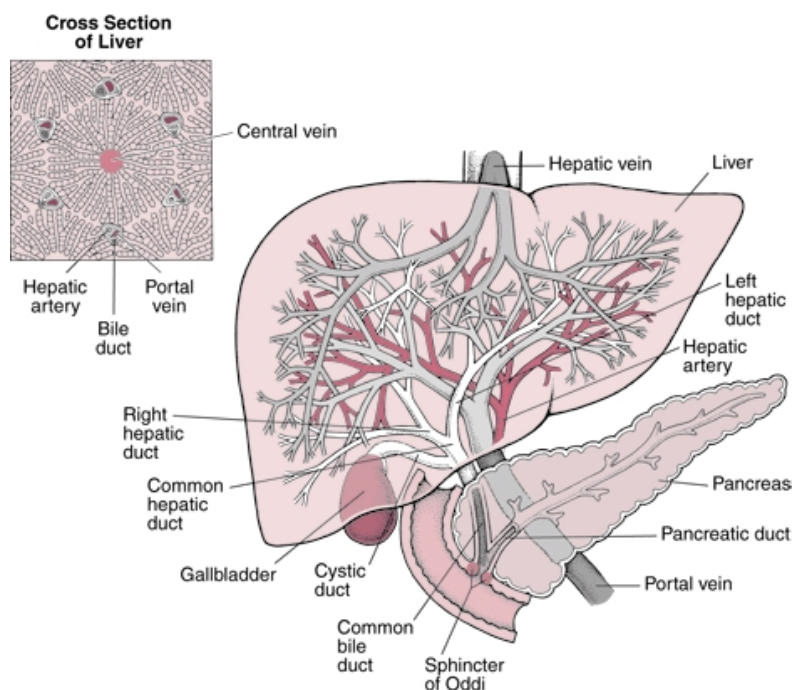


Figure 4.1.: The vessel system of the liver

4.2. Treatment of Liver Tumors

A liver tumor (hepatocellular carcinoma, HCC) is an abnormal growth of cells in a mass or a lump, distinguished by its malignancy and whether it has evolved in the liver (primary liver tumor) or has been delivered from another part of the anatomy (secondary liver tumors, metastases). The main causes for liver tumors are alcoholic cirrhosis, hepatitis B, or C, and intoxication. Tumors can be detected via anamneses², a blood test (in case of hepatitis), or adequate imaging modalities. Even though the main blood supply of the liver comes from the portal vein, HCCs are exclusively supported by hepatic arteries.

There are three possible treatments for liver cancer, surgery, radiation therapy, and drug treatment. A surgery is the most severe intervention which cuts either parts of the liver (liver resection) or replaces the liver entirely (liver transplantation). Anastasis for liver resection is rather long compared to minimally invasive treatments and does not guarantee a total recovery. Liver transplantations naturally cure a liver cancer entirely, however, organ supply is short and expensive. Treatment by medicine applies cytostatica to the patient in order to destroy malignant (tumor) cells. This procedure is also called chemotherapy and is mainly used when a tumor has spread in the body and cannot be treated locally any more. Sometimes, it is also applied additionally to surgery in order to improve operability / recovery or to kill not ascertainable tumor cells after treatment. Minimally-invasive procedures

²The elicitation of a patient case history, particularly using the patient's recollections

for liver treatments are used more frequently in hospitals nowadays since they can be performed almost ambulant. Typically, only small incisions are made, instruments are injected therein, and guided to the region of interest where the therapy is carried out. The guidance is monitored by appropriate imaging devices (for example C-arms). Minimally-invasive treatments are not as demanding to the patient's health compared to conventional methods. However, they are seldomly used to fully cure patients from liver carcinomas but instead to relieve patients from pain and improve their quality of life (palliative therapy).

One such minimally-invasive treatment, which is carried out on a regular basis (5-10 times per week) in hospitals is a Transarterial Chemoembolization (TACE). Here, in order to apply local chemotherapy and embolizing the blood vessels supporting the tumor, a catheter is inserted into the arterial vasculature in the hip region and guided to the tumor's location using X-ray imaging (see fig. 4.2). Since the embolizing liquid dissolves after a few days, this treatment is repeated on a regular basis for one patient.

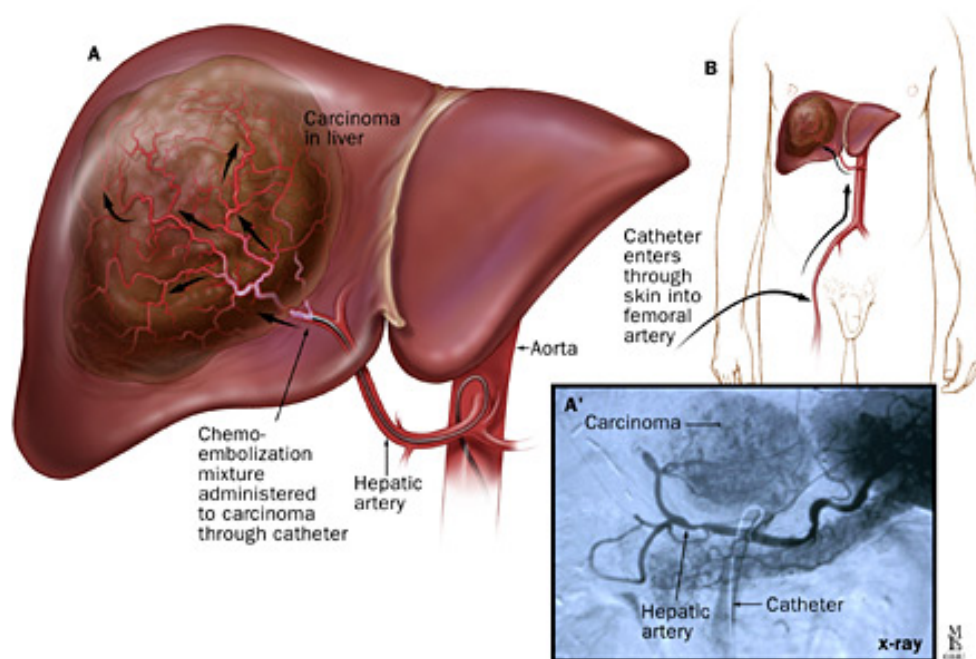


Figure 4.2.: A transarterial chemoembolization. With courtesy of Dr. Jeff Geschwind, Johns Hopkins University

In the following, we will have a look at work- and dataflow of the TACE procedure, and deduce the necessity for 2D-3D registration from it.

4.3. Workflow of Transarterial Chemoembolizations

Once a tumor has been detected and the patient is scheduled for TACE, a preoperative 3D scan is performed one day before the treatment. This scan is usually acquired via CTA or MRA and gives information about the location of the tumor, the configuration of blood vessels that a catheter must be guided through, and possible complications due to medications the patient has received so far.

Once the procedure has been planned and the patient is accepted for treatment, TACE is started by injecting a catheter into the femoral artery of a patient who is not or only partially anesthetized. From then on, a C-arm is used to monitor the catheter as it is guided through the arterial system. Usually, a DSA is acquired providing a vascular overview once the catheter has reached the aorta (see Figure 4.3a). Then, it is guided via constant fluoroscopy imaging into the hepatic artery. DSAs are frequently acquired to find the location of the tumor (Figure 4.3b). The catheter is led to the artery supporting the tumor (Figure 4.3c), cytostatica are applied, and the vessel is embolized.

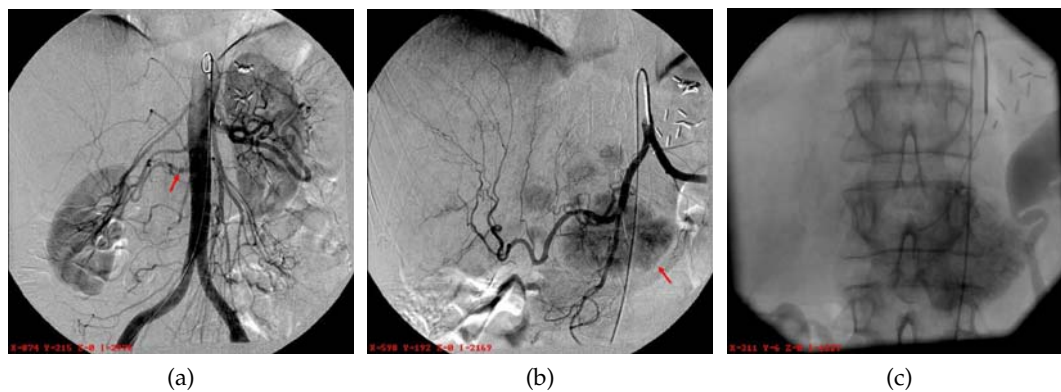


Figure 4.3.: A chemoembolization workflow shown by different X-ray projections. (a) shows an overview of the vessel anatomy. The red arrow indicates the hepatic artery. (b) shows a state where the catheter is inside the hepatic arterial system. The red arrow indicates the tumor region. (c) shows a fluoroscopy image of the state where the catheter has reached the tumor region.

Only a DSA where the catheter is near enough to the tumor region can visualize the HCC. As can be seen in Figure 4.3, the overview DSA does not show the tumor. Moreover, the fluoroscopic image does not show vessels at all or only temporarily if contrast agent is administered. Note also that the fluoroscopic images are acquired from one view only.

Currently, the 3D preoperative information is not brought to the interventional room. It would, however, be beneficial for the operating physician to know the position of the catheter in 3D with respect to vessels and tumor. Interventionalists often have to change the angulation of the C-arm to have a better depth perception, which

could be avoided if preoperative data is fused with the 2D projection. As already mentioned in the introduction the issues of blind navigation, reduced depth perception, and patient motion could be addressed if a 2D-3D registration is available and catheter information is transferred to the 3D preoperative data set.

Even though the goal of this thesis is to provide accurate and robust methods for 2D-3D registration in this context, the task of information fusion of intraoperative instruments and preoperative data needs to address more issues. First, in order to keep the registration updated while fluoroscopic images are acquired and the patient keeps on breathing, a tracking algorithm has to be developed compensating for breathing movement. Moreover, the instrument, i.e. the catheter has to be located (or at least its tip) to have the 2D coordinates for backprojection into space. Last but not least, a suitable visualization technique for data fusion must be provided, giving the interventionalist an intuitive interface for catheter navigation.

After the presentation of 2D-3D angiographic registration techniques aligning pre- and intraoperative data sets, we will address the three aforementioned issues in the Conclusion of this thesis, in chapter 7.

4.4. Feasibility of 2D-3D Registration

In the following, the problem will be analyzed with respect to the available data. Only if similar structures can be found in 2D and 3D data set a registration can be accomplished. Moreover, we discuss the particular difficulties when registering TACE data. Finally, we will reiterate over all the reviewed registration methods and evaluate their applicability to 2D-3D registration on TACE images.

4.4.1. Data Availability

Preoperative Data The current workflow for chemoembolizations in our partner clinic involves a three-phase CTA scan of the liver region consisting of native, arterial dominant, and portal-venous phase visualizing especially the portal venous system, faintly the arteries, and the hepatic veins. The native scan is done to detect already existing embolization liquid in the liver. The arterial dominant phase allows for detection of new malignancies, and, together with the venous phase, shows the radiologist whether a treatment is possible with the current vessel configuration.

During the intervention, however, only arteries are visible in the 2D data sets, no portal or hepatic vessel systems, such that until now 2D-3D registration was not possible. We create a strong link between diagnostic radiology and intervention by defining a new protocol for the preoperative scans, introducing one additional run of an *angiographic* phase that visualizes liver arteries (delay times with bolus tracking: 6 (angiographic), 10 ± 2 (arterial dominant), 21 ± 4 (portal-venous) seconds), see Figure 4.4. The aim is to let the interventionalist benefit from 3D high resolution CTA scans during the intervention. We have acquired several data sets using a state-of-the-art 64-slice CT imaging device (Siemens Sensation 64). The spatial precision of the acquired scans could be reconstructed to $0.58 \times 0.58 \times 0.6 \text{ mm}^3/\text{voxel}$ in a

$512 \times 512 \times (280 - 500)$ *voxel* volume making it possible to extract vessels with a diameter down to $1 - 2\text{mm}$.

As confirmed by physicians, the additional radiation exposure (approximately 6 mGy) is acceptable for patients undergoing a chemoembolization treatment. This new scan protocol is used to perform the registration. As a result, path planning can be performed and intraoperative 3D visualization can be offered.

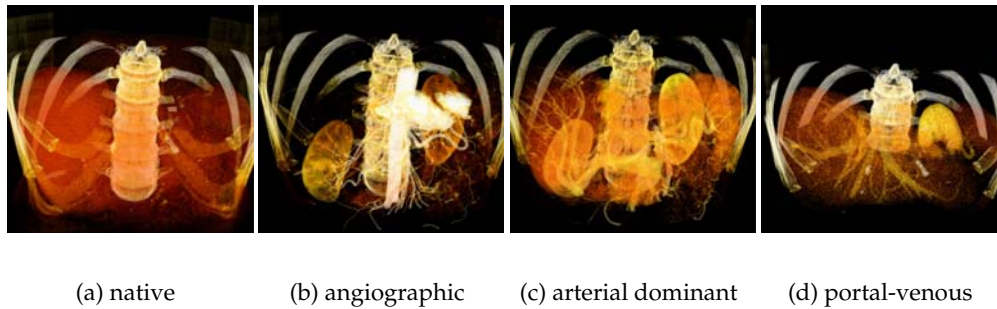


Figure 4.4.: The new 4-phase CT protocol

Intraoperative Data We choose to register the preoperative data set to a DSA. Fluoroscopic images show bone structure, which could be used for rigid registration. However, the structure to be aligned is the vessel system that is subject to motion (rigid and non-rigid), which cannot be inferred from the skeletal structure³. Thus, a registration algorithm should focus on the structure of interest, the vasculature, supporting the use of DSAs. Moreover, for feature-based registration algorithms, an extraction of vessel features is necessary, which can be accomplished easier using DSAs compared to contrasted fluoroscopic images due to a better signal-to-noise ratio and less artifacts.

4.4.2. Challenges

Even though the preoperative acquisition is altered to provide necessary information common to both pre- and intraoperative data set, there are still some challenges that have to be coped with.

Contrast Difference First, contrast injection is performed globally for the preoperative, locally for the intraoperative data set. Thus, contrast propagation stops earlier in the vessel structure in preoperative data, while thinner vessels are visible in intraoperative data. A registration based on vessel structures has to discard those outliers in the 2D data set. Moreover, possible segmentation errors as well as the global contrast propagation can introduce vascular outliers in 3D, too.

³Breathing motion, for instance, induces different transformations on organs (and thus vessels), ribs, or spine

Small Vessels As already mentioned in 4.1, hepatic arteries have a diameter of $1 - 5\text{mm}$ making it difficult to provide a proper segmentation. Particularly in a pre-operative CTA small arteries shrink to the size of one voxel only, making segmentations prone to errors caused by noise. These segmentation errors either have to be compensated by a suitable vessel extraction algorithm, or have to be considered during 2D-3D registration.

Breathing Movement Due to patient breathing the vessel structures are deformed [151, 125]. Either the deformation is taken into account by the transformation model, or deformed vessels have to be detected and discarded for a rigid registration method. Moreover, a DSA usually shows artifacts (a displaced catheter or rib contours, see Figure 4.3), which have to be taken into account during registration. A 2D segmentation algorithm has to be robust against such artifacts, and a 2D-3D registration based on intensities must not be disturbed by them.

Single View Our clinical partners only use a single view C-arm for TACE treatment as do most other hospitals for abdominal catheterizations. Thus, no 3D reconstruction and 3D-3D registration approach is possible in this specific scenario. The depth information has to be inferred from one view only, making a deformable alignment particularly difficult, see 3.4.

Fast and Automatic A registration algorithm must be fast and automatic since it will be used during the intervention. While preoperative data can be (semi-)manually segmented, the 2D vessel extraction should be as automatic as possible, or the registration has to be computed without 2D segmentation. Moreover, a registration should not require a manual pre-alignment, proper initialization routines have to be provided for applicability.

4.4.3. State-of-the-Art Applicability to TACE

We will now highlight advantages and flaws of approaches already proposed in the literature, and discuss their applicability to TACE data.

Feature- vs. Intensity-Based Registration Pure intensity-based registration for angiographic alignment of TACE data is rather difficult to achieve. First, most of the intensity-based approaches that have been reviewed above need a segmentation of the 3D vasculature, which makes it unreasonable to not at least use attributes like diameter and centerline of the preoperative data set. The methods based on MIP approximations of DRRs are not likely to work due to the small nature of hepatic arteries. A MIP of the arterial vascular system of the liver will be prone to error due to noise and alignment might fail especially if the depth information gathered during MIP is used in the registration process as proposed by Kerrien *et al.* [73].

Deformation and Size Bias of Intensity-Based Methods Liver arteries deform during patient breathing. Unfortunately, it can occur that also thick vessels deform vastly (see chapter 6), which makes it difficult to align the images according to them. Methods based on intensity similarity measures tend to align vasculature biased by the diameter of the vessels. The larger the vessel, the more influence it gains in the similarity measure. However, due to non-rigid motion, vessels with different sizes should rather be treated equally in order to attain more robustness against deformation. This makes a registration using the methods of Hipwell [68, 101, 23], Day and Napel [39], Turgeon [145], or Chan [27] difficult in abdominal regions.

Furthermore, we find it also crucial for a registration algorithm to have information about 2D vessel geometry, topology, and diameter properties. In this respect, 2D vascular segmentation is an important step in our opinion, and we will show in chapter 5 that a mere normalization of vessel radius and an avoidance of 2D segmentation as proposed by Jomier *et al.* [70] is not sufficient for a successful registration in some clinical cases.

Automation A high level of automation must be achieved intraoperatively in order to make the algorithm applicable for TACE procedures. A tedious manual segmentation of 2D data is to be avoided, which excludes some approaches (e.g. that by Alperin *et al.* [1], Liu *et al.* [88], or Vermandel *et al.* [150]) for 2D-3D registration used on chemoembolization image data. Moreover, automatic initialization is an important issue and the capture range of algorithms should be high. We will propose and discuss suitable automatic initialization techniques to find an initial estimate in the vicinity of the true registration parameters.

Deformable Registration Non of the reviewed methods is solving for a local transformation acknowledging the deformation introduced by patient breathing and presence and advancement of the injected catheter. It is doubtful whether the bitangent properties derived by Feldmar *et al.* [41], or the region-based correspondence search as described by Kita *et al.* [77] still work in this deformable environment. In the following chapter, we will propose two rigid registration algorithms, which are both robust against deformation changes and solve for transformation parameters as well as one-to-one correspondences. We link these results to a deformable 2D-3D registration algorithm in chapter 6, which for the first time addresses the difficult problem of non-rigid vascular alignment of a 3D image to a single 2D projection.

5. Rigid 2D-3D Registration of Angiographic Images

This chapter introduces two methods for rigid registration of 3D CTA to 2D DSA images of abdominal catheterizations.

In the first two sections, 5.1 and 5.2, we will provide details on the model of the C-arm we use for deducing the registration parameters and explain the preprocessing of the data we have to apply to retrieve the data structures that are used for alignment.

Next, the bifurcation-driven registration will be discussed in section 5.3, a method to register two vascular graphs using bifurcation points and topological graph information to adapt 3D to 2D feature space. In section 5.4 we will introduce the second rigid registration algorithm, in which the alignment is driven by an iterative 2D segmentation refining feature spaces for correspondences. Both methods will be subject to extensive testing, and a method for creating a simulated DSA image with a ground truth registration is developed to evaluate accuracy and robustness of the second algorithm since it is using 2D image intensities in the registration process.

Integrating the registration results into clinical workflow will be postponed to chapter 7. Registration-induced visualization and a subsequent catheter tracking method will be discussed there.

5.1. C-arm Model

The presented model interprets the calibration matrix \mathbf{K} and extrinsic parameters $[\mathbf{R}|\mathbf{t}]$ of a pinhole projection in the context of a C-arm setup. For an illustration refer to Figure 5.1. All images were acquired with C-arms of the Axiom series of Siemens Medical Solutions.

Intrinsic Parameters We assume an absence of distortion due to flat panel detector technology or correction by calibration. The intrinsic parameters can be received from the calibration given by stationary C-arms for reconstruction purposes (or interpolated from them as explained in 2.4.2).

The focal length f_x, f_y is given in mm by a calibrated field of view (FOV), image width h_x and height h_y , aspect ratio a , and the pixel pitch m_x, m_y :

$$f_x = m_x \frac{h_x/2}{a \tan FOV/2} \quad , \quad f_y = m_y \frac{h_y/2}{\tan FOV/2} \quad (5.1)$$

The principal point (p_x, p_y) is either given by calibration, or, if not available, an approximative value is given by the center of the image $(h_x/2, h_y/2)$.

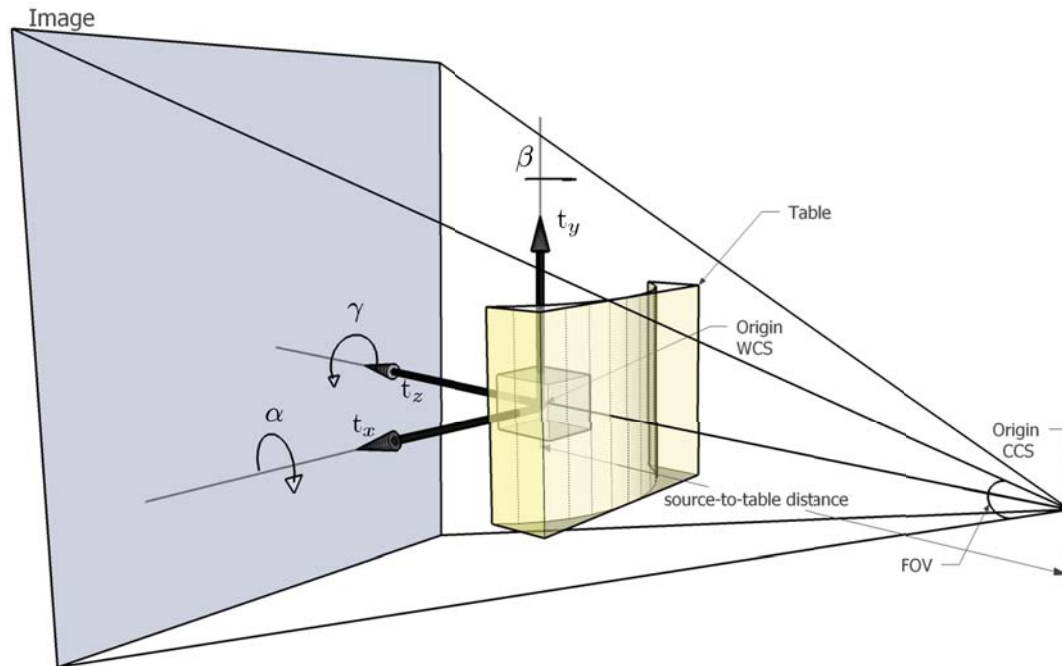


Figure 5.1.: 6 rigid body parameters in a C-arm setup

Extrinsic Parameters The origin of the WCS (center of rotation) is placed in the middle of the moving 3D image, where a right-handed coordinate system spans a plane by x - and y -axis parallel to the image plane. Moreover, the WCS origin is located on the ray connecting CCS origin and principal point, making the z -axis lie on the principal ray. Since C-arm geometry places the 3D object between X-ray source and image plane, the following interpretation of the 6 rigid-body parameters can be deduced:

- α : rotation around horizontal axis of image, *secondary angle of C-arm*
- β : rotation around vertical axis of image, *primary angle of C-arm*
- γ : rotation around principal ray
- t_x : in-plane translation along horizontal axis of image, *perpendicular table translation*
- t_y : in-plane translation along vertical axis of image, *parallel table translation*
- t_z : out-of-plane translation along the principal ray, *table translation towards X-ray source or detector*

The rotation matrix \mathbf{R} is then given by the matrix representation of the Euler angles (α, β, γ) , and the translation $\mathbf{t} = (t_x, t_y, t_z)^\top$.

5.2. Preprocessing

For all proposed methods, we developed a graph representation of centerlines and bifurcations of vessel structures attributed with the diameter at each location. The process is divided up into three stages: the vascular segmentation (section 5.2.1), the extraction of centerlines, bifurcations, and diameters (section 5.2.2), and the creation of the graph structure (section 5.2.3). A visual overview of all steps is given in Figure 5.2.

5.2.1. Segmentation

CTA Segmentation Since contrast agent is applied globally in a CTA scan, its propagation is uniform and rather straightforward to segment. Thus, we choose a region growing algorithm to extract the vascular structure, as described in 2.2.4. In order to avoid the region growing to stop due to noise, a smoothing is applied. The smoothing has to be edge-preserving since small vessels are important to be covered by the algorithm and leakages due to low contrast difference should be avoided. Therefore, the 3D volume of the angiographic scan is filtered with anisotropic diffusion [119] before the user has to place a seed point at the beginning of the arterial tree to be segmented.

The angiographic phase of CTA shows contrasted aorta and the arterial system of other organs than the liver, too. The user manually selects a point in the vicinity of the hepatic artery where it leaves the aorta. By automatically drawing a cube with the size of the hepatic artery, the region growing is stopped and redundant vascular information that is not visible in the intraoperative image can be discarded.

As can be seen in Figure 5.2b this segmentation technique yields good results for the extraction of hepatic arteries from the angiographic CTA scan. However, as was assessed manually, very small vessel structures cannot be segmented using a region growing due to noise. Level Set methods (see 2.2.4) could provide a better segmentation in terms of vessels with a diameter of less than two pixels. However, we preferred the region growing technique since it provides reasonable results for 2D-3D registration, is computationally fast, easy to implement, and the segmentation can conveniently be refined manually.

DSA Segmentation In 2D DSAs, the SNR is higher compared to 3D CTAs, making it necessary to use a more sophisticated vessel enhancement filter. A background removal is performed by applying a bothat filter (closed image minus original image) followed by a multiscale vesselness filter assigning the probability of lying in a tubular structure to each pixel as described by Frangi *et al.* [47]. Again, a region growing algorithm extracts the vessel structure from one or several seed points.

5.2.2. Extraction of Graphs

From the segmented data sets one can easily extract a centerline image by applying topology-preserving thinning algorithms in 3D and 2D [113]. A wave propagation

algorithm [162] extended to cope with loops is used to create a graph from this centerline [112]. By advancing a set of waves and testing their fronts for connectivity, a graph can be created with bifurcation nodes at branching points of the vessel tree and segments consisting of sampling nodes in between (see Figure 5.2). Mind that the position of ramification points is directly depending on the thinning algorithm. Since thinning is an approximation to MAT [14], the (unique) bifurcation lies on the center of the largest sphere that can be fitted into the segmented vasculature.

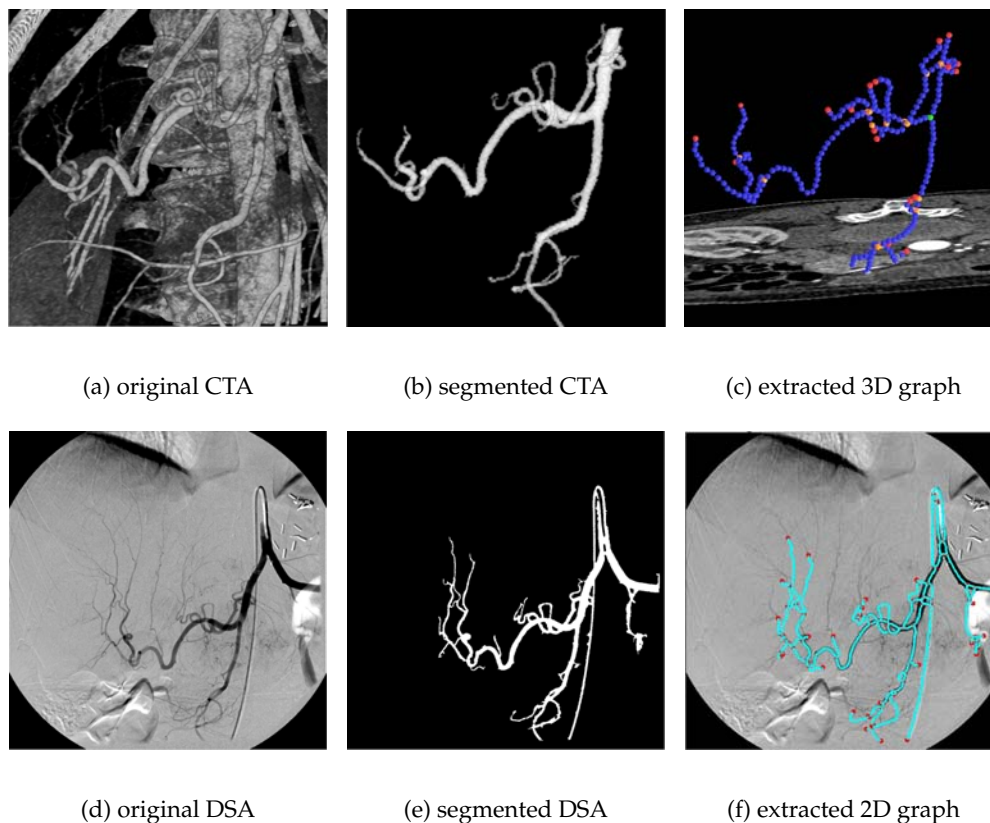


Figure 5.2.: Preprocessing in 3D/2D. Figure (a) shows the volume rendered CTA, (b) shows the segmented vasculature, (c) the extracted graph, where the green point is the root node, orange points inner, red points outer bifurcation points, and blue points represent sampling points of the vessel segments. Figure (d) and (e) show original DSA and its segmented vasculature. Figure (f) shows the 2D graph (turquoise are sampling, red are bifurcation points)

Points between each bifurcation are sampled and stored as edge labels to keep edge position information. The size of a wave should be set to the desired sampling rate of segmented vessels, which can be down to 1 pixel or voxel. Note that a vessel graph in 3D is not necessarily a tree since there can be anatomical loops in the vasculature as has been confirmed by physicians. Since the thinning algorithm still introduces some wrong branches due to noise, edges smaller than the vessel diame-

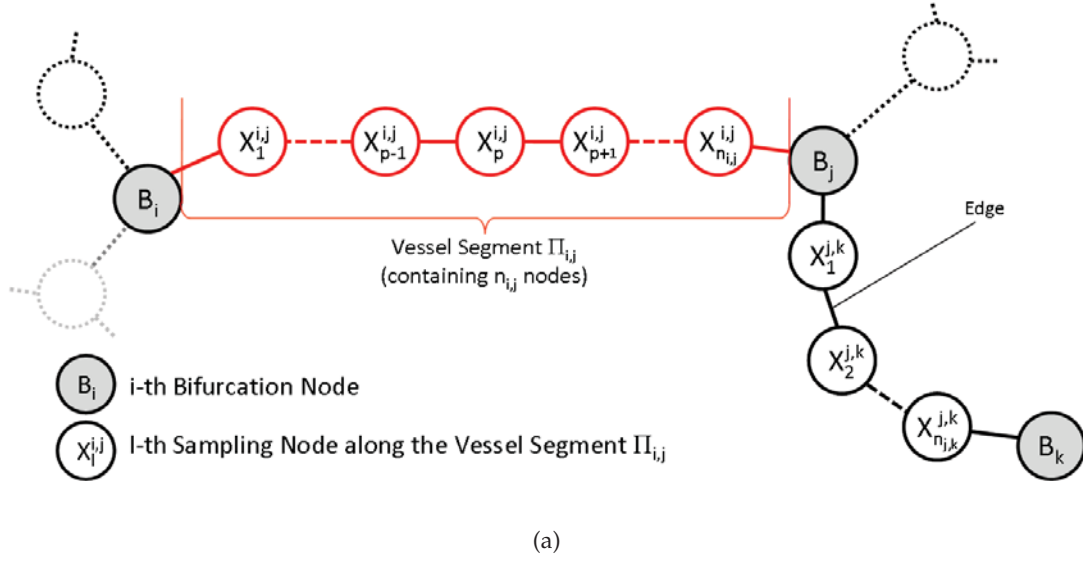


Figure 5.3.: Illustration of the used graph structure.

ter are removed with a Euclidean distance map of the segmented data sets. For the same reason and in the same way very adjacent bifurcations are fused together.

The diameter of the vessels is computed using a distance map of the segmented image. The distance map is created such that the largest Euclidean distance to the contour is given inside the segmentation. On each centerline point, the radius, and hence the diameter can be determined thus, as described in section 2.2.5.

5.2.3. Graph Representation of Vessel Centerlines

We model vessel structures as directed graphs $G^d = (V^d, E^d)$, with a set of n nodes $V^d \subset \mathbb{R}^d$ and the connecting edges $E^d \subset V^d \times V^d$. Here $d \in \{2, 3\}$ denotes the dimension of the graph. For the following, please refer also to Figure 5.3.

The nodes are classified either as bifurcation nodes V_b^d or sampling nodes V_s^d , such that $V^d = V_b^d \cup V_s^d$ and $\emptyset = V_b^d \cap V_s^d$. While the bifurcation nodes express the topology and the rough geometry of the vessel tree, the sampling nodes are used to describe the geometry of the vessel segments in more detail.

A general graph node is abbreviated by $\mathbf{V} \in V^3$, and $\mathbf{v} \in V^2$, in order to distinguish between the two dimensions we are working on.

The bifurcation nodes are abbreviated by \mathbf{B} in 3D and \mathbf{b} in 2D and are identified with their spatial coordinates, such that $\mathbf{B} \in V_b^3$, $\mathbf{b} \in V_b^2$.

We denote the sampling nodes by \mathbf{X} in 3D and \mathbf{x} in 2D and again identify them with their spatial coordinates.

We define a vessel segment $\Pi_{i,j}$ as a path between two neighboring bifurcation nodes \mathbf{B}_i and \mathbf{B}_j , containing all sampling nodes and edges between \mathbf{B}_i and \mathbf{B}_j . The number of nodes in $\Pi_{i,j}$ is $n_{i,j}$ and the number of edges respectively $n_{i,j} + 1$. The

sampling nodes are indexed relative to the vessel segment $\Pi_{i,j}$ starting from 1 to $n_{i,j}$, compare Figure 5.3. The correspondences are also ordered relative to the respective vessel segment.

We will also use a *topological* version of a graph $G^t = (V^t, E^t)$, where $V^t = V_b^d$ are only bifurcation nodes, and $E^t \subset V_b^d \times V_b^d$ represents the ramification topology of the vessel structure.

5.3. Bifurcation-Driven 2D-3D Registration

Given 2D and 3D graphs from the newly introduced angiographic CTA scan and the DSA image, the aim is now to recover the 6 extrinsic parameters to form $[\mathbf{R}|\mathbf{t}]$. This is an easy task if correspondences are given, in our scenario, however, corresponding information is not available and has to be determined as well.

In the following method we use the fact that bifurcation locations are distinct, and well-defined. Moreover, bifurcations form a space of correspondences between 2D and 3D graph structure. In a first step, the algorithm is initialized by finding one bifurcation correspondence via a-priori information of the patient location and iterative (x, y) -translation. Fixing this correspondence, a nonlinear optimization is performed on a reduced parameter space iterating over 3 rotational and 1 translational parameter. Good feature correspondences are iteratively created for the matching by recurrent graph creation of the projected 3D centerline image.

5.3.1. Initialization

State-of-the-art angiographic C-arm devices store lots of information concerning imaging geometry. Each 2D angiogram is provided with the calibration matrix \mathbf{K} , and a source-to-table distance (STD , see Figure 5.1). Moreover, a primary and secondary angle provide a good initial estimate of the rotation matrix $\tilde{\mathbf{R}}$.

We use all this information to produce initial image as well as object coordinates of the extracted vessel trees. For all node coordinates of the 2D centerline graph $\tilde{\mathbf{v}}_i$ we undo the transformation specific to the imaging device:

$$\hat{\mathbf{v}}_i = \mathbf{K}^{-1}\tilde{\mathbf{v}}_i \quad (5.2)$$

For all node coordinates of the 3D centerline graph $\tilde{\mathbf{V}}_i$, we apply an initial transformation including primary and secondary angle $\tilde{\mathbf{R}}$ (assuming $\gamma = 0$) and an approximate z-translation $\tilde{\mathbf{t}}_z = (0, 0, STD)^\top$:

$$\mathbf{V}_i = \tilde{\mathbf{V}}_i\tilde{\mathbf{R}} + \tilde{\mathbf{t}}_z \quad (5.3)$$

Naturally, the values of rotation parameters and z-translation are just a rough estimate and subject to further optimization as described in the following section.

Registration of x-y-Translation This step tries to find a 2D correspondence to the bifurcation in 3D with the largest vessel attached, which is called the root. After

setting the a-priori information, we iteratively translate the 3D graph in x - and y -direction parallel to the image plane such that the root's projection is laid over 2D bifurcations with high diameter. The energy \mathcal{E}_{topo} , described in Equation (5.7), is evaluated and the (x, y) -translation yielding the lowest value is chosen. Thus, we find one corresponding vertex and reduce our optimization problem to recovering three rotational parameters (\mathbf{R}) and one translational parameter t_z along the ray connecting the X-ray source position to the projected root on the image plane.

5.3.2. 4 DOF Optimization

Geometric Optimization of Rotation and z-Translation 2D-3D registration problems are twofold: recovery of corresponding information and estimation of rigid transformation. Since vessel structures can be interpreted as a set of curves, the Iterative Closest Point (ICP) algorithm [163, 11] could be incorporated for finding both, matches and transformation parameters. Let $C(G, \mathbf{y})$ be a function determining the point of graph G closest to a given point \mathbf{y} , an energy \mathcal{E}_{icp} can be defined by

$$\mathcal{E}_{icp} = \sum_i^{n_2} \|C(G_{2D}, f_{[\mathbf{R}|t_z]}(\mathbf{V}_i)) - f_{[\mathbf{R}|t_z]}(\mathbf{V}_i)\|^2, \quad (5.4)$$

where G_{2D} is the 2D vessel graph, \mathbf{V}_j , $j = 1 \dots n_2$ are all points representing the 3D vasculature (bifurcations and segment sampling points). With $\mathbf{t}_z = [t_x, t_y, t_z]^\top$ we indicate that only t_z is subject to optimization, t_x, t_y are fixed.

\mathcal{E}_{icp} has many local minima since projected points of one 3D vessel segment could easily be driven to different, not corresponding 2D vessel segments in the optimization process. Moreover, even with outlier detection via an adaptive distance threshold based on statistical analysis [163], the energy would yield wrong alignment due to deformation.

If we do not focus the correspondence search on all curve points but only on dedicated ones that are likely to be detected in both data sets, we can improve the estimation process. Bifurcation points can be detected in 2D and 3D data sets very easily and represent good descriptors for a projection of vasculature since they are distributed over the whole vessel tree and are distinct to each other. Hence, we restrict our energy only to these good features, the ramifications of the vessel graphs:

$$\mathcal{E}_{bif} = \sum_i^{n_3} \|C(\{\mathbf{b}_j\}, f_{[\mathbf{R}|t_z]}(\mathbf{B}_i)) - f_{[\mathbf{R}|t_z]}(\mathbf{B}_i)\|^2, \quad (5.5)$$

where $\mathbf{b}_1, \dots, \mathbf{b}_{n_{2D}}$ and $\mathbf{B}_1, \dots, \mathbf{B}_{n_3}$ are bifurcation points of the 2D and 3D graphs, respectively. Only inner bifurcations can be used since leaves in the graph account for the end of contrast propagation, which is different in 3D and 2D data set.

Unfortunately, segmentations and hence extracted graphs of the data sets are often very different due to local and global application of contrast agent. Moreover, the projection also produces crossings of vessels that cannot easily be detected and resolved since vessels can also be tangent to each other. This can be dealt with by performing a new graph extraction on the projected graph's centerline image in each

iteration (see fig. 5.4). The centerline image is created by drawing the 3D graph as a one-voxel-wide centerline in a volume and projecting the volume with the current imaging parameters. The new energy can be stated now as

$$\mathcal{E}_{extract} = \sum_i^{n_4} \|C(\{\mathbf{b}_j\}, \mathbf{b}_i^f) - \mathbf{b}_i^f\|^2, \quad (5.6)$$

where $\{\mathbf{b}_1^f, \dots, \mathbf{b}_{n_4}^f\}$ is the inner bifurcation list (without leaves) of a graph, which is created as follows:

- From 3D graph G_{3D} a centerline volume \mathcal{A} is created.
- \mathcal{A} is projected with projection function $f_{[\mathbf{R}|\mathbf{t}_z]}$ to yield a centerline image \mathcal{A}^f .
- A new graph G^f is extracted from the projected graph's centerline image \mathcal{A}^f starting at the location of the projected root vertex.
- Only the inner bifurcations of G^f are put into the resulting set $\{\mathbf{b}_1^f, \dots, \mathbf{b}_{n_4}^f\}$

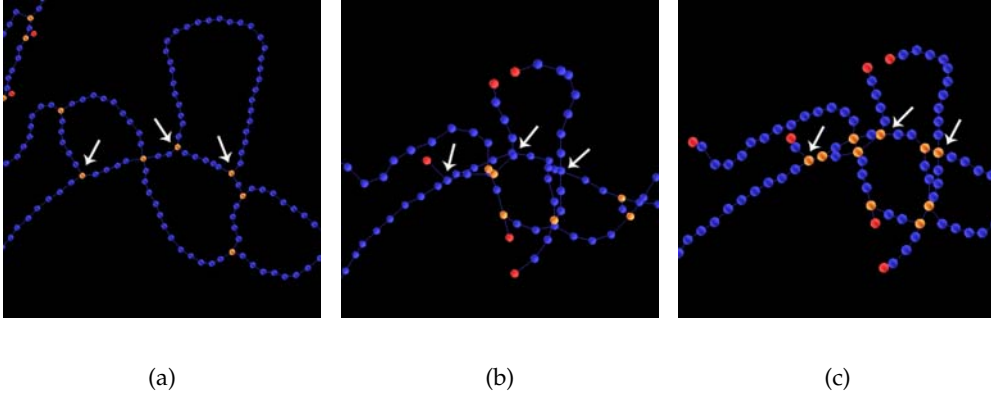


Figure 5.4.: Fig. (a) shows the real 2D graph, (b) the projected 3D graph, and (c) the new created graph from the centerline image of the projected 3D graph. The white arrows show the bifurcations in 2D that are not present in fig. (b), but could be detected by the wave propagation, see fig. (c).

Topological Optimization of Rotation and z-Translation Since we deal with graph structures, we can also incorporate topological information in the registration. Due to different segmentation results in 2D and 3D, the two graphs to be registered do not fulfill the subgraph property and it is not straightforward to do a topology-based graph matching to register the data. However, topological *tendencies* can be used for registration. The degree of each vertex can be used as well as a time stamp coming from a breadth first search to penalize wrong bifurcation matches:

$$\mathcal{E}_{topo} = \sum_i^n r_i^b r_i^d \|C(\mathbf{b}_j, \mathbf{b}_i^f) - \mathbf{b}_i^f\|^2, \quad (5.7)$$

where r_i^b is the ratio of the normalized breadth first search values of the current bifurcation \mathbf{b}_i^f and the closest bifurcation in the 2D graph or its reciprocal if $r_i^b < 1$. r_i^d is the ratio of the degrees of \mathbf{b}_i^f and the closest 2D bifurcation or its reciprocal if $r_i^d < 1$. Graph searches and degrees are computed on the *topological* representation of the respective graphs (see 5.2.3).

Optimization Scheme Due to the high non-linearity of the cost function \mathcal{E}_{topo} a gradient-based optimizer is not used. In each iteration the graph creation changes the number of possible correspondences and the scope of the squared sum differs, hampering the derivation of a valid Jacobian. Therefore, instead of using gradient-based methods, the downhill simplex [123] algorithm was favored.

5.3.3. Algorithm Evaluation

Creation of Reference Registration Experiments have been carried out on synthetic data from 3D head vasculature, a phantom head showing a rigid vessel structure, and on four patient data sets of TACE procedures. For creating (rigid) synthetic ground truth data, we extracted the 3D centerline from the head phantom and projected the resulting graph with rotation and translation typical to a patient-C-arm setup. The transformation was chosen to produce a projection with a similar number of overlays that could be found in real data sets. For the phantom head, a reference registration has been created by intensity-based registration using Gradient Correlation [118] as similarity measure (see Figure 5.5). For the patient data sets a manual registration was provided by experienced radiologists.

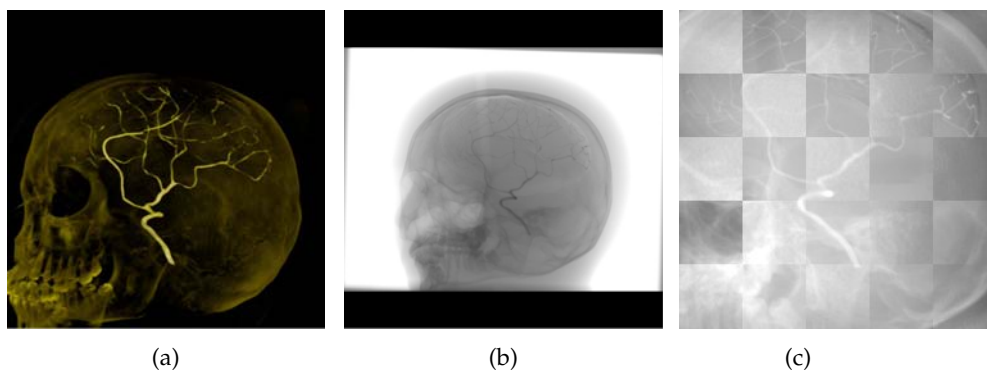


Figure 5.5.: Fig. (a) shows a volume rendering of a 3D head phantom, fig. (b) an X-ray projection of this head. Fig. (c) shows a checkerboard image of inverted 2D and DRR of the reference registration.

Accuracy Measure For accuracy assessment, we used the RSME measure of Equation (2.43), defined between the reference registration parameters and the computed

parameters. In the robustness tests, the standard deviation was also computed in order to account for the stability of the error.

Robustness Test In order to evaluate the convergence and robustness of the optimization, Monte Carlo simulations have been carried out on all data sets. Random displacements in a range of $\pm 10mm$ in translation along the axis connecting X-ray source position to root node (t_z) and $\pm 10^\circ$ in rotation angles (α, β, γ) have been added to the reference pose and the registration procedure was invoked. These displacements are equivalent to a range of 10-50 mm average projection distance of bifurcation points. Note that in order to have the same 3D displacements on all data sets a transformation has to be applied to all coordinates of G_{3D} before the tests, such that the WCS origin is located in the center of the volume (which equals the center of rotation).

The algorithm has been invoked from a total of 200 randomly generated simulation poses.

Method Comparison Moreover, we implemented the method of Jomier *et al.* [70] and added errors of up to $\pm 10mm$ and $\pm 10^\circ$. For the realization of Jomier's method, instead of the 1D parameter search as proposed in the original paper, we used a Downhill Simplex optimizer to solve for 6 DOF minimizing the cost function as defined in Equation 3.8. We performed a second test with smaller errors (up to ± 5 mm and $\pm 5^\circ$, equal to 5-25 mm average projection distance of bifurcation points) because Jomier's method solves for all 6 DOF, not only 4.

Results Tables 5.1 and 5.2 show standard deviations and root mean square errors of 200 trials for the 6 degrees of freedom (3 translation and 3 rotation parameters). Rows denoted with M1 refer to results from our method, those with M2 10 show results from Jomier's algorithm with the large error range, those with M2 5 with the small error range.

We did not perform tests for Jomier's method on synthetic and rigid phantom data since no image intensities were created in the former, and no DSA image (only a fluoroscopic image) was available in the latter case, respectively. Our method is sometimes outperformed in z-translation (t_z), which is the translation perpendicular to the image plane. These deviations, however, do not create a large pixel error when projected (about 3 mm average projection distance of bifurcation points). The more important rotation angles and in-plane translation values prove to be more accurate when using our method. Figure 5.6 shows three patient data sets after initialization (a),(b),(c) and after optimization (d),(e),(f). The blue line shows the extracted 2D graph, and the green line the projected 3D graph. As can be observed, the optimization procedure improves the initial alignment up to a deformation of the vessels.

Runtime Finding one correspondence and thus two parameters, t_x and t_y , was successfully performed for each of the data sets. It took between 0.5 and 1.8 seconds

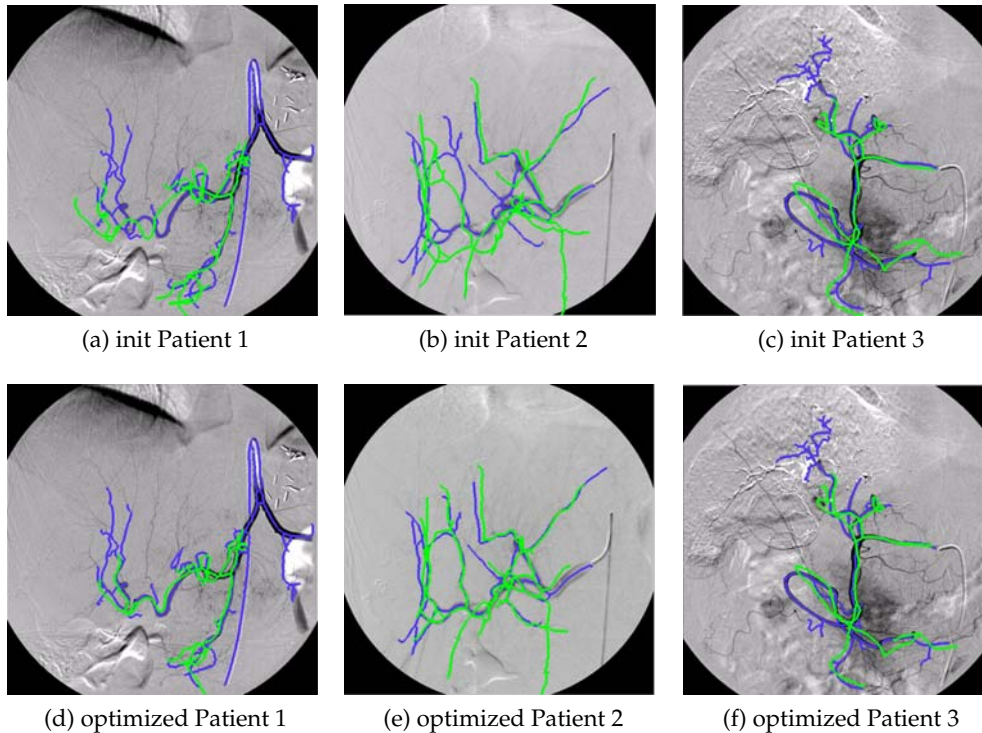


Figure 5.6.: Initialized and registered pose of three patient data sets.

on a 1.6 GHz Pentium machine. The optimization procedure took 2.5 - 6 seconds for phantom and patient data.

5.3.4. Discussion

By developing a 2D-3D registration algorithm based on the newly acquired data, we enable physicians to transfer planning information to the interventional room, and visualize patient anatomy in 3D from the same view point (see 7.1.1). We overcome the difficulty of alignment by conceiving an algorithm, which iteratively generates good features that can be detected easily in 2D and 3D and describe the perspective projection adequately. The algorithm requires user interaction for 3D and 2D segmentation. Since the preoperative 3D segmentation is not subject to hard time constraints, the vasculature extracted by region growing can be refined several times and tailored to thoroughly represent the hepatic arterial system. The intraoperative situation does not allow an extensive user interaction, so we provide a single click technique to start a region growing on a retrospectively enhanced DSA image. Due to the small amount of user influence, the segmentation in 2D is suboptimal, which we account for with a restriction of the registration to bifurcation points only, reducing the number of outliers extensively. With this technique, we also address the inherent difference of vascular images due to global and local contrast injection.

Data	Method	σ_{t_x}	σ_{t_y}	σ_{t_z}	σ_α	σ_β	σ_γ
head simulation	M1	0.0004	0.0005	0.0050	0.0028	0.0010	0.0026
	M2	-	-	-	-	-	-
head phantom	M1	0.0005	0.0005	0.0069	0.0019	0.0009	0.0022
	M2	-	-	-	-	-	-
patient 1	M1	1.3487	1.3982	48.5488	6.2751	2.4778	0.9400
	M2 10	17.9463	43.9687	18.8130	19.8789	19.0780	17.4332
	M2 5	11.9465	35.8826	11.7423	7.9779	11.3076	9.9759
patient 2	M1	0.1463	1.2696	5.0197	4.5966	2.5925	1.2467
	M2 10	2.6396	2.9281	8.0932	7.9089	6.5415	2.0341
	M2 5	1.0204	1.2284	5.5270	5.3732	4.6572	0.6931
patient 3	M1	2.7590	7.5364	45.0523	7.7809	3.9825	7.3726
	M2 10	20.7737	45.7128	16.5745	11.7821	17.2824	21.9335
	M2 5	19.1786	11.3295	8.7508	6.0658	9.9346	4.1008
patient 4	M1	6.9731	1.3264	64.3743	6.3780	8.0713	4.3081
	M2 10	43.3558	13.6386	16.8588	20.1722	24.1609	21.4028
	M2 5	18.4730	5.5094	11.0570	6.7126	20.7805	6.2196

Table 5.1.: Standard Deviations (σ) of Rigid Registration of 200 Monte Carlo simulations in mm for t_x, t_y, t_z and degree for α, β, γ , respectively

Data	Method	RMS_{t_x}	RMS_{t_y}	RMS_{t_z}	RMS_α	RMS_β	RMS_γ
head simulation	M1	0.0389	0.2689	2.2302	0.3966	0.0014	0.5100
	M2	-	-	-	-	-	-
head phantom	M1	0.1104	0.1787	1.2799	0.5842	0.0291	0.6455
	M2	-	-	-	-	-	-
patient 1	M1	1.3815	1.4114	56.2447	6.8791	3.6151	0.9527
	M2 10	22.3263	58.1284	19.6391	19.8301	21.5437	21.6254
	M2 5	13.2387	40.4219	12.8111	7.9678	12.7487	11.5099
patient 2	M1	1.2302	1.4209	28.4073	5.0616	3.8540	2.3298
	M2 10	2.6345	4.1985	8.0793	8.9258	6.6079	2.1112
	M2 5	1.0380	2.8683	5.5190	6.1704	4.6732	0.7196
patient 3	M1	6.5579	7.8977	66.3731	7.9441	11.8805	7.4747
	M2 10	20.7272	61.2542	17.9872	14.4016	19.0442	29.2579
	M2 5	19.3971	11.3037	9.2925	6.2510	15.4947	4.3602
patient 4	M1	10.6187	2.1967	88.9475	8.4271	16.2405	5.5228
	M2 10	49.3440	14.5086	17.0029	21.6873	25.1797	22.1071
	M2 5	19.1812	5.7051	11.2161	7.3732	21.6268	6.3191

Table 5.2.: Root Mean Square Errors (RMS) of Rigid Registration of 200 Monte Carlo simulations in mm for t_x, t_y, t_z and degree for α, β, γ , respectively

5.4. Segmentation-Driven 2D-3D Registration

The bifurcation-driven registration process has performed satisfactory in many clinical cases. However, we have found out that some data sets of liver arteries do not show enough bifurcations (even with the detection of projected bifurcations) to drive the registration to the desired solution, especially when the patient has undergone several treatments already. Thus, we would like to incorporate the full information of vessel segments for registration, not only junction points. Moreover, the user interaction required during intervention is not desirable since time is a critical factor.

We developed an alternative method, which is fully automatic during the inter-

vention and yields good results even if only a small part of the vessel tree is visible or many outliers are present. By coupling a technique for automatic seed point detection developed by Can *et al.* (see 2.2.3) for 2D vascular structures with a region growing step, we avoid user interaction intraoperatively. A combination of registration and 2D segmentation via a probability map allows us to adjust the feature spaces such that non-corresponding features in 2D as well as 3D vasculature are removed consequently while the full vessel curve information can still be used for alignment.

With this approach we combine robustness and high capture range with a fully automatic registration technique. Moreover, one-to-one correspondence of vascular features is assured, which makes it possible to visualize roadmaps in 3D as discussed in chapter 7.

We motivate our method through a *maximum likelihood* (ML) formulation solving for both registration and segmentation. Unlike other algorithms for combined segmentation/registration, we only care about the resulting registration and also leave the algorithm as generic as possible in order to use alternative registration and segmentation steps. In section 5.4.2 we apply our algorithm to 2D-3D DSA-to-CTA registration for abdominal interventions.

Related Work to Combined Segmentation / 2D-3D Registration A combination of segmentation and 2D-3D registration was proposed by Hamadeh *et al.* [64] and Bansal *et al.* [7] for the rigid alignment of medical images. The former only segmented once for aiding the registration, the latter used a minimax-approach in order to optimize one energy functional that encapsulates the joint conditional entropy of DRR and X-ray given a segmentation. A recent method proposed by Brox *et al.* [20] combines pose estimation with a level set formulation to let a registration aid the segmentation. In all these methods, the segmentation is integrated into the algorithm and cannot be replaced. Since vessel segmentation is a specific problem where general approaches cannot be applied without modification we tried to leave the combination as generic as possible and discarded these methods. Combined segmentation and registration has also been successfully applied to brain MR images (see Pohl *et al.* [122] and references therein) where an Expectation Maximization (EM) formulation was favored. In contrast to our proposed algorithm, this work also solves for MR specific nuisance parameters and serves a diagnostic application not subject to hard time constraints.

5.4.1. MLE with Labelmaps

In the following, we will denote the model of a vessel graph G by \mathcal{M} . \mathcal{M} is an instantiation of a random variable M , where all node coordinates of G are stacked up. \mathcal{M} does not own diameter or topological information. We will treat an image \mathcal{I} as an instantiation of a random variable I with intensity values as entries. A labelmap (segmentation) is expressed as \mathcal{L} . A labelmap of size $n \times n$ is built from n^2 indicator labels ℓ_x . Probabilities of a random vector \mathcal{X} will be denoted by $P(\mathcal{X})$.

We want to maximize the probability that certain registration parameters Θ fit best

the 3D model \mathcal{M} to the 2D image data \mathcal{I} , i.e. we want to find a maximal probability

$$P(\Theta|\mathcal{I}, \mathcal{M}) = \frac{\overbrace{P(\mathcal{I}, \mathcal{M}|\Theta)}^{\text{likelihood}} \overbrace{P(\Theta)}^{\text{a priori}}}{\underbrace{P(\mathcal{I}, \mathcal{M})}_{\text{normalizing constant}}}. \quad (5.8)$$

Thus, the Maximum Likelihood estimation (MLE) of the registration is

$$\hat{\Theta} = \arg \max_{\Theta} P(\mathcal{I}, \mathcal{M}|\Theta). \quad (5.9)$$

Maximizing the likelihood of Equation (5.9) is very difficult if there is no correspondence information between image pixels and model points. Thus, we let a 2D segmentation aid the estimation. We introduce a random variable \mathcal{L} representing a labelmap over the image \mathcal{I} . Marginalizing over \mathcal{L} we get

$$\hat{\Theta} = \arg \max_{\Theta} \sum_{\mathcal{L}} P(\Theta, \mathcal{L}|\mathcal{I}, \mathcal{M}) \quad (5.10)$$

$$= \arg \max_{\Theta} \sum_{\mathcal{L}} P(\mathcal{L}|\mathcal{I}, \mathcal{M}) P(\Theta|\mathcal{L}, \mathcal{I}, \mathcal{M}) \quad (5.11)$$

using the product rule. From this formulation we can deduce an iterative scheme. If we had values for variable \mathcal{L} given, we could solve the ML of Equation (5.11). Since \mathcal{L} has to be estimated also, we iterate between expectation estimation (E-step) of the *unknown* random variable \mathcal{L} and optimization of a cost function (M-step) given this expectation:

$$\mathcal{L}^{(t)} \leftarrow \mathbb{E}(\mathcal{L}|\Theta^{(t-1)}, \mathcal{I}, \mathcal{M}) = \sum_{\mathcal{L}} \mathcal{L} P(\mathcal{L}|\Theta^{(t-1)}, \mathcal{I}, \mathcal{M}) \quad (5.12)$$

$$\Theta^{(t)} \leftarrow \arg \max_{\Theta} P(\Theta|\mathcal{L}^{(t)}, \mathcal{I}, \mathcal{M}) \stackrel{ML}{\propto} \arg \max_{\Theta} P(\mathcal{L}^{(t)}, \mathcal{I}, \mathcal{M}|\Theta) \quad (5.13)$$

The M-step (Equation (5.13)) is rather easy to accomplish since we already have a model in 3D (\mathcal{M}) and can determine the MLE using $\mathcal{L}^{(t)}$ in a model-to-model registration, using for example an ICP algorithm.

For the E-step (Equation (5.12)), however, we must determine the expectation value of the labelmap given the last registration and the data. Since this is not straight-forward, we will discuss it in more detail.

Assuming spatial independence of pixels in image \mathcal{I} (which is common in this context, see [122, 7]), we can determine the expectation for each pixel \mathbf{x} separately. If we restrict our segmentation on one object only, we can deduce an indicator variable $\ell_{\mathbf{x}}$ for each pixel \mathbf{x} , where

$$\ell_{\mathbf{x}} = \begin{cases} 1, & \text{if } \mathbf{x} \text{ is inside the object} \\ 0, & \text{otherwise} \end{cases} \quad (5.14)$$

Thus, the expectation for the label $\ell_{\mathbf{x}}$ of a pixel \mathbf{x} becomes

$$\mathbb{E}(\ell_{\mathbf{x}}|\Theta^{(t-1)}, \mathcal{I}, \mathcal{M}) = P(\ell_{\mathbf{x}} = 1|\Theta^{(t-1)}, \mathcal{I}, \mathcal{M}) \quad (5.15)$$

$$= \alpha P(\Theta^{(t-1)}|\ell_{\mathbf{x}} = 1, \mathcal{I}, \mathcal{M}) P(\ell_{\mathbf{x}} = 1|\mathcal{I}) \quad (5.16)$$

using Bayes' rule, where $\alpha = 1/P(\Theta^{(t-1)}|\mathcal{I}, \mathcal{M})$, and \mathcal{M} is dropped in the last term of (5.16) since the segmentation of \mathcal{I} is independent of the 3D model. With Equation (5.16) we can assign the expectation of the segmentation to each pixel and thus get a *probability map* $\mathcal{I}_{\mathcal{L}^{(t)}}$ for $\mathcal{L}^{(t)}$. We can interpret this map as the probability for each pixel to be registered (has a correspondence) to the model, given that it is part of the segmented object *combined* with the a-priori probability to be part of the segmented object.

Note that we see the expectation as a probability where we joined the registration parameters from the last iteration and the a-priori knowledge of a pixel belonging to an object. We still keep the freedom to choose any kind of binarization technique, which we apply to the probability map.

We can give a generic algorithm for the segmentation-driven 2D-3D registration, which we will henceforth refer to as EBM algorithm as summarized in Algorithm 3.

Algorithm 3 EBM: Segmentation-driven 2D-3D registration

Given image \mathcal{I} , a model \mathcal{M} , initial estimates of parameters $\Theta^{(0)}$, and labelmap $\mathcal{L}^{(0)}$

$$\Theta^{(t-1)} \leftarrow \Theta^{(0)}$$

$$\mathcal{L}^{(t-1)} \leftarrow \mathcal{L}^{(0)}$$

while \neg converged **do**

E-step: Create probability map $\mathcal{I}_{\mathcal{L}^{(t)}}$: For each pixel \mathbf{x} with $\ell_{\mathbf{x}} = 1$ determine the probability for the new label using Equation (5.16). For each pixel \mathbf{x} with $\ell_{\mathbf{x}} = 0$ set the probability to zero.

B-step: Binarize $\mathcal{I}_{\mathcal{L}^{(t)}}$ to get $\mathcal{L}^{(t)}$.

M-step: Register \mathcal{M} to $\mathcal{L}^{(t)}$ starting from $\Theta^{(t-1)}$ to get $\Theta^{(t)}$

end while

Note that our method does not follow the strict formulation of the EM algorithm [37],

$$\Theta^{(t)} = \arg \max_{\Theta} \sum_{\mathcal{L}} P(\mathcal{L}|\Theta^{(t-1)}, \mathcal{I}, \mathcal{M})P(\mathcal{L}, \mathcal{I}, \mathcal{M}|\Theta). \quad (5.17)$$

In our algorithm, we directly calculate the expectation of the hidden variable \mathcal{L} , whereas EM calculates the expectation of the *probability* of the complete data $(\mathcal{L}, \mathcal{I}, \mathcal{M})$ given the incomplete data $(\mathcal{I}, \mathcal{M})$ and an estimate of Θ . Unlike EM, convergence is not proven for our approach. In our experiments, however, the algorithm always converged given suitable termination criteria.

5.4.2. The EBM Algorithm for Angiographic Registration

We can now apply the EBM algorithm to rigid CTA-to-DSA registration. Several steps of the algorithm are illustrated in Figure 5.7. Given a DSA image \mathcal{I} (Figure 5.7a) and the vasculature model \mathcal{M} (laid over the DSA in Figure 5.7f) of a CTA volume. The 3D point cloud that spatially describes \mathcal{M} , i.e. sampling points on vessel

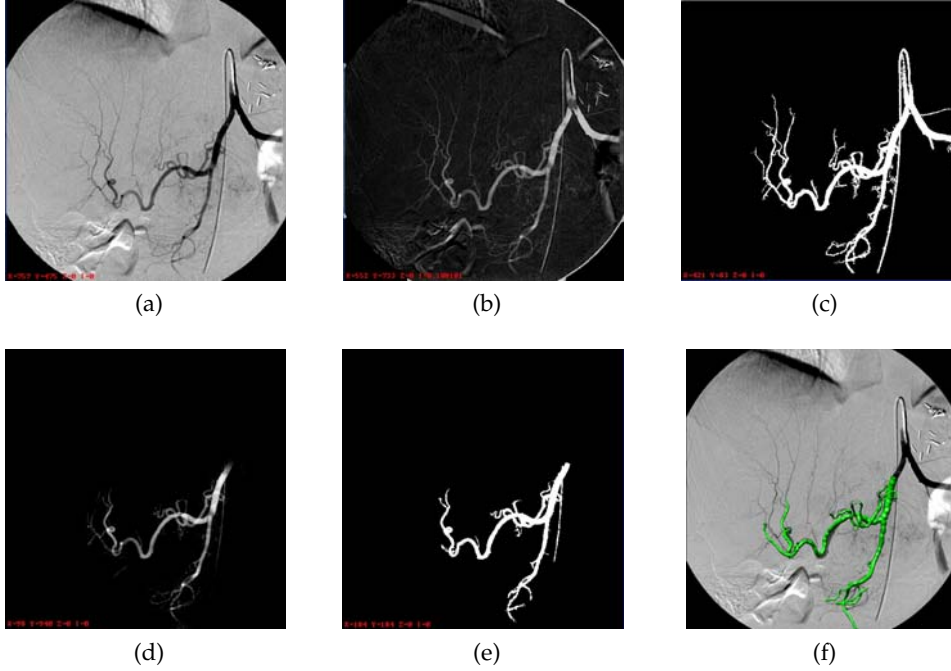


Figure 5.7.: Illustration of the segmentation-driven registration: (a) original DSA, (b) bothat filtered DSA, (c) initial segmentation (automatic seed point detection, region growing), (d) probability map penalizing non-corresponding but extracted features in 2D and 3D, (e) final segmentation after registration - increased feature similarity, (f) overlay of 3D vasculature and DSA

centerlines and bifurcation locations, is denoted by $\{\mathbf{V}_j\}$. We want to estimate the rigid-body transformation, i.e. our parameter set is $\Theta = \{\alpha, \beta, \gamma, t_x, t_y, t_z\}$. We consider all image intensities normalized to belong to the domain $[0; 1]$.

Image Preprocessing As initialization for the a-priori probability $P(\ell_x = 1 | \mathcal{I}_x)$ we choose a bothat filtered image whose contours are sharpened by histogram equalization (Figure 5.7b). We refer to this filtered image as \mathcal{I}^{BH} .

Mind that other probability images can be deduced, for instance by applying filters of Frangi *et al.* [47], Sato *et al.* [131], or Manniesing *et al.* [98]. However, we use the bothat filter due to its computational efficiency.

The initial ($\mathcal{L}^{(0)}$, see Figure 5.7c) as well as all subsequent segmentations of the DSA are computed using a region growing technique based on intensity thresholds as explained in 5.2.1. The seed points, however, are automatically detected using a derivative-mean filter defined by Can *et al.* [25] for vessel tracing. It detects pixels that are likely to lie on a vessel centerline by filter inspection in 12 directions and criteria evaluation. This method is very fast and yields decent candidate seeds. In order to start with a segmentation, we choose the intensity values for the region growing to be inside the interval $\mu_{seeds} \pm 2\sigma_{seeds}$, which are mean and standard deviation of

the intensity values of all detected seed points. We start the region growing from all detected seed points. Outliers are removed by choosing the largest connected region as the actual segmentation. From the segmentation we create a model of a 2D vessel centerline to be able to register it with the 3D model \mathcal{M} and deduce a diameter, which is used as σ in the E-step. The remaining steps of quantification and graph creation are performed as described in 5.2.2.

Initial Registration $\Theta^{(0)}$ is determined by combining information from the C-arm with an exhaustive feature search. This search is performed similar to the one explained in 5.3.1, but is not restricted to bifurcations, but is carried out on all nodes of the respective graphs.

Iteration We define the pixel error ε of a pixel \mathbf{x} similar to Equation 3.5 as

$$\varepsilon(\mathbf{x}) = d(\mathbf{x}, C(\mathbf{x}, \{f_{\mathbf{P}_\Theta}(\mathbf{V}_j)\}))^2 \quad (5.18)$$

where $d(\cdot, \cdot)$ determines the Euclidean distance of two vectors, $C(\mathbf{y}, \{\mathbf{z}_j\})$ determines the closest point of a point set $\{\mathbf{z}_j\}$ to a point \mathbf{y} , $\{\mathbf{V}_j\}$ are all points on the 3D centerline, and $f_{\mathbf{P}_\Theta}$ is the projection matrix (Equation (2.38)) with the current pose parameters Θ .

E-step: This step computes the probability map using the expectation value as defined in Equation (5.16). The probability that a vessel pixel is registered to the 3D model, $P(\Theta^{(t-1)} | \ell_{\mathbf{x}} = 1, \mathcal{I}, \mathcal{M})$, is defined via the pixel error (Equation (5.18)). If we allow a deviation proportional to the maximal width of a vessel in the 2D image, σ , and assume the error distribution to be Gaussian, we get

$$P(\Theta^{(t-1)} | \ell_{\mathbf{x}} = 1, \mathcal{I}, \mathcal{M}) = \frac{1}{\sigma\sqrt{2\pi}} e^{-\varepsilon(\mathbf{x})/\sigma^2} \quad (5.19)$$

The a-priori probability for a pixel \mathbf{x} to lie inside a vessel is defined by the image \mathcal{I}^{BH} as described above, i.e. $P(\ell_{\mathbf{x}} = 1 | \mathcal{I}) = \mathcal{I}^{BH}(\mathbf{x})$. Putting both terms together, we define the expectation value of a pixel label $\ell_{\mathbf{x}}$ as

$$\mathbb{E}(\ell_{\mathbf{x}} | \Theta^{(t-1)}, \mathcal{I}, \mathcal{M}) \propto e^{-\varepsilon(\mathbf{x})/\sigma^2} \cdot \mathcal{I}^{BH}(\mathbf{x}), \quad (5.20)$$

where we dropped α from eq. (5.16) since it just represents an isotropic scaling on pixel intensities of $\mathcal{I}_{\mathcal{L}^{(t)}}$. With Equation (5.20) we can compute a value for all pixels of the probability map $\mathcal{I}_{\mathcal{L}^{(t)}}$.

B-step: After building up the map (Figure 5.7d), we perform a new region growing (Figure 5.7e) and centerline extraction as described above to get a new 2D centerline.

M-step: The 2D-3D registration is computed by minimizing the pixel error ε , which is evaluated only on the 2D centerline points. If a projected centerline point $\mathbf{P}_\Theta \mathbf{V}_j$ already has a closest point, the one with the smaller error is chosen. Thus, we assure one-to-one correspondence of centerline features. The iteration of the registration is governed by a Downhill Simplex optimizer [123] minimizing the non-linear cost function $\sum_{\mathbf{x}} \varepsilon(\mathbf{x})$, where \mathbf{x} has a corresponding (closest) point in the 3D model \mathcal{M} .

We stop the algorithm if the absolute difference of the two labelmaps of current and last E-step, $\sum_{\mathbf{x}} |\mathcal{L}^{(t-1)}(\mathbf{x}) - \mathcal{L}^{(t)}(\mathbf{x})|$, is very small. We choose a threshold of 5% of the pixels in an image (size 1024^2), at which the difference of the labelmaps becomes visually insignificant.

5.4.3. Algorithm Evaluation

Creation of Reference Registration For testing the algorithm in a controlled environment we artificially created a DSA from intraoperative 3D data, which was acquired additional to the preoperative CTA. We assembled a simulated DSA from a background image and a 3D vasculature both acquired during the same intervention. The background image was created by subtraction of two fluoroscopic images in a different breathing state without contrast, see Figure 5.8a¹. On the same device (Siemens Axiom Artis fDA) that was used for DSA acquisition, we computed a 3D reconstruction of the patient anatomy in the intraoperative situation. This 3D image was segmented and processed to yield a 3D graph representation of the vessel system. Then, we aligned the 3D graph with the simulated DSA using the projection information of the device. We manually refined the computed pose such that the catheter lay inside the right vessel, accounting for breathing deformation.

Given this alignment, we projected the 3D vessel graph onto the background image. At each centerline location \mathbf{v} we drew a disk with the same size as the projected diameter. The intensity information for the pixels \mathbf{x}_i inside the disk was calculated proportional to the projected diameter d :

$$\mathcal{I}(\mathbf{x}_i) = c - \frac{1}{d}, \quad (5.21)$$

where c is an intensity constant. Thus, the smaller the vessel diameter, the higher the intensity value. This simulates the effect of contrast loss during propagation to distant (smaller) vessels. We applied an averaging smoothing filter to all disk pixels in order to get rid of intensity edges between adjacent disks. In order to account for vessel overlay (where the accumulating contrast makes vessels appear darker), we always used the minimal intensity of all calculated ones at an overlay point. Finally, we added Gaussian noise (standard deviation 0.05 on $[0; 1]$ intensities) to the vessel pixel intensities.

We assembled three test situations using the artificially generated DSA (see also Figure 5.8):

- *Rigid Test*: As 3D input graph we used the vascular graph with which the DSA was generated. Thus, a perfect overlay of all vessel structures can be achieved.
- *Outlier Test*: We manually removed some vessel segments of the 3D input graph of the rigid test such that the number of visible vessel segments roughly match

¹We are aware that new C-arm systems improve DSAs by non-rigid 2D-2D registration, which was left out in this simulation.

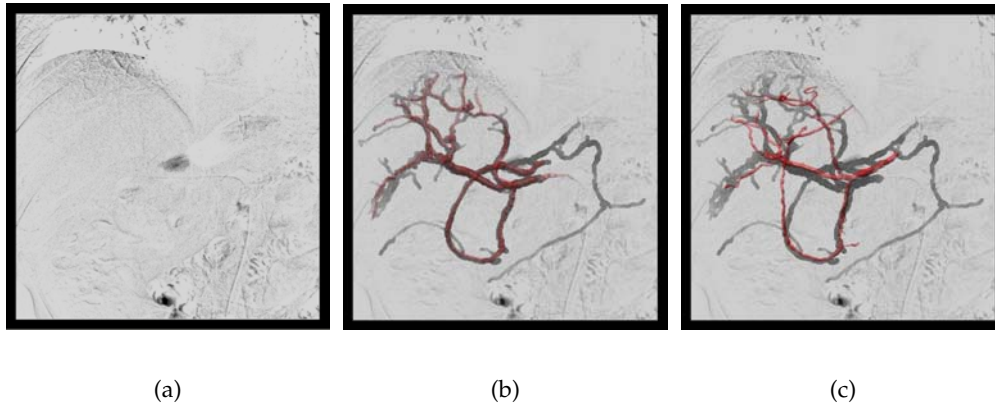


Figure 5.8.: Simulated DSA images. (a) shows the background image created from two fluoroscopic acquisitions in different breathing states. (b) shows an overlay of the 3D intraoperative vasculature after vessel segment removal (used for test “Outlier”). (c) shows the overlay of the preoperatively acquired CTA vasculature, which was used in test “Deformation”.

that of the graph extracted from the preoperative CTA. In this way, rigid alignment can still lead to a perfect overlay of the 3D vessels, but there are unmatched 2D vessel segments disturbing the registration (outliers). See Figure 5.8b for an overlay of the registered input 3D graph.

- *Deformation Test:* Here we did not use the intraoperative 3D graph for registration, but the preoperative graph extracted from CTA. In order to compute a reference registration, we manually determined corresponding bifurcation points in pre- and intraoperative 3D graph. Then, we used the method of Umeyama [147] to rigidly register two 3D point clouds and transformed the 3D CTA graph to the coordinate system of the intraoperative 3D graph where we generated the DSA from, see Figure 5.8c. While a ground truth registration was present in the former two test situations, this test compares against reference registration parameters determined by another algorithm. Since Umeyama [147] showed that his method minimizes the 3D Euclidean distance in a least-squares sense, this algorithm can be regarded as “gold standard” for our scenario.

For clinical testing, we acquired five patient data sets with different level of contrast propagation and deformation. Three of them are visualized in Figure 5.9 together with an overlay of the 3D CTA vasculature after registration. The reference registration was provided by experts together with a reference 2D segmentation. As can be assessed from Figures 5.9d, 5.9f, and 5.8c, large deformations can occur in the liver arterial system.

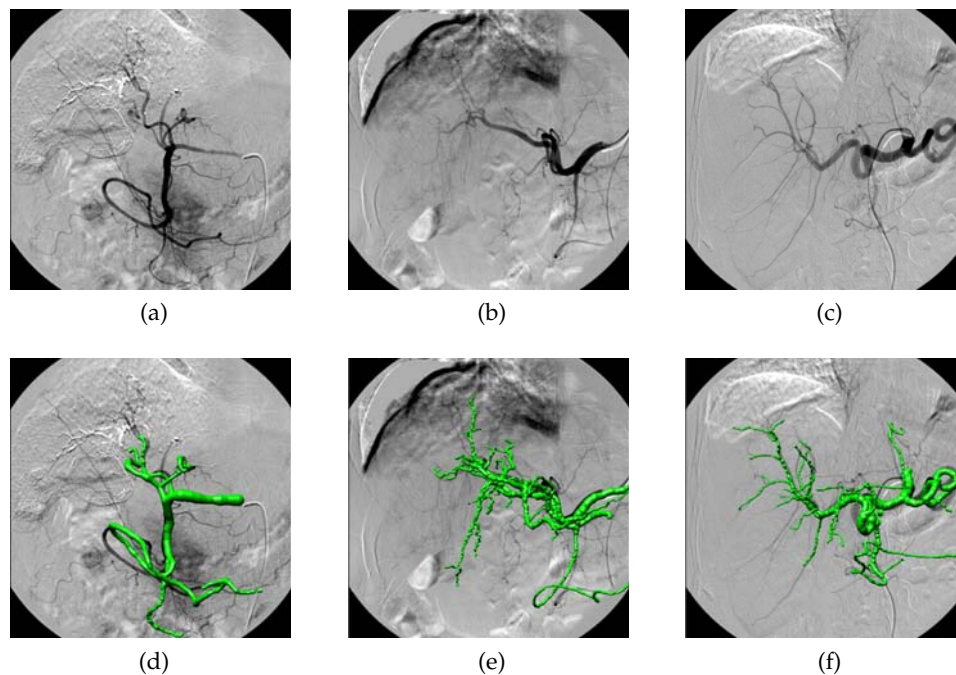


Figure 5.9.: Registration results on 3 data sets. 2D vessel trees (upper row) are different as are 3D vasculatures (laid over DSA, lower row). Figure 5.9e shows 3D vasculature with vessels that are not visible in 2D. Large deformations between 2D and 3D can be seen in the lower part of Figure 5.9d or 5.9e.

Accuracy and Robustness Accuracy and robustness was assessed in the same way as for the bifurcation-driven registration through RSME, standard deviation, and Monte Carlo studies (see 5.3.3). Random displacements were added to all 6 parameters, however, not only to 4. The range of error added to the single registration parameters was $\pm 5mm$, and $\pm 5^\circ$, respectively. For the simulation studies, we additionally tested a range of $\pm 10mm$ and $\pm 10^\circ$. As in 5.3.3 we invoked the registration procedures 200 times.

Additional to RMSE and standard deviation, we assessed mTRE and mPD as defined in Equations (2.40) and (2.42) in section 2.4.3, and computed their average value over the 200 Monte Carlo simulations. For the mTRE we defined points on a grid with an equal spacing of 16 mm over the whole input 3D image. We transformed them with the reference transformation \mathbf{T}_{gold} as well as with the transformation before \mathbf{T}_{bef} (for range assessment) and after \mathbf{T}_{reg} (for accuracy assessment) the registration. For assessing mPD, we projected the grid points with \mathbf{P}_{gold} , \mathbf{P}_{bef} , and \mathbf{P}_{reg} , respectively, and determined the pixel error multiplied with the pixel size in mm. Furthermore, since the structure of interest in angiographic registration are vessels, we evaluated mTRE and mPD on bifurcation points only. We did not evaluate the mRPD (Equation (2.42)) since it gives similar information as the mPD but with a smaller magnitude since the object is located between X-ray source and de-

Test	σ_{t_x}	σ_{t_y}	σ_{t_z}	σ_α	σ_β	σ_γ	ϵ_{t_x}	ϵ_{t_y}	ϵ_{t_z}	ϵ_α	ϵ_β	ϵ_γ
Rigid5	0.08	0.14	1.43	0.12	0.09	0.12	0.38	0.27	4.23	0.13	0.31	0.28
Rigid10	5.56	1.23	15.97	4.00	1.68	2.29	5.59	1.30	15.93	3.99	1.69	2.28
Outlier5	0.98	1.41	2.87	0.85	1.29	1.00	1.02	1.48	5.17	1.27	1.30	1.08
Outlier10	3.93	3.29	22.09	2.14	1.21	1.77	3.95	3.29	22.11	2.53	1.22	1.90
Deformation5	0.73	1.10	13.14	1.89	1.42	1.61	2.98	1.80	13.23	5.70	6.44	1.64
Deformation10	6.48	4.86	35.94	5.16	4.96	3.45	6.73	4.85	35.85	6.88	7.74	3.71

Table 5.3.: Results of standard deviations σ and RMS errors ϵ of translations (in mm) and rotations (in deg) of the simulated DSA images. Deviation and error in z -translation are not as significant as those in-plane, or in rotations

Test	mTRE	mTRE bif	mPD	mPD bif	range PD
Rigid5	4.03	3.80	1.13	0.50	5.02 - 17.32
Rigid10	6.97	6.51	3.70	2.74	10.06 - 34.31
Outlier5	5.22	5.37	2.88	2.47	
Outlier10	8.29	8.26	4.76	3.93	
Deformation5	16.45	13.13	14.09	7.24	
Deformation10	25.96	21.51	18.95	10.72	

Table 5.4.: mTRE and mPD for the EBM algorithm of simulated DSA images. Tests in the range of ± 5 are in the upper rows, tests in the range of ± 10 in the lower rows. Number of grid points for mTRE and mPD was 2352. Number of bifurcation points for mTRE bif and mPD bif was 125/40/39. mTRE ranges were 4 – 22 mm (for the ± 5 displacements) and 8 – 28 mm (for the ± 10 displacements). All values are given in mm.

sector. Since we are interested in a visually observable error, the mPD which yields the displacement in the image plane, was favored.

Algorithm Comparison On the clinical data sets, we tested the performance of the algorithm against our implementation of Jomier’s method and the bifurcation-driven registration. An expert performed manual 2D segmentations of the DSAs for the bifurcation-driven method.

For both methods we assessed RSME, standard deviation, as well as mTRE and mPD for equally spaced grid and bifurcation points. The mTRE and mPD values are averaged over all 200 registrations. We did not compare the performance of the algorithms on the simulated data.

Results Tables 5.3 and 5.4 show the errors computed from the Monte Carlo studies of the simulation tests.

Two tendencies can be observed. First, the error increases when using less vessels for alignment. Moreover, the error is observed to be rather high when deformation is hampering the registration².

²Mind that the deformation in this example is unusually high.

#		σ_{t_x}	σ_{t_y}	σ_{t_z}	σ_{α}	σ_{β}	σ_{γ}	ϵ_{t_x}	ϵ_{t_y}	ϵ_{t_z}	ϵ_{α}	ϵ_{β}	ϵ_{γ}
1	Jomier	0.76	1.80	4.66	3.48	3.17	1.60	0.78	2.21	5.30	4.75	3.60	1.66
	Bif	0.20	0.06	3.43	0.08	1.89	0.11	0.34	0.23	6.58	0.22	4.41	0.38
	EBM	0.54	2.68	34.63	3.79	1.88	1.25	0.54	2.70	36.12	3.79	1.97	1.25
2	Jomier	0.74	0.93	5.06	4.84	3.18	0.58	0.78	3.46	5.38	8.33	3.18	0.78
	Bif	0.16	1.33	4.52	4.80	2.59	1.27	1.24	1.49	28.48	5.28	3.85	2.33
	EBM	0.04	0.16	1.99	0.45	0.18	0.04	0.07	0.25	3.73	0.72	0.35	0.04
3	Jomier	3.34	2.03	7.39	4.43	4.37	2.04	4.68	2.96	7.43	5.62	4.39	2.07
	Bif	2.32	4.56	43.72	3.84	3.98	4.78	6.72	6.21	62.07	5.19	11.58	4.87
	EBM	3.55	1.53	24.11	7.47	3.33	4.62	3.54	1.54	24.36	7.49	3.33	4.62
4	Jomier	22.45	6.65	13.73	7.74	24.64	9.15	23.18	6.84	13.81	8.40	25.41	9.16
	Bif	6.30	0.89	55.10	4.55	6.82	4.09	9.05	2.02	70.69	7.54	14.73	4.99
	EBM	0.95	0.18	9.41	0.29	1.96	0.10	1.09	0.19	13.04	0.36	2.62	0.10
5	Jomier	26.35	16.37	10.34	7.15	13.60	5.81	26.66	16.37	10.87	7.25	18.63	6.07
	Bif	20.65	1.82	148.41	14.88	12.29	15.10	52.74	3.39	422.62	28.76	16.95	24.40
	EBM	1.22	0.74	16.83	3.05	2.07	0.67	1.41	0.74	20.19	3.05	2.44	0.76
Avg.	Jomier	10.73	5.60	8.23	5.53	9.79	3.83	11.21	6.37	8.56	6.87	11.04	3.95
	Bif	5.93	1.70	51.04	5.63	5.5	5.07	14.02	2.67	118.09	9.39	10.30	7.39
	EBM	1.26	1.06	17.39	3.01	1.88	1.34	1.33	1.08	19.49	3.08	2.14	1.35

Table 5.5.: Results of standard deviations σ and RMS errors ϵ of translations (in mm) and rotations (in deg). Deviation and error in z -translation are not as significant as those in-plane, or in rotations

Second, the error in projection direction (ϵ_{t_z}) is three to six times higher than the in-plane error. This is quite common for 2D-3D registration based on one view since a change of out-of-plane parameters does not alter the projection as much as a change of in-plane parameters. This phenomenon can also be observed in the mTRE and mPD values.

Table 5.5 shows RMSE and standard deviation values for the five patient data sets.

It can be seen that error and deviation in z -translation is sometimes outperformed by the other two methods, however, the more important in-plane translation and rotations have less error in our method. The large errors of Jomier's and the bifurcation-driven method in the last two data sets can be explained with a "subset" property. In the first three data sets the 3D vasculature is a "subset" of the 2D vasculature, whereas in the last two data sets this property is not fulfilled, i.e. the 3D vasculature shows branches that are not visible in 2D. The results show that our method is more robust with respect to variability in both dimensions.

Table 5.6 shows mTRE and mPD for grid points and bifurcation points of the patient data, again averaged over 200 registration procedures. The different ranges of the error in the five data sets are due to the different 3D image sizes. The range of the random displacements in all parameters, $\pm 5mm, \pm 5^\circ$, is equal throughout the studies. Especially the mPD error shows the accurate alignment by EBM of vessel structures when projected to the image plane.

Runtime The number of iterations of our algorithm usually lies between 2 and 5. The runtime (analyzed on a Intel Core2Duo 2.6 GHz machine) splits into (both-) filtering (28.5 sec), seed point extraction (1.0 sec), region growing (0.3 sec), centerline

Data	Method	mTRE	mTRE bif	mPD	mPD bif	range TRE	range PD
1	Jomier	14.49	6.57	15.39	4.52	4.99 - 19.21	6.32 - 25.29
	Bif	10.56	9.05	6.91	2.10		
	EBM	10.13	9.67	5.23	1.82		
2	Jomier	15.44	7.29	14.77	3.59	4.57 - 17.16	5.04 - 19.13
	Bif	30.31	27.27	11.44	2.87		
	EBM	3.65	3.15	1.44	0.21		
3	Jomier	49.43	40.81	58.33	50.65	5.57 - 21.03	5.64 - 22.02
	Bif	62.28	60.35	30.65	10.15		
	EBM	11.26	9.49	5.63	2.13		
4	Jomier	21.63	11.98	26.76	14.67	5.01 - 18.78	5.39 - 20.16
	Bif	59.83	52.23	29.76	8.37		
	EBM	9.93	9.49	3.71	1.08		
5	Jomier	23.32	14.88	32.66	32.66	4.72 - 21.80	5.57 - 27.86
	Bif	404.35	421.99	83.77	51.38		
	EBM	14.89	12.15	7.60	1.99		

Table 5.6.: mTRE and mPD for algorithm comparison of Jomier’s method, the bifurcation-driven algorithm described in 5.3, and the EBM algorithm. Number of grid points for mTRE and mPD was between 3000 and 9000. Number of bifurcation points for mTRE bif and mPD bif was between 12 and 98. All values are given in mm.

extraction (2.7 sec), exhaustive initialization (34.9 sec), iteration (including region growing, centerline extraction, and pose optimization) (12.9 sec), where all runtimes have been averaged over the 5 patient data sets and the iteration runtime over the number of iterations. Altogether, applying the registration takes 1.5 - 2 min. The two critical stages are filtering and exhaustive initialization - both can be further optimized numerically.

5.4.4. Discussion

We have developed a method for 2D-3D registration of angiographic data. Our emphasis lies on a fully automatic registration once the interventionalist starts the treatment. We believe that a 2D segmentation can yield a more robust (feature-based) registration with high capture range. Motivated by an ML formulation of a combined segmentation/registration, we derived a generic method for estimating the 2D labelmap and the registration parameters iteratively linked by a common probability map.

In this probabilistic framework, we keep the freedom to choose any segmentation or registration technique. Mind that the estimation process of the M-step (section 5.4.2) is only an approximation to an ML estimate, as required by Equation (5.13), but yields satisfactory results. Experiments with a real ML estimator for 2D-3D curve registration, a 2D-3D ICP algorithm as well as the Iterative Inverse Perspective (IIP) algorithm as proposed by Wunsch and Hirzinger [157], did not provide the desired convergence to the right solution. We believe that the number of outliers was still too large for an ICP algorithm to succeed making a preliminary computation of putative matches for correspondence necessary. This step, however, is not required for our

proposed method.

Unlike other approaches, we keep user interaction low while high capture range and robustness against vessel variability and deformation are maintained. With the segmentation-driven registration, we create a common feature space and thus one-to-one correspondence of vessel features.

Compared to the bifurcation-driven registration and Jomier's method, the segmentation-driven registration is able to recover the correct pose more often even if high deformation and outliers are present. On the patient data sets, a registration accuracy of $mPD = 1.45$ mm can be observed in average, comparable to the error achieved by other algorithms in this field applied to *rigid* vasculature. However, in extreme cases where non-rigid patient movement deforms vessels vastly, the algorithm is not converging to the right solution when started far from the optimum, as has been shown in the simulation data set created from 3D pre- and intraoperative images.

We also want to emphasize on the evaluation of the different error measures that are common for accuracy assessment in 2D-3D registration. We believe that an analysis of RMS errors together with standard deviations of all 6 parameters is crucial in this context. If the center of rotation is chosen carefully, they yield comparable results to $mTRE$ and mPD as proposed by van de Kraats *et al.* [148]. These values, however, do not offer the same amount of information on the error as the RMSE. Thus, if the transformation model contains a finite and small number of parameters as in the rigid case, parameter error analysis should be provided for 2D-3D registration evaluation protocols, too.

6. Deformable 2D-3D Registration of Angiographic Images

In the previous parts of the thesis, methods for 2D-3D alignment of vascular images have been discussed that use a rigid transformation model discarding local motion. The algorithms are robust against deformation changes of vessel structures but do not solve for these changes, leaving a considerable amount of misalignment, which can be, as reported for liver, up to 3 cm [125].

These misalignments cause errors in image fusion, i.e. 3D roadmap vessels cannot be thoroughly laid over the current 2D vasculature, or catheter backprojection might miss the right vessel hampering a 3D visualization of the intraoperative situation.

In order to overcome the shortcomings of the rigid approach, we propose a method for computing a meaningful deformation of a 3D structure from a single 2D projection. The method solves the registration problem with the minimization of an energy consisting of a difference measure and regularization terms, which incorporate the a priori knowledge about the problem, see Figure 6.1.

The difference term used in this approach penalizes the distance between the projection of 3D points from the input vasculature, represented as nodes of a centerline graph, and the corresponding points from the 2D projection image (Figure 6.3).

Minimizing only the difference term results in what we refer to as the *Naive approach*, which is not able of recovering the deformation in the projection direction and thus leads to unnatural results. In order to be able to compute the 3D displacement, additionally to the difference, we employ a combination of two regularization terms, which model assumptions about vessel structures and thus yield realistic deformations.

The first term describes the assumption that the length of vessels does not change heavily inside the human body and penalizes large changes of the vessel length. This term is important since it presents constraints in 3D space and thus reduces the number of solutions for one node from infinite to two along the projection ray, if one of the neighbors is assumed fixed (Figure 6.2). Also, in our experiments the minimization of this term results in the nearest solution to the initial position of the respective point. Figure 6.3 illustrates the idea of using the difference term together with length preservation.

However, for real graphs with many nodes and large deformations the length preservation term has the drawback that the behavior is too local. Although the length preservation itself is successful, in these cases the property that the nearest solution to the initial position is computed introduces unnatural bends in the vessels, thus leading to unwanted results, compare Figure 6.4. In order to counteract this effect, we impose a smoothness condition on the resulting displacement field. This is done by employing one of two standard regularization terms, diffusion [154],

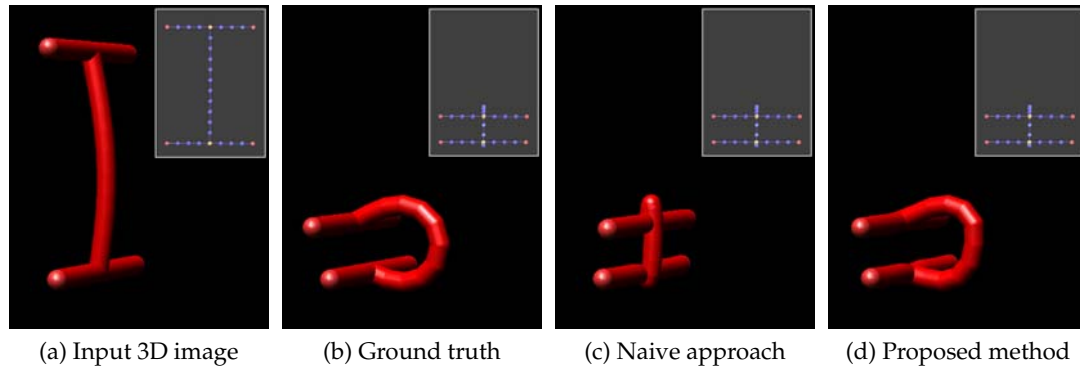


Figure 6.1.: Visualization of the method results on a simple synthetic example, with the window-in-window presenting the 2D projection of the respective 3D structure. **(a)** is the input 3D graph to be deformed while **(b)** shows a graph, which was used to generate the input 2D projection image. Hence, **(b)** presents the ground truth for the deformation of **(a)**. The camera is positioned on the right side of the images, such that the shape change in ray direction is not observable from the 2D projection image. **(c)** With the naive approach using only the distance measure from a single projection, it is not possible to recover the full 3D deformation since there are no constraints along the projection rays. **(d)** Employing the length preservation and diffusion regularization terms present additional constraints and thus allows for correct deformation also in the direction along the projection rays.

or bending energy [128].

Usually, these regularization terms are equipped with a boundary condition (e.g. Dirichlet, where the boundary values are fixed) which restricts the null-space of the terms. Fixing certain displacement values would require to have at least one vessel point for which the position is known. However, selecting such a 3D point in a deforming volume would present a very difficult - if not impossible - task. Thus, we replace the boundary condition by the soft constraint of position retention, which can easily be integrated into the optimization procedure.

So in summary, our method enables meaningful 3D deformations of 3D vessel structures based on a single 2D projection of the same structure. To the best of our knowledge this is the first time that this problem is addressed in the field of medical image processing.

Related Work In the robotics and graphic community, computing the 3D pose of a model from a 2D image is regarded as an inverse kinematics problem (see e.g. Grochow *et al.* [56] and references therein), which is somewhat related to our topic. However, the model which is used in these approaches often just has a very limited number of degrees of freedom (DOF) unlike our model, where each feature point introduces 3 DOF.

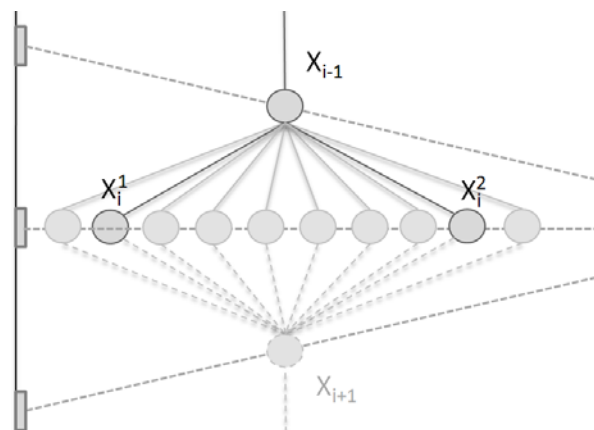


Figure 6.2.: Illustrates the reduction of admissible solutions for one node along the projection ray, by using length preservation. For the fixed node \mathbf{X}_{i-1} , the position of the node \mathbf{X}_i is constrained to two possible solutions, \mathbf{X}_i^1 and \mathbf{X}_i^2 , if the distance between \mathbf{X}_{i-1} and \mathbf{X}_i is assumed constant. Without the length constraint, every position along the ray presents a solution, some of which are visualized above.

6.1. Method

The basic idea of the proposed method is to use a difference term and supplement it by regularization terms which incorporate a priori knowledge about the problem and thus impose constraints along the projection rays, which are needed in order to render the problem well-posed. Having modeled the problem this way, the solution is computed by using an optimization method of choice. Since the focus of this work is on the modeling part, we use the standard gradient descent optimization scheme.¹

In the following, we first briefly describe the setting for the algorithm and the performed pre-processing steps. We go on by presenting notation and introducing structures we use. Then we define the model and in the following subsections we present the single components of the energy function to be optimized.

6.1.1. Setting and Preprocessing

As input for our method we use an extracted model of 2D and 3D vasculature, as well as a feature-based rigid pre-alignment in a calibrated setting² yielding a projection matrix and correspondence information between 2D and 3D feature points. All of these steps have been presented in chapter 5. A graph model is created 3D from a region growing step yielding vessel segmentations, followed by topological thinning and bifurcation detection as described in 5.2. A rigid 2D-3D registration is

¹However, any other standard gradient-based approach, such as e.g. Levenberg-Marquardt [99], can be employed.

²Meaning that intrinsic parameters of the intraoperative imaging device are given. Also, image distortion can be assumed to be absent due to flat-panel detector technology.

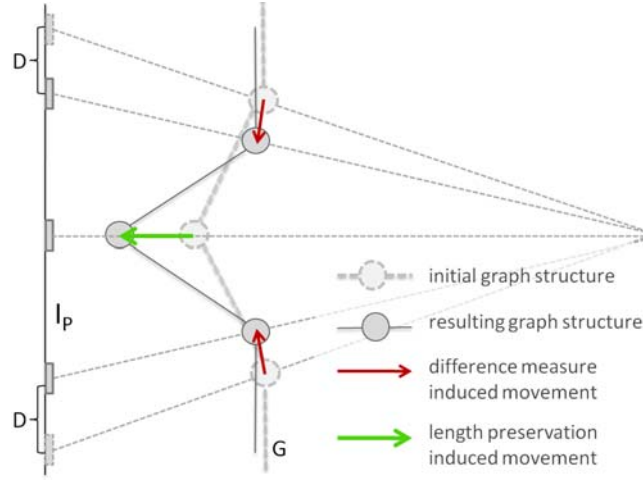


Figure 6.3.: 2D illustration of the effect of the difference measure and the length preservation term on the motion of the vessel structure. The difference term D measures the distance in the 2D projection image I_p . The length preservation penalizes the change of length of the 3D graph G .

computed by using the segmentation-driven 2D-3D registration from 5.4 solving for both a projection matrix and correspondences of centerline points. If corresponding information is not available at each centerline point, a closest point operator can be incorporated after the rigid registration to assign one-to-one correspondences to all curve points. If ambiguities arise in this assignment due to projection overlay of vessel structures, these features can be left out of the correspondence set, which does not influence the proposed method.

6.1.2. Preliminaries and Notation

As described in 5.2.3 we model vessel structures as graphs $G^d = (V^d, E^d)$. This method uses the sampling nodes \mathbf{X}, \mathbf{x} of 3D and 2D graphs for alignment. The correspondences between the 3D and 2D points are represented by $C \subset V^3 \times V^2$. Moreover, the inherent property of each sampling node having a left and right neighbor is incorporated to reduce the set of admissible transformations.

The deformation function is encoded by a set of 3D displacement vectors $\varphi \in \mathbb{R}^{3 \times n}$ centered in the n graph nodes. The displacement at the i -th node \mathbf{X}_i is denoted by φ_i , such that the final position of the node is $\mathbf{Y}_i = \mathbf{X}_i + \varphi_i$.

We also employ a dense version of the displacement function, which we denote by $\tilde{\varphi}$. We obtain $\tilde{\varphi}$ from φ by interpolation using Thin-Plate Splines (TPS) [152], see Appendix B. We choose a TPS since it has global support yielding a dense displacement field from a set of arbitrarily distributed control points. We use the dense displacement field for assigning displacement values to nodes for which no displacement

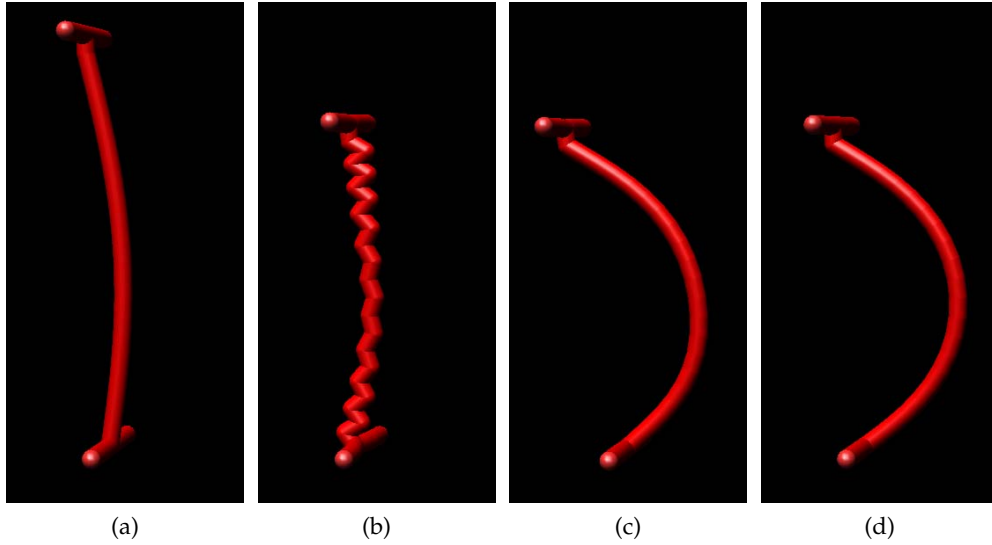


Figure 6.4.: Demonstrates the effect of joint usage of the length preservation and the diffusion regularization term. **(a)** Input 3D image. **(b)** Result with Length Preservation. **(c)** Result with Length Preservation and Diffusion Regularization clearly produces a more natural result. **(d)** Ground truth.

vectors are defined.³

For projections we use a standard pinhole camera model with the principal ray in the direction of the positive Z-axis as presented in 2.4.

6.1.3. The Model

The deformable registration process is now described as a minimization of the energy function \mathcal{E} with respect to the displacements φ of the vessel nodes in order to get the estimate φ' of φ , that is

$$\varphi' = \arg \min_{\varphi} \mathcal{E} , \quad (6.1)$$

with the energy function

$$\mathcal{E} = \mathcal{D} + \alpha \mathcal{S}_L + \beta \mathcal{S}_S + \gamma \mathcal{S}_P , \quad (6.2)$$

where the energy $\mathcal{E} : (G^3, G^2, C, \varphi) \mapsto y \in \mathbb{R}$ consists of a difference term $\mathcal{D} : (G^3, G^2, C, \varphi) \mapsto y \in \mathbb{R}$ and regularization terms $\mathcal{S}_L : (G^3, \varphi) \mapsto y \in \mathbb{R}$ for length

³In order to simplify the implementation, correspondences are computed only for sampling nodes, and thus also the energies are only evaluated there. This technical detail is due to the need to consider predecessor and successor nodes in some parts of the algorithm. In addition, omitting the bifurcation nodes, which often have more than only two neighboring nodes, facilitates the implementation.

preservation of the vessel segments, $\mathcal{S}_S : \varphi \mapsto y \in \mathbb{R}$ for smoothness of the displacement field, and the term $\mathcal{S}_P : \varphi \mapsto y \in \mathbb{R}$ for retention of initial positions of graph points, which replaces the standard boundary condition. For brevity, we will drop the function arguments in the remainder of the paper. The positive scalars α , β and γ control the influence of the respective terms.

In the following, we present the energy terms from Equation (6.2). We also give the respective derivatives which are used in the gradient descent optimization scheme.

6.1.4. Difference Measure

The difference measure \mathcal{D} which drives the registration process penalizes the distance between the projection of 3D points from the input graph and the corresponding 2D points from the input projection image.

Given point correspondences C with a single correspondence $C_i = (\mathbf{X}_i, \mathbf{x}_i)$ and a projection function $f : \mathbb{R}^3 \rightarrow \mathbb{R}^2$, we can define the distance measure

$$\mathcal{D} = \frac{1}{n} \sum_{i=1}^n \|\mathbf{x}_i - f_{\mathbf{P}}(\mathbf{X}_i + \varphi_i)\|^2 . \quad (6.3)$$

Here, $f_{\mathbf{P}} : \mathbb{R}^3 \rightarrow \mathbb{R}^2$ is a projection function as already defined in Equation (2.38):

$$f_{\mathbf{P}}(\mathbf{X}) = (\mathbf{p}_1^\top \hat{\mathbf{X}} / \mathbf{p}_3^\top \hat{\mathbf{X}}, \mathbf{p}_2^\top \hat{\mathbf{X}} / \mathbf{p}_3^\top \hat{\mathbf{X}})^\top , \quad (6.4)$$

where \mathbf{p}_1^\top , \mathbf{p}_2^\top and \mathbf{p}_3^\top constitute the row vectors of the projection matrix $\mathbf{P} \in \mathbb{R}^{3 \times 4}$, and $\hat{\mathbf{X}} = [\mathbf{X}^\top, 1]^\top$ is the homogeneous 4-vector of the 3D point \mathbf{X} .

For the minimization according to the model (6.2), the derivative of \mathcal{D} with respect to φ_i is needed. By using $\mathbf{Y}_i = \mathbf{X}_i + \varphi_i$ the gradient is given by

$$\frac{\partial \mathcal{D}}{\partial \varphi_i} = -\frac{2}{n} (\mathbf{x}_i - f_{\mathbf{P}}(\mathbf{Y}_i))^\top \mathbf{J}_i , \quad (6.5)$$

where $\mathbf{J}_i \in \mathbb{R}^{2 \times 3}$ is the Jacobian of $f_{\mathbf{P}}$ with respect to φ_i , given by

$$\frac{1}{(\mathbf{p}_3^\top \hat{\mathbf{Y}}_i)^2} \begin{bmatrix} p_{11}\mathbf{p}_3^\top \hat{\mathbf{Y}}_i - p_{31}\mathbf{p}_1^\top \hat{\mathbf{Y}}_i & p_{21}\mathbf{p}_3^\top \hat{\mathbf{Y}}_i - p_{31}\mathbf{p}_2^\top \hat{\mathbf{Y}}_i \\ p_{12}\mathbf{p}_3^\top \hat{\mathbf{Y}}_i - p_{32}\mathbf{p}_1^\top \hat{\mathbf{Y}}_i & p_{22}\mathbf{p}_3^\top \hat{\mathbf{Y}}_i - p_{32}\mathbf{p}_2^\top \hat{\mathbf{Y}}_i \\ p_{13}\mathbf{p}_3^\top \hat{\mathbf{Y}}_i - p_{33}\mathbf{p}_1^\top \hat{\mathbf{Y}}_i & p_{23}\mathbf{p}_3^\top \hat{\mathbf{Y}}_i - p_{33}\mathbf{p}_2^\top \hat{\mathbf{Y}}_i \end{bmatrix}^\top \quad (6.6)$$

where p_{ij} denote the entries of the projection matrix.

6.1.5. Length Preservation Constraint

Since vessel structures are in general enclosed by soft tissue, for example inside liver, and breathing motion is limited to a certain magnitude, the length change of the vessels is limited. We model this observation by imposing a soft length preservation constraint on the single vessel segments. Thus, we do not impose constant lengths, which would be a too restrictive and unnatural assumption in the given setting.

Since the vessel length is defined in 3D space, this constraint is able to induce a deformation orthogonal to projection rays, compare Figure 6.3.

We define the terms $d_i^-(\varphi)$ and $d_i^+(\varphi)$, which measure the length of the edges connected to the sampling node \mathbf{X}_i for a given set of displacements φ by

$$d_i^-(\varphi) = \|\mathbf{Y}_i - \mathbf{Y}_{i-1}\|^2, \text{ and} \quad (6.7)$$

$$d_i^+(\varphi) = \|\mathbf{Y}_i - \mathbf{Y}_{i+1}\|^2, \quad (6.8)$$

where we once again set $\mathbf{Y}_i = \mathbf{X}_i + \varphi_i$, compare also Figure 5.3. Please note that the initial length of the edges connected to \mathbf{X}_i is given by $d_i^-(\mathbf{0})$ and $d_i^+(\mathbf{0})$ where $\mathbf{0}$ is the zero displacement field.

Now we can define a length preserving cost function as

$$\mathcal{S}_L = \frac{1}{n} \sum_{i=1}^n \left| d_i^-(\mathbf{0}) - d_i^-(\varphi) \right|^2 + \left| d_i^+(\mathbf{0}) - d_i^+(\varphi) \right|^2, \quad (6.9)$$

which penalizes the deviation from the initial length of the two edges which are directly influenced by the i -th node.

The derivative of \mathcal{S}_L with respect to φ_i reads

$$\frac{\partial \mathcal{S}_L}{\partial \varphi_i} = \frac{-8}{n} \left[w_i^-(\mathbf{Y}_i - \mathbf{Y}_{i-1}) + w_i^+(\mathbf{Y}_i - \mathbf{Y}_{i+1}) \right]^\top, \quad (6.10)$$

with $w_i^- = d_i^-(\mathbf{0}) - d_i^-(\varphi)$ and $w_i^+ = d_i^+(\mathbf{0}) - d_i^+(\varphi)$.

The evaluation of the derivative of the length preservation term is performed independently on single vessel segments Π , since for the computation, ordered correspondences and nodes with a left and right neighbor each are needed.

6.1.6. Diffusion Regularization and Bending Energy

The so-called diffusion regularization term is often used in intensity-based registration (compare e.g. [154]) in order to impose a smoothness constraint onto the displacement field. The energy function is defined as

$$\mathcal{S}_D = \frac{1}{n} \sum_{i=1}^n \left\| \nabla \varphi_i^{(x_1)} \right\|^2 + \left\| \nabla \varphi_i^{(x_2)} \right\|^2 + \left\| \nabla \varphi_i^{(x_3)} \right\|^2, \quad (6.11)$$

where $\nabla \varphi^{(d)}$ is defined by using the dense version of the displacement field $\tilde{\varphi}$, which is computed using the 3D Thin-Plate Spline. Here the standard central difference approximation scheme with an appropriate grid spacing h is used.

The derivative of \mathcal{S}_D is

$$\frac{\partial \mathcal{S}_D}{\partial \varphi_i} = \frac{2}{n} \Delta \varphi_i = \frac{2}{n} \left[\Delta \varphi_i^{(x_1)}, \Delta \varphi_i^{(x_2)}, \Delta \varphi_i^{(x_3)} \right], \quad (6.12)$$

where Δ is the Laplace operator with $\Delta \varphi_i^{(d)} = \partial_{xx} \varphi_i^{(d)} + \partial_{yy} \varphi_i^{(d)} + \partial_{zz} \varphi_i^{(d)}$. The Laplace operator is also evaluated by using the dense version of the displacement field.

A regularization via bending energy minimization has been proposed in registration algorithms to allow for affine transformations (bending energy, unlike diffusion, is insensitive against affine transformations, see 2.3.2). We want to explore the impact of this affine insensitivity even after rigid 2D-3D registration. The bending energy term is defined as

$$\mathcal{S}_C = \frac{1}{n} \sum_{i=1}^n \sum_{j=1}^d \sum_{k=1}^d \left| \frac{\partial^2 \varphi_i^{(x_1)}}{\partial x_j \partial x_k} \right|^2 + \left| \frac{\partial^2 \varphi_i^{(x_2)}}{\partial x_j \partial x_k} \right|^2 + \left| \frac{\partial^2 \varphi_i^{(x_3)}}{\partial x_j \partial x_k} \right|^2, \quad (6.13)$$

and its derivative is given by

$$\frac{\partial \mathcal{S}_C}{\partial \varphi_i} = \frac{2}{n} \mathbf{G}^\top \mathbf{G} \varphi_i = \frac{2}{n} \left[\mathbf{G}^\top \mathbf{G} \varphi_i^{(x_1)}, \mathbf{G}^\top \mathbf{G} \varphi_i^{(x_2)}, \mathbf{G}^\top \mathbf{G} \varphi_i^{(x_3)} \right], \quad (6.14)$$

where \mathbf{G} is the operator for the computation of the second derivatives, i.e.

$$\mathbf{G} \varphi_i = \left[\frac{\partial^2}{\partial x_j \partial x_k} \varphi_i \right]_{j=1, \dots, 3, k=1, \dots, 3}. \quad (6.15)$$

Either \mathcal{S}_D or \mathcal{S}_C is used as smoothing term \mathcal{S}_S in the energy formulation 6.2.

The evaluation of the TPS for computing the gradient and the Laplacian does not present a large overhead, since the TPS coefficients are already computed in every iteration in order to transform nodes for which no correspondences are defined.

6.1.7. Position Retention Constraint

Instead of using a boundary condition for our problem, such as fixed values for the displacement at certain nodes, we use a soft-constraint which implies that all points should retain their initial position. The advantage of this approach is that it involves no hard constraints, which would possibly require user interaction. The weighting γ for the position retention constraint is chosen very low relative to the coefficients for the other terms, such that only the motion along the projection rays is effectively constrained, which is not or hardly constrained by the other terms.

The energy term is defined to minimize the distance between initial and final position as

$$\mathcal{S}_P = \frac{1}{n} \sum_{i=1}^n \|\mathbf{Y}_i - \mathbf{X}_i\|^2 = \frac{1}{n} \sum_{i=1}^n \|\varphi_i\|^2, \quad (6.16)$$

and the trivial derivative is

$$\frac{\partial \mathcal{S}_P}{\partial \varphi_i} = \frac{2}{n} \varphi_i. \quad (6.17)$$

6.1.8. Optimization Scheme

By using all components of the cost function \mathcal{E} together with their gradients, and the step size μ , we can give an algorithm based on gradient descent optimization, compare Algorithm 4.

Algorithm 4 Deformable 2D-3D Registration with Additional Constraints

Given the input graphs G^3 and G^2 , ordered point correspondences $C_i = (\mathbf{X}_i, \mathbf{x}_i)$, and a projection matrix \mathbf{P} ,

repeat

 calculate $\nabla\mathcal{E} = \nabla\mathcal{D} + \alpha\nabla\mathcal{S}_L + \beta\nabla\mathcal{S}_S + \gamma\nabla\mathcal{S}_P$

 update displacements $\varphi = \varphi - \mu\nabla\mathcal{E}/\|\nabla\mathcal{E}\|$

 update the 3D TPS and deform whole graph

until $\|\nabla\mathcal{E}\| < \varepsilon$

Figure 6.5 shows an iteration of the 2D-3D registration algorithm on a synthetic example. Note that the upper and lower part of the “C” shape are bent in the wrong direction after 85 iterations (Figure 6.5c), but the algorithm recovers from this situation as can be observed in Figures 6.5d and 6.5e.

6.2. Results and Evaluation

In order to validate our results, besides visual inspection, we compute two different quantitative error measures.

The first is the 3D Euclidean distance between the nodes of the ground truth (GT) structure and a given graph.

Since this first measure does not take topology into account we also introduce a second measure, which does not penalize the position, but only evaluates the shape. At every node, the angle between the two adjacent edges is computed.

We perform the tests on synthetic graphs with artificial deformations in order to test various aspects of the method. To demonstrate the applicability for real applications, we apply the tests to real vessels segmented from angiographic images, deformed by both, artificial and natural deformation fields. Moreover, we conduct a clinical test on real data sets.

The error evaluation is summed up in Table 6.1. The respective visualization of the results for synthetic data sets is presented in Figure 6.8.

6.2.1. Parameter Values and Smoothness Term

Empirically we have found out that a value of $\alpha = 40$ yields good results for all input data sets. For the smoothness term, $\beta = 20$ is a good trade-off between smoothness of deformation field and length preservation if the diffusion regularization is used. The regularization by bending energy usually works well if we choose $\beta = 10$. For these values, diffusion and bending energy regularization yield visually similar results and a similar quantitative error for all studies.

γ is usually chosen to be 100 times smaller than α, β . $\gamma = 0.1$ was a good choice for all experiments.

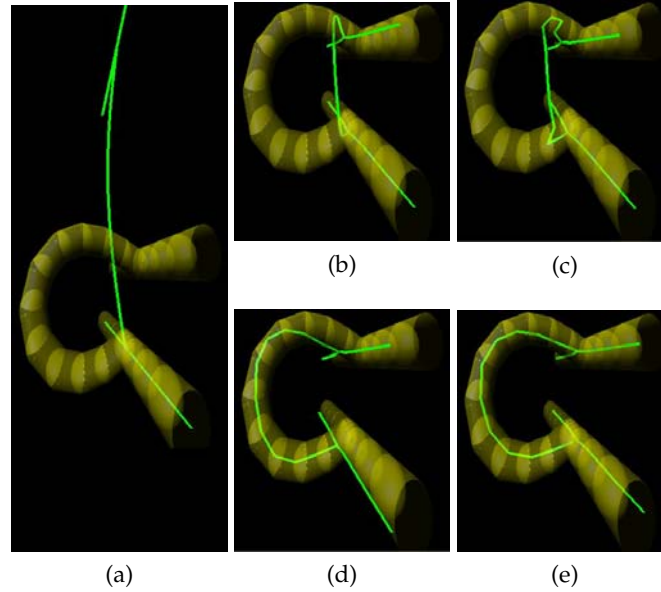


Figure 6.5.: An iteration of the 2D-3D deformable registration. In each figure the yellow transparent surface represents the ground truth, the green line represents the centerline of the deformed 3D graph. The 2D graph to which the 3D graph is to be registered is not shown. (a) input situation. The situation is shown after 85 (b), 1012 (c), 3674 (d), and 7670 (e) iterations. The typical values of $\alpha = 40$, $\beta = 20$, and $\gamma = 0.1$ have been chosen, μ was set to 0.001.

6.2.2. Tests on Synthetic Data

For these tests, we generate two 3D graphs by deforming the respective graph structures such that the length is preserved. One of the graphs serves as input for the method, while the other one presents the ground truth solution. The 3D ground truth is not directly used, but we generate a 2D projection of this structure, which is used as input for the method, together with the projection matrix and a correspondence set. For three exemplary data sets (Synth1, Synth2 and Synth3) quantitative and visual results are presented in Table 6.1 and Figure 6.8.

6.2.3. Real Data with Artificial Deformation

In order to assess the behavior of the method on natural vessel structures in a quantitative way, we deform the graphs extracted by segmentation from patient data sets with a length-preserving deformation function.⁴This way, we are able to perform our method and measure the distance of the result to a known ground truth in the same way as for synthetic data sets. A projection matrix computed from a rigid CTA-

⁴To this end, we employ a dedicated function, which is not used in our method itself, in order to assure the validity of comparison.

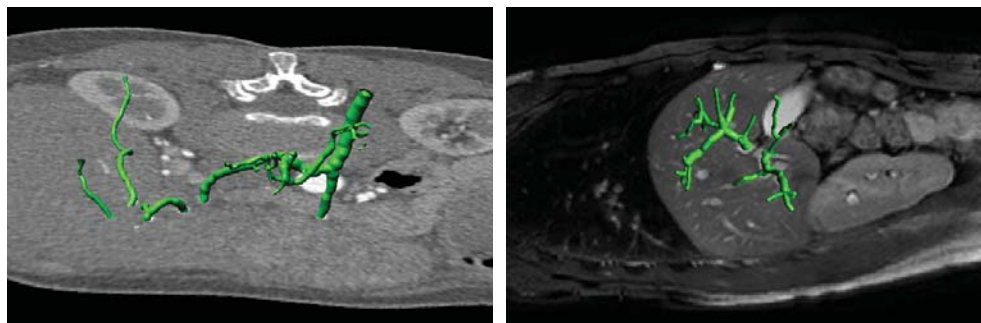


Figure 6.6.: Visualization of segmented real vessel structures. **Left:** Liver 1 data set (CTA) taken from a patient suffering from hepatocellular carcinoma. **Right:** Liver 2 data set (MRA) taken from Siebenthal *et al.* [151].

to-DSA registration of the respective patient is used to create the input 2D vessel graph. For the presented tests, we use a liver data set (Liver 1) from a patient who suffers from hepatocellular carcinoma and was treated with Transarterial Chemoembolization, compare Table 6.1 and Figure 6.6.

6.2.4. Real Data with Natural Deformation

Natural deformation fields for human organs are hard to obtain. In order to verify our method on possibly natural deformations we employ the results presented by Siebenthal *et al.* [151]. The displacement fields provided by this work are computed from a series of contrasted 4D MR images of the liver. A deformable registration is performed in [151] between the single 3D images, while the high time resolution together with the strong texture of the contrasted images assures the quality and reliability of the resulting deformation field. We segment the vessel structures from the contrasted MR images used in [151], and generate the input 3D graph for our method. Then, we apply the displacement field from [151] to the 3D graph and thus compute the ground truth for the result. A projection matrix yielding an anterior-posterior image was used for 2D input creation. In the same way as for the synthetic data sets, the 3D ground truth together with initial and deformed 3D input graph are used to quantitatively assess the performance of our method. Despite the small deformation observable in the data set (Liver 2), a clear improvement is achieved. Compare Table 6.1 and Figure 6.6.

6.2.5. Clinical Test

We performed a clinical test with known projection matrix and a “gold standard” deformation field for comparison. An important issue for the creation of this reference deformation field is the correspondence problem on vascular 3D graphs, which we address in an intuitive manner by resampling and length accumulation.

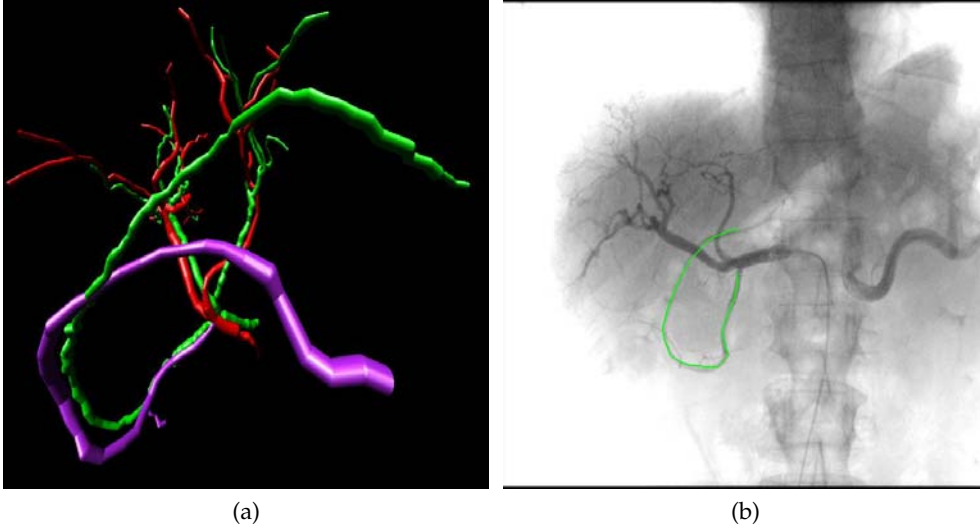


Figure 6.7.: Clinical Evaluation: (a) CTA and intraoperative reconstruction of vasculature rigidly registered. The purple vessel segment was used for the clinical test. A large deformation is observable in this vessel compared to the corresponding, intersecting green vessel. (b) Projection of vessel segment onto an intraoperative 2D image. The 2D image was used for the intraoperative 3D reconstruction and a projection matrix is known due to calibration.

We use two 3D graphs extracted from a preoperative CTA and an intraoperative cone-beam reconstruction of the same patient undergoing a liver catheterization. The intraoperative reconstruction is created from 395 views with projection matrices known from calibration. We first manually determine point correspondences of all bifurcation points visible in both data sets. Unlike sampling nodes on vessel segments, the location of bifurcations is well-defined at the junction of a vessel graph and hence correspondency can be established. We rigidly register the two resulting 3D point sets using the least-squares method of [147].

For computing a reference deformation field, we extract two vessel segments, $\Pi_{i,j}$ from the CTA graph and $\Pi'_{k,l}$ from the reconstruction graph that are manually determined to correspond. The chosen segment showed a large deformation, which was assessed after rigid 3D-3D registration (see Figure 6.7a). We now want to establish correspondency to all sampling nodes of $\Pi_{i,j}, \Pi'_{k,l}$ given an initial correspondence $\mathbf{B}_i \leftrightarrow \mathbf{B}'_k$.

The nodes on $\Pi_{i,j}, \Pi'_{k,l}$ cannot be assumed to have the same sampling since they have been extracted from two different data sets. Thus, we first apply a resampling to the segments to have an inter-node distance smaller than $0.8mm$. Then, we assign correspondences to the sampling nodes in the following way (without loss of generality we assume segment $\Pi_{i,j}$ to be shorter as $\Pi'_{k,l}$): For a node $\mathbf{X} \in \Pi_{i,j}$ determine its curve length to \mathbf{B}_i , $d(\mathbf{X}, \mathbf{B}_i)$. Walk through $\Pi'_{k,l}$ starting from \mathbf{B}'_k until the first node \mathbf{X}' has been found with $d(\mathbf{B}'_k, \mathbf{X}') \geq d(\mathbf{B}_i, \mathbf{X})$, which is assigned as corresponding

node to \mathbf{X} . This procedure is repeated for all nodes in $\Pi_{i,j}$.

With the set of correspondences $\{\mathbf{X}_h \leftrightarrow \mathbf{X}'_h\}$, $h = 1, \dots, n_\Pi$ we can compute a 3D Thin Plate Spline to align the two vessel segments $\Pi_{i,j}, \Pi'_{k,l}$. The resulting spline is used to deform $\Pi_{i,j}$ to $\tilde{\Pi}_{i,j}$. With this method we observed the difference in length of $\Pi_{i,j}$ and $\tilde{\Pi}_{i,j}$ to be smaller than 6%, additionally validating the assumption of length preservation.

As input for our registration method, we used $\Pi_{i,j}$, the segment $\pi'_{k,l}$ projected with matrix \mathbf{P}_{rec} , and the correspondence information of the 3D segments. \mathbf{P}_{rec} is taken from one of the views used for reconstruction and thus resembles the 2D intraoperative situation, compare Figure 6.7b.

A considerable improvement in Euclidean and shape error can be observed when applying our algorithm, despite the large deformation of the vessel segment, compare entries for Liver 3 in Table 6.1.

Test Type		Position Error [mm]		Shape Error [rad]	
Test	Data	μ	σ	μ	σ
Synth 1	Input	4.46	3.58	0.5847	0.7769
	Result	0.19 (95.8%)	0.05	0.0723 (87.6%)	0.0583
Synth 2	Input	1.36	1.09	0.3224	0.3628
	Result	0.22 (83.5%)	0.11	0.0254 (92.1%)	0.0192
Synth 3	Input	1.42	0.80	0.3463	0.1990
	Result	0.56 (60.3%)	0.37	0.1503 (56.6%)	0.1317
Liver 1	Input	7.38	2.23	0.1675	0.1676
	Result	3.25 (56.0%)	2.89	0.1106 (33.9%)	0.1277
Liver 2	Input	1.20	0.65	0.0082	0.0093
	Result	0.96 (19.7%)	0.74	0.0057 (30.3%)	0.0075
Liver 3	Input	14.88	15.01	0.2188	0.1672
	Result	7.57 (49.1%)	3.95	0.1824(16.6%)	0.1562

Table 6.1.: Results of error evaluation on several synthetic and real data sets. The position error by Euclidean distance, as well as the shape error by angle measurement is assessed. We give the mean error μ and in order to show the significance of the improvement also the standard deviation σ . For the mean, the relative improvement to the input data is given in percent. For visualization of the settings, compare Figures 6.7, 6.6, and 6.8.

6.3. Discussion

We presented a method for deformable registration of 3D vessel structures to a single 2D projection image. By combining a difference measure with constraints resulting from valid assumptions, we improve the rigid spatial alignment of the 3D vessel, which up to now presents the state of the art for this problem. The improvement in the spatial alignment is important for 3D depth perception and navigation during interventions. Quantitative and qualitative tests on medical and synthetic data sets clearly demonstrate the improvement achieved by our method.

In this chapter we consider the correspondency problem of vessel sampling points as well as the 2D-3D pose estimation problem to be solved before the application of

our method.

By using the regularizing \mathcal{S}_L and \mathcal{S}_S terms, we successfully account for the inherent ill-posedness of the problem, the unknown (and generally unsolvable) deformation in projection direction. However, an ambiguity remains since the length preservation constraint allows for two equally qualified solutions. Using a gradient-based optimization bends vessels towards the nearest solution. If we make the (valid) assumption that vessels surrounded by soft tissue undergo a deformation that is not inverting curvature, the optimization scheme drives the algorithm to the right solution. We can even reduce this assumption to allow for local curvature inversions. As can be seen in Figure 6.5c to 6.5e, the smoothing term handles such situations.

Further work will include improving the optimization methods for the presented model, automatic assessment of the model coefficients, and further testing of robustness with respect to missing and wrong correspondences.

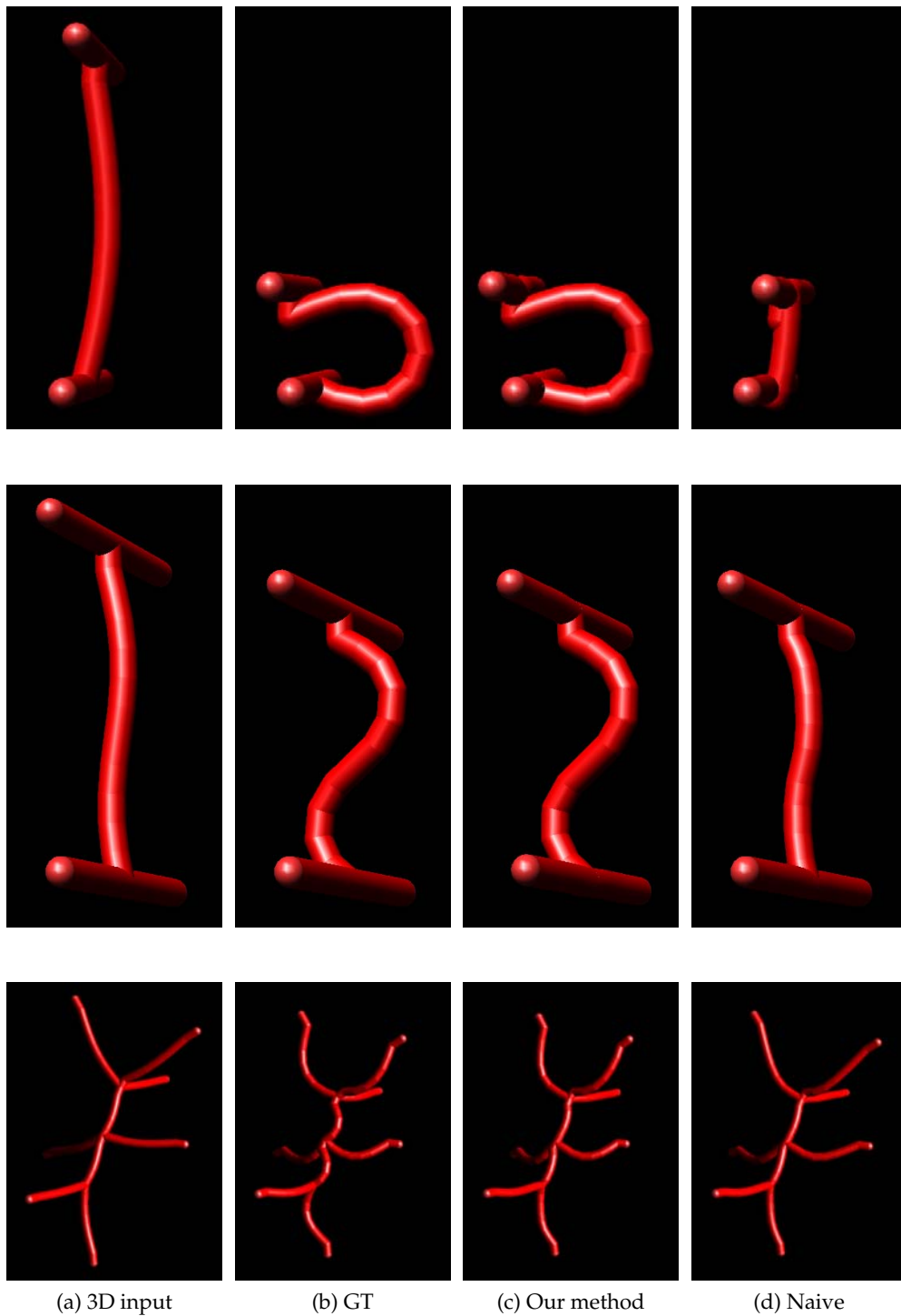


Figure 6.8.: Visualization of a selection of tests on synthetic data. Every row presents a single example setting, with the quantitative assessment of the results in Table 6.1 (from top to bottom: Synth 1, Synth 2, Synth 3).

7. Conclusion

Summary In this thesis, novel methods for the registration of angiographic 3D and 2D data sets have been successfully developed. We focused on liver catheterizations, in particular Transarterial Chemoembolizations as a frequently used treatment for liver tumors, where a fusion of CTA and DSA data can provide valuable information in terms of depth perception and intraoperative navigation. We introduced a new CTA protocol for liver artery visualization, developed two novel rigid registration algorithms, and proposed a method for deformable 2D-3D registration in a single-view scenario.

The introduction of a CTA protocol to visualize liver arteries allowed for a feature-based alignment, where the difficulties of vessel extraction, the correspondence problem in heterogeneous feature spaces, and non-rigid registration in a one-view scenario were overcome.

We conceived two rigid registration algorithms, which were tailored to be robust against segmentation errors, different contrast propagation, and deformation changes.

The *bifurcation-driven registration* restricted the feature space to ramification points of the underlying vessel structure and reduced the number of outliers by iterative graph extraction on projected centerline images. By combining this technique with topological information of the vessel graphs, a new distance function was developed that shows a good convergence rate on different patient data.

While the bifurcation-driven registration yields good results in many clinical cases, it also required a minimal amount of user interaction intraoperatively. Thus, we developed a second technique that performs fully automatic during the intervention. The *segmentation-driven registration* combines 2D DSA segmentation with 2D-3D pose estimation using a probability map in order to consequently discard false positives in the two vascular systems. This probability link, embedded in a Maximum Likelihood formulation, proved to be beneficial in terms of accuracy and robustness compared to hybrid methods, which avoid 2D segmentation. Since this enhanced feature space did not require an optimal segmentation, an automatic seed detection could be employed to provide an integration into intraoperative workflow without additional user interaction.

Last but not least, the refinement of a (sub-optimal) rigid vascular alignment in a non-rigid environment was addressed by the implementation of a *single-view 2D-3D deformable registration* algorithm. The minimization of an energy term based on the Euclidean distance between corresponding points was rendered well-posed by incorporating natural and mathematically valid constraints of length preservation and smoothness of local transformations. A 3D deformation field could be computed thus, where even the displacement in projection direction is captured, improving the results of rigid 2D-3D registration considerably.

7.1. Workflow Integration

For a clinical deployment of these registration algorithms, the fusion of pre- and intraoperative images has to be addressed. This includes not only an intuitive visualization of 3D vasculature or planning information, but also a propagation of the registration results to subsequent images that are acquired during the medical procedure. In the course of this work, we developed two visualization techniques that transfer information from CTA to DSA and vice versa. They will be discussed in section 7.1.1. For information propagation, we compensated for respiratory induced patient motion apparent in fluoroscopic image sequences. This issue is subject of section 7.1.2. We conclude with future work, which also addresses the difficult task of catheter tracking in fluoroscopic images.

7.1.1. Intraoperative Visualization

The result of 2D-3D registration can be used to improve visualization in the operating room. The fusion of preoperative information with intraoperative images or instrument locations can solve the problems of reduced depth perception and blind navigation. Basically, there are two possibilities to apply the information fusion: Either preoperative information is projected to enhance fluoroscopic images with vessel or roadmap information. A second way for visualization is to extract the current information from the 2D image (like catheter tip location) and backproject it to 3D using all information gained through the registration process. For both approaches we have developed visualization tools and acquired feedback from our clinical partners.

Catheter Guidance with Roadmap Projections For qualitative feedback on the registration accuracy and an improvement of treatment workflow through the 2D-3D alignment, we have shown two different techniques for 2D-3D projective visualization to our clinical partners: Direct volume rendering is used to project the registered 3D image and lay it over the current DSA image (see Figure 7.1a); a Multi-Planar Reconstruction (MPR) is used to display a 2D slice or a subvolume from the viewpoint of the C-arm on a second monitor (see Figures 7.1b and 7.1c).

According to physicians the 2D-3D overlay on one view does not improve 3D perception in the interventional room. The 3D volume is projected and, since the registration information is to be kept, should not be transformed and seen from any other viewpoint. Thus, the overlay is only giving additional 2D, but no 3D perception. The MPR visualization was favored because it resembles the rendering of orthogonal slices radiologists are used to from diagnostic procedures. Moreover, if shown on a second monitor, it does not influence the 2D DSA and can be used as general orientation whereas fine-grained navigation is done on fluoroscopic/DSA images. By showing different slices and/or MIPs of a subvolume a 3D perception can be created. Although “In-place” visualization of registered data is preferred when fusing different 3D data sets [143], our clinical partners believe that in the case of 2D-3D data fusion “Out-of-place” visualization proves to be the better choice.

In order to transfer previously planned information to the intraoperative setting, a simple planning tool was implemented that allowed physicians to create a 3D roadmap on the preoperative data before the intervention. After the registration process this roadmap can be projected onto the current DSA highlighting the vessel path the catheter should take to reach the tumor. We will refer to this method for planning and navigation as *roadmapping tool*.

With the roadmapping tool, an interventionalist can plan a procedure preoperatively on the CTA data by simply clicking on the vessel branch to be embolized (see Figure 7.1d). A shortest path is automatically calculated using the segmented vasculature's centerline. The path is followed to the main vessel by increasing vessel diameter. This roadmap can be visualized on the extracted 3D vasculature for orientation (Figure 7.1e) and projected with the registration parameters onto the current 2D image for improved catheter navigation (Figure 7.1f). This planning feature received very positive feedback from our clinical partners since navigation through the vessel system can be significantly improved by roadmap projection.

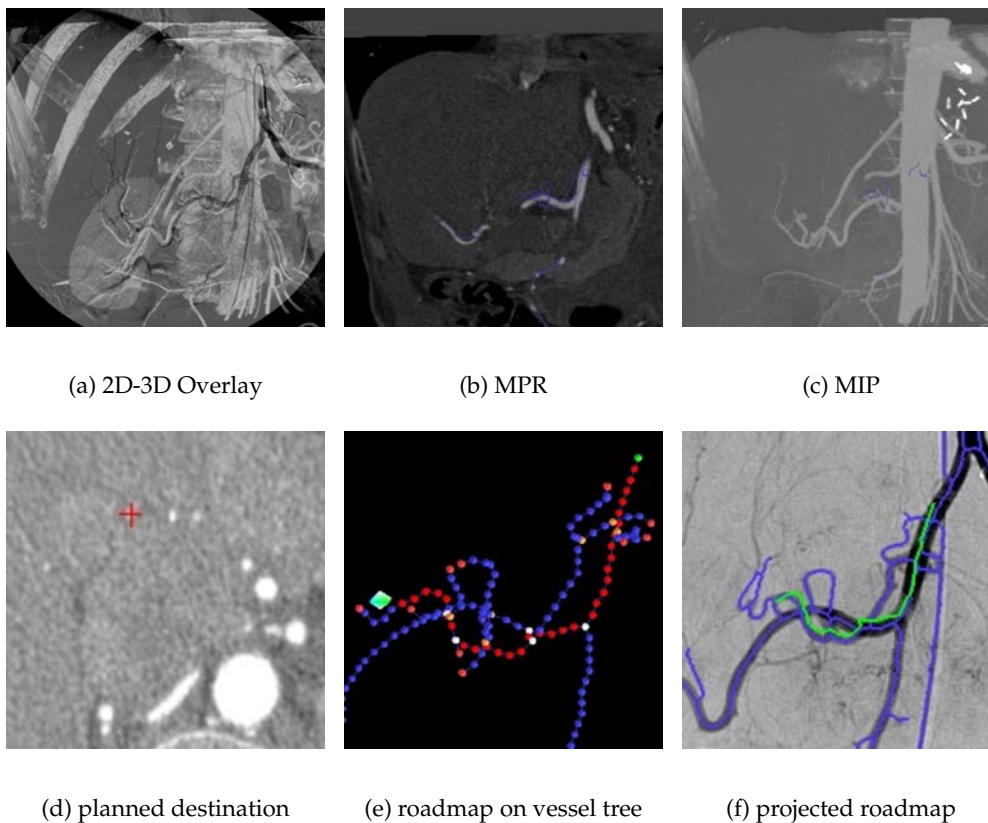


Figure 7.1.: Intraoperative Visualization and Navigation

Correspondence-Based 2D-3D Visualization For each vessel centerline point, the segmentation-driven 2D-3D registration can establish one-to-one correspondences, which can be used for catheter visualization on the 3D vessel model. If the catheter (tip) location is known in 2D, its location on the extracted 2D vasculature can be computed. For this, a simple closest point operator can be used assuming the catheter to lie in the vicinity of the 2D centerline graph. Thus, a tracking of the catheter in fluoroscopic image sequences (Figure 7.2a) allows physicians to have information about catheter location in the 2D vessel graph without additional contrast injection. Moreover, once correspondences have been determined by 2D-3D registration, this information can be provided in 3D (Figure 7.2b) and the viewpoint can be changed to improve depth perception (Figure 7.2c). Our clinical partners were particularly interested in this visualization technique if it was combined with a slice rendering of the CTA to allocate patient anatomy to the 3D vessel model, which is hard to interpret as stand-alone.

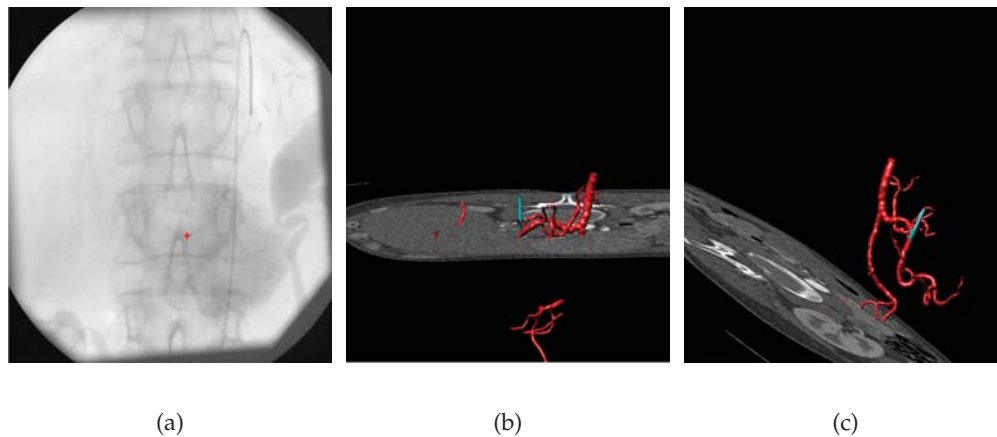


Figure 7.2.: Correspondence-based Visualization: (a) shows a catheter tip (red cross) in a fluoroscopic image. The vessel structure cannot be inferred here. (b) shows the catheter tip backprojected to the 3D vessel model (green arrow). Thus, vasculature, current catheter location, and patient anatomy can be assessed in 3D, (c) shows another viewpoint of the 3D vessel model. Since the correspondences have been previously established by 2D-3D registration, the transformation can be changed and depth perception is increased.

The correspondences determined by 2D-3D registration are not optimal in terms of outliers induced by ambiguities such as vessel overlay. An interpolation scheme can be introduced to reduce the sensitivity to outliers. If the previous 3D location of the catheter is known by tracking, the new location must not be located in another vessel of the vascular graph unless the last node of the vessel segment has been reached. If such a correspondence outlier has been detected, either the visualization can indicate

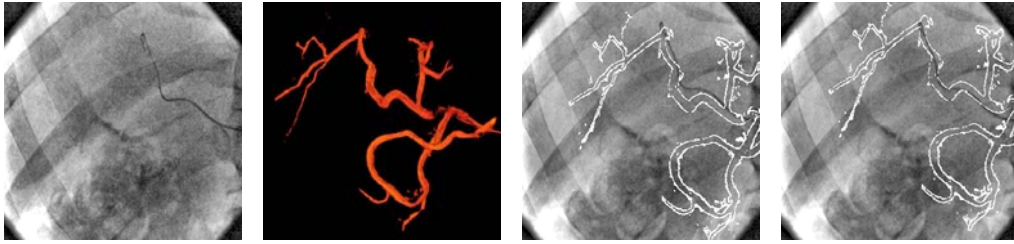


Figure 7.3.: (a) shows a 2D fluoroscopy image. (b) displays a projected roadmap of the hepatic arteries. (c) illustrates the projection of the contours of the projected roadmap onto the 23. frame in the 2D fluoroscopy image sequence. (d) indicates the projection of the roadmap onto 23. frame with motion correction.

it and stop, or an interpolation can be performed to move along the current vessel until a reliable correspondence is reached again.

We are also working on a method for uncertainty propagation to find the right 3D catheter tip location. It will be shortly summarized in 7.2.

For the realization of this visualization technique, a 2D catheter tracking is essential, which will also be addressed in 7.2.

7.1.2. Real-Time Breathing Correction

After the acquisition of a DSA image, with which a 2D-3D registration is performed, the interventionalist proceeds by navigating the catheter through the vascular system using fluoroscopic image sequences. These typically have a rate of 12-15 FPS, and catheter movement can be observed mainly induced by patient breathing and catheter advancement. Due to this motion, visualization driven by the previously computed registration is corrupted, i.e. projected roadmaps may be displaced from the current vessel, or backprojection of catheters might fail. For the visualization based on correspondences, the graph node in 2D nearest to the catheter tip has to be determined, which is hampered by this motion, too.

We account for this problem by compensating for the 2D motion induced by respiratory movement.

We propose a method for real-time estimation of the apparent 2D displacement of the hepatic arteries, which is illustrated in Figure 7.3 for roadmap projection. By *apparent displacement* we refer to the translational motion of the blood vessels projected onto the fluoroscopy image plane. However, in fluoroscopy images, the vessels and thus their motion is only visible, if the vessels are contrasted. Therefore, our approach approximates the displacement of the vessels by tracking the catheter motion in 2D fluoroscopy. A description of the entire tracking system including preliminary results is detailed in Appendix D. By updating the 2D-3D registration result this way, a realistic image fusion is achieved with respect to the current catheter position.

7.2. Future Work

Catheter Detection and Tracking The correspondence-based visualization provides a tool to visualize any location in a 2D vessel simultaneously in 3D. It would be desirable by clinicians to have information about the catheter, in particular its tip, in the 3D vascular tree. Thus, automatic catheter detection in 2D fluoroscopic images is important to fully integrate the benefits of 2D-3D registration into clinical workflow.

This detection is problematic due to the bad SNR of fluoroscopic images. Moreover, bone edges that are visible in these images sometimes have the same curvilinear shape as the catheter due to its small size (about 10 pixels in a 1024×1024 image). These false positives make extraction algorithms prone to error. Preliminary tests with a detector of curvilinear structures proposed by Steger [137] have not brought satisfactory results. An interesting work that will be followed in the future is the steerable tensor voting algorithm proposed by Franken *et al.* [49, 48]. A tensor filter is applied to images derived from Hessian analysis to detect a catheter in noisy fluoroscopic images.

If the catheter tip has been detected in a first image, its location has to be tracked in the following fluoroscopic frames and the tracking information has to be propagated to 3D. We are working on an integration of results coming from registration and motion compensation algorithms in order to predict the catheter tip location in 3D from subsequent fluoroscopic frames.

Given the catheter tip location \mathbf{x} in the last frame and a displacement \mathbf{d} in 2D computed with the apparent breathing correction method. On a sample set $\{\mathbf{y}_i\}$, $i = 1, \dots, n$ in the neighborhood of $\mathbf{x} + \mathbf{d}$ we can determine the CC value $CC(\mathbf{y}_i)$ in 2D. We get the corresponding points \mathbf{Y}_i in 3D through backprojection and closest point computation to the centerline points.

By randomly altering the rigid transformation parameters \mathbf{R}, \mathbf{t} for m times, we get new points \mathbf{Z}_{ij} together with energies \mathcal{E}_j for all the new poses. For all points \mathbf{Y}_i we can determine their covariance matrices weighted with the respective energies

$$\Lambda_i = \frac{1}{\sum_{j=1}^m \mathcal{E}_j^2} \sum_{j=1}^m \mathcal{E}_j (\mathbf{Z}_{ij} - \bar{\mathbf{Z}}_i)^\top (\mathbf{Z}_{ij} - \bar{\mathbf{Z}}_i), \quad (7.1)$$

where $\bar{\mathbf{Z}}_i$ is the weighted mean of \mathbf{Z}_{ij} , $j = 1, \dots, m$.

With these covariances, we can determine the *location of the most significant sample mode of the data* as described in [33]. By incorporating the CC values $CC(\mathbf{y}_i)$ from motion compensation, interpreted as probabilities, into the algorithm's weights w_i , we combine uncertainties of registration and motion compensation to yield the most probable 3D location of the catheter. For a thorough explanation of the algorithm and preliminary results on simulated data, refer to [10].

Application and Modalities Up to now, we have applied the registration algorithm to data coming from the TACE procedure. On the one hand, this data shows a great variability in terms of vessel shape and deformation making it suitable for algorithm evaluation. On the other hand, the applicability of the algorithms to other

vascular images, e.g. coming from a TIPS surgery, shall be evaluated in the future. The performance of the algorithms when applied to different vessel systems will be addressed. Moreover, the incorporation of different angiographic images will be tested. Instead of preoperative CTA images, MRA data can be used, and it has to be evaluated to which extent the extractable information suffices to compute the right registration. Intraoperatively, it has to be evaluated if contrasted 2D fluoroscopic images can also be used for the proposed methods (especially the segmentation-driven registration). If a detection of vessels in these images is successful despite the bad SNR and the small amount of contrast agent injected, the registration can be updated on the fly during the procedure. This could make breathing correction as well as catheter backprojection easier and more robust.

Tumor Visualization Integrating the tumor into the proposed visualization techniques is an issue that should be addressed for TACE procedures. This way, blood vessels are shown for navigation together with the target region to be reached. Several steps have to be realized for tumor visualization and fusion with catheter and vessel locations in 3D. Since the tumor is only visible in the arterial dominant phase of the CTA scan (see 4.4.1), it has to be registered to the angiographic phase of the CTA. This 3D-3D registration can be solved using intensity-based methods. Moreover, an adequate tumor visualization has to be developed. Direct volume rendering techniques will be rather difficult to maintain since tumor structures have a similar Hounsfield unit compared to surrounding tissue, even in the arterial dominant CTA scan. Thus, a tumor segmentation from CTA would be vital to successfully illustrate the tumor region.

Intraoperative 3D Imaging Since 3D imaging is provided by C-arms nowadays, fast 3D-3D registration of vascular structures will become more important. In this thesis, the 3D reconstruction data was used in the evaluation protocol of 2D-3D registration algorithms. However, since many hospitals use intraoperative reconstructions on a regular basis in vascular treatments, it should be promising to develop methods combining a 3D-3D registration with a 2D-3D refinement. The difficulty of deformation has been addressed by researches to align hepatic vessel systems for follow-up studies [4, 29]. However, the high difference of vessel structures due to local and global contrast injection poses an additional difficulty that is worth being addressed in the future.

Appendix

A. Practical Considerations on Images

Computer images are rasterized, i.e. spatial locations are sampled and intensity information is only available at discrete points called picture or volume elements (pixel/voxel):

$$\mathcal{I} : \mathbb{N}_0^d \rightarrow \mathbb{R} \quad (\text{A.1})$$

For simplicity, we will not use the term voxel, and indicate in the text if we address 2D, 3D, or ND images. We can arrange all the intensity values into a matrix (in 2D) \mathbf{A}_m^n or a tensor (in 3D) $\mathbf{T}_k^{n,m}$. Often, it is necessary to retrieve the intensity value between pixels, which can be achieved by *interpolation* from neighboring pixels.

The neighborhood of a pixel is defined over adjacent pixels. There exist several neighborhoods depending on dimension and integration of diagonally adjacent pixels. For example, a 4-neighborhood in a 2D image is defined as $\mathcal{N}_4(\mathbf{x}) = \{\mathcal{I}_{x-1,y}, \mathcal{I}_{x+1,y}, \mathcal{I}_{x,y-1}, \mathcal{I}_{x,y+1}\}$, where we placed the locations into the subscript for better readability. An 8-neighborhood is defined as

$$\mathcal{N}_8(\mathbf{x}) = \{\mathcal{I}_{x-1,y}, \mathcal{I}_{x+1,y}, \mathcal{I}_{x,y-1}, \mathcal{I}_{x,y+1}, \\ \mathcal{I}_{x-1,y-1}, \mathcal{I}_{x-1,y+1}, \mathcal{I}_{x+1,y-1}, \mathcal{I}_{x+1,y+1}\}.$$

A.1. Image Filtering

In a discrete setting *convolution* of two functions f, g is defined as:

$$(f * g)(m) = \sum_n f(n)g(m - n), \quad (\text{A.2})$$

Due to its frequent application (e.g. in linear scale-space), it is important to state how the Gaussian filter is created. Usually, we create a Gaussian kernel G_σ with standard deviation σ without evaluating the constant before $((2\pi\sigma^2)^N/2)$, but with a normalization factor

$$\hat{G}_\sigma(\mathbf{x}) = e^{-\|\mathbf{x}\|^2/2\sigma^2} \quad (\text{A.3})$$

$$G_\sigma(\mathbf{x}) = \frac{\hat{G}_\sigma(\mathbf{x})}{\sum_{x_1} \cdots \sum_{x_n} \hat{G}} \quad (\text{A.4})$$

Usually we create G_σ symmetric with mean zero, so if a filter size is given by h , we evaluate the kernel at positions $-(h-1)/2$ to $(h-1)/2$ in each direction. The filter size should also be adjusted to the chosen σ , a good trade-off between numerical relevance and accuracy is $h = 6 * \sigma$.

A.2. Image Derivatives

On discrete images, building the derivative is a filtering process. We can derive the image derivative from the difference quotient and image neighborhood. The quotient should include the surroundings in a symmetrical manner and should be as local as possible. For example, for a 2D image $\mathcal{I} : \mathbb{N}_0^2 \rightarrow \mathbb{R}$ we get:

- (1) First derivative: The simplest derivative filter is the central difference operator, i.e. the mask $[-1, 0, 1]$ filters the image in each dimension.

$$\frac{\partial \mathcal{I}_{x,y}}{\partial x} = \frac{\mathcal{I}_{x+1,y} - \mathcal{I}_{x-1,y}}{2h}, \quad (\text{A.5})$$

where h is the element spacing between adjacent pixel. The filtering in y is analogous.

- (2) Second derivative: Here, we derive two difference quotients and build their difference quotient. Since we want to be symmetric and local, we take the mask $[-1, 1]$ for first derivative and $[-1, 0, 1]$ for the second:

$$\begin{aligned} \frac{\partial^2 \mathcal{I}_{x,y}}{\partial x^2} &= ((-1) * \frac{\mathcal{I}_{x,y} - \mathcal{I}_{x-1,y}}{h} + (\frac{\mathcal{I}_{x+1,y} - \mathcal{I}_{x,y}}{h}))/h \\ &= \frac{\mathcal{I}_{x-1,y} - 2\mathcal{I}_{x,y} + \mathcal{I}_{x+1,y}}{h^2}. \end{aligned} \quad (\text{A.6})$$

$\frac{\partial^2 \mathcal{I}_{x,y}}{\partial y^2}$ is analogous. Mind that due to the minimality criterion, the difference quotient is taken at $x + \frac{1}{2}h$ and $x - \frac{1}{2}h$, thus we only have to divide by h instead of $2h$ for both derivation steps. The filtering in different direction is achieved by multiplying the central difference term to get a matrix filter:

$$[-1, 0, 1]^\top \begin{pmatrix} -1 \\ 0 \\ 1 \end{pmatrix}^\top = \begin{pmatrix} 1 & 0 & -1 \\ 0 & 0 & 0 \\ -1 & 0 & 1 \end{pmatrix} \quad (\text{A.7})$$

This assures symmetry again:

$$\frac{\partial^2 \mathcal{I}_{x,y}}{\partial x \partial y} = \frac{\mathcal{I}_{x-1,y+1} - \mathcal{I}_{x+1,y+1} - \mathcal{I}_{x-1,y-1} + \mathcal{I}_{x+1,y-1}}{4h^2} \quad (\text{A.8})$$

Since discrete differential operators are sensitive to noise, a Gaussian smoothing is usually applied together with derivation, whose implementation is described below together with linear scale-space.

A.3. Linear Scale-Space

Moving in linear scale-space is equivalent with applying a Gaussian filter with standard deviation σ to an image. If we want to build first and second derivatives in

scale-space, we can, due to the commutativity of filtering and derivation, build the filter derivative and convolve the image with the new filter:

$$\nabla \mathcal{I}_\sigma = G_\sigma * \nabla \mathcal{I} = \nabla G_\sigma * \mathcal{I}, \quad (\text{A.9})$$

and

$$\mathcal{H}_{\mathcal{I}_\sigma} = G_\sigma * \mathcal{H}_{\mathcal{I}} = \mathcal{H}_{G_\sigma} * \mathcal{I}. \quad (\text{A.10})$$

B. Thin Plate Splines

B.1. Special Spline Smoothing Problem

Given $\mathbf{x}(i) = (x_1(i), \dots, x_n(i))^\top \in \mathbb{R}^n$ and $y_i \in \mathbb{R}$, $i = 1, \dots, n$, and a data model

$$y_i = f(x_1(i), \dots, x_n(i)) + \epsilon_i, \quad (\text{B.1})$$

where $\epsilon_i \sim N(0, \sigma_i^2)$ represents measurement noise.

We want to solve the *special spline smoothing problem in n -dimensional Euclidean space*, i.e. we want to find the minimizing function f_λ to the variational problem

$$\frac{1}{n} \sum_{i=1}^n (y_i - f(x_1(i), \dots, x_n(i)))^2 + \lambda J_m^d(f), \quad (\text{B.2})$$

where $J_m^d(f)$ is defined as the thin-plate penalty functional on dimension d and derivation order m , e.g. for $d = 2, m = 2$

$$J_2(f) = \int_{-\infty}^{\infty} \int_{-\infty}^{\infty} (f_{x_1x_1}^2 + 2f_{x_1x_2}^2 + f_{x_2x_2}^2) dx_1 dx_2, \quad (\text{B.3})$$

or, for $d = 3, m = 2$

$$J_2(f) = \int_{-\infty}^{\infty} \int_{-\infty}^{\infty} (f_{x_1x_1}^2 + f_{x_2x_2}^2 + f_{x_3x_3}^2 + 2[f_{x_1x_2}^2 + f_{x_1x_3}^2 + f_{x_2x_3}^2]) dx_1 dx_2 dx_3. \quad (\text{B.4})$$

The solution f_λ to (B.2) is given by a combination of M monomial¹ coefficients and N radial function (RF) coefficients

$$f_\lambda(\mathbf{x}) = \sum_{\nu=1}^M d_\nu \phi_\nu(\mathbf{x}) + \sum_{i=1}^N c_i E_m(\mathbf{x}, \mathbf{x}(i)), \quad (\text{B.5})$$

where $\mathbf{x} = (x_1, \dots, x_n)^\top$, $\mathbf{x}(i) = (x_1(i), \dots, x_n(i))^\top$, and E_m is Green's function for the m -iterated Laplacian, (see Wahba 90 ([152]), p.30). f_λ is called the *Thin Plate Spline*.

Informally, E_m can be thought of as a radial function, i.e. a function whose response decreases (or increases) monotonically with distance from a central point (Orr 96 [110]).

The resulting spline f_λ has the following properties:

¹A monomial is a product of positive integer powers of a fixed set of variables, for example, x, xy^2 , or x^2y^3z . In this case they are of the order $< m$

- (1) *Natural Spline*: f_λ must be a *natural* spline, i.e. a spline f of odd degree $k = 2l - 1 (l \geq 2)$, which satisfies

$$f^{(l+j)}(a) = f^{(l+j)}(b) = 0, \quad j = 0, 1, \dots, l - 2 \quad (\text{B.6})$$

- (2) *Interpolating and Approximating Behavior*: If $\lambda = 0$ we have an interpolating behavior, i.e. for all measured points $\mathbf{x}(i), y_i : y_i = f_\lambda(\mathbf{x}(i)), i = 0, \dots, n$. If $\lambda \neq 0$ we have an approximating behavior, i.e. for all measured points $\mathbf{x}(i), y_i : y_i \approx f_\lambda(\mathbf{x}(i)), i = 0, \dots, n$, such that the SSD is minimized:

$$\min_f (y_i - f(x(i)))^2 \quad (\text{B.7})$$

- (3) *Existence of Squared Integral*: In order to fulfill the smoothness condition, the squared integral must exist, i.e.

$$\int_{-\infty}^{\infty} (f^{(m)}(t))^2 dt < \infty \quad (\text{B.8})$$

- (4) *Smoothness Condition*: The thin-plate penalty functional $J_m^d(f)$, the integral of squared derivatives of order m , must be minimized. Thus, the resulting spline is smooth (has low curvature).

B.2. Numerical Solution

We want to find the coefficients d_ν, c_i of f_λ . For that, we rewrite the equation as a system of linear equations in matrix-vector form. For each measurement $y_i \leftrightarrow \mathbf{x}(i)$ we write the constraints

$$y_i = \sum_{\nu=1}^M d_\nu \phi_\nu(\mathbf{x}(i)) + \sum_{j=1}^N c_j E_m(\mathbf{x}(i), \mathbf{x}(j)), \quad (\text{B.9})$$

in matrix-vector form

$$\mathbf{Kc} + \mathbf{Pd} = \mathbf{y} \quad (\text{B.10})$$

$$\mathbf{P}^\top \mathbf{c} = \mathbf{0}, \quad (\text{B.11})$$

where $\mathbf{K} \in \mathbb{R}^{N \times N}$, $K_{ij} = E_m(\mathbf{x}(i), \mathbf{x}(j))$ only consists of the radial functions evaluated at all measured \mathbf{x} -vectors $\mathbf{x}(i)$ (independent of y_i).

$\mathbf{P} \in \mathbb{R}^{N \times M}$, $P_{ij} = \phi_j(\mathbf{x}(i))$ accounts for the coefficients of the monomial part with all measured points $\mathbf{x}(i)$, and $\mathbf{y} = (y_1, \dots, y_n)$ are all measurements in the domain.

Equation (B.10) accounts for the constraints given by the function f_λ . Equation (B.11) accounts for the square integrability of f_λ , and simply forces the derivative of the elastic part of $f_\lambda, c_i E_m(\mathbf{x}, \mathbf{x}(i))^{(m)}$, to be 0 at infinity.

In the upper equations we require an **interpolation** behavior, i.e. $f(\mathbf{x}(i)) = y_i$. However, we have noisy measurement data and want to have an **approximation** behavior, i.e. $f(\mathbf{x}(i)) \approx y_i$, such that the sum of squared differences in equation (B.2) is minimized. This can be achieved by introduction of the regularization parameter λ into the numerical solution:

$$(\mathbf{K} + n\lambda\mathbf{W}^{-1})\mathbf{c} + \mathbf{P}\mathbf{d} = \mathbf{y} \quad (\text{B.12})$$

$$\mathbf{P}^\top \mathbf{c} = \mathbf{0}, \quad (\text{B.13})$$

where $\mathbf{W}^{-1} = \text{diag}(\sigma_1^2, \dots, \sigma_n^2)$ is the matrix of variances of the noise distribution of the measurements, or $\mathbf{W}^{-1} = \mathbf{I}$ if unknown.

Altogether, we have to solve for the vector $[\mathbf{c} \ \mathbf{d}]^\top$ in the system of linear equations

$$\begin{pmatrix} y_1 \\ y_2 \\ \vdots \\ y_n \\ 0 \\ \vdots \\ 0 \end{pmatrix} = \begin{bmatrix} \mathbf{K} + n\lambda\mathbf{W}^{-1} & \mathbf{P} \\ \mathbf{P}^\top & \mathbf{0} \end{bmatrix} \cdot \begin{bmatrix} \mathbf{c} \\ \mathbf{d} \end{bmatrix}, \quad (\text{B.14})$$

which can be accomplished using standard numerical solvers, e.g. the Singular Value Decomposition (SVD).

B.3. TPS for Feature-Based Deformable Registration

The TPS is particularly suitable for the task of feature-based deformable registration as introduced by Bookstein [15] for medical image registration and extensively studied by Rohr [126].

Given m points $\mathbf{X}_i = (x_{i1}, \dots, x_{in})^\top \in \mathcal{F}^A$ and $\tilde{\mathbf{Y}}_i = (y_{i1}, \dots, y_{in})^\top \in \mathcal{F}^B$ representing corresponding point features extracted from images \mathcal{A}, \mathcal{B} .

We want to find a transformation φ that minimizes the squared distance of all corresponding points. Moreover, we want the transformation to be sufficiently smooth, i.e. no folding or tearing should be introduced. Mathematically, we want to find φ , such that

$$\mathcal{E} = \sum_{i=1}^n \|\mathbf{X}_i - \varphi(\mathbf{Y}_i)\|^2 + \lambda \mathbf{J}_2(\varphi) \quad (\text{B.15})$$

is minimal. \mathbf{J}_2 is called the thin-plate penalty functional (see Equations (B.3) and (B.4)) and penalizes the curvature of the transformation φ in order to keep it smooth.

The TPS is given by $\varphi' = (\varphi'_1, \dots, \varphi'_n)^\top$, where φ'_i models an affine transformation part ($n + 1$ monomials), and a local deformation part (m radial functions):

$$\varphi'_i(\mathbf{X}) = a_0 + \sum_{j=1}^n a_j x_j + \sum_{k=1}^m w_k U(|\mathbf{X}_k - \mathbf{X}|), \quad (\text{B.16})$$

where a_0, \dots, a_n are the parameters controlling the affine part and w_1, \dots, w_m are the parameters controlling the local non-rigid part. These $n(n+1)$ affine and nm non-rigid parameters are determined from the point correspondences $\{\mathbf{X}_i \leftrightarrow \mathbf{Y}_i\}$. $U(\cdot)$ is a radial function and defined as $U(r) = r^2 \ln(r)$ in 2D and as $U(r) = |r|$ in 3D [146].

TPS registration has advantages and drawbacks. First, it can be computed on arbitrary points in space and retrieve a function with global support, i.e. the control points do not have to be uniformly distributed as for functions with local support, e.g., cubic B-splines [63]. Moreover, it is no mere interpolation scheme, but can be used as an approximation scheme, minimizing Equation (B.15) for all points in the image domains. Doing that, it also penalizes for high variations in curvature of the displacement field making sure that it transforms “sufficiently smooth”. And last, but not least, TPS are very easy to implement and, for a smaller number of control points, computationally efficient.

However, TPS-based registration is rather restricted. It cannot minimize other distance measures than mono-dimensional Euclidean, or Mahalanobis distance and thus always has to operate on point sets. Due to this rigidity of the formulation, it cannot be extended to 2D-3D deformable registration. Furthermore, it minimizes one particular smoothing term and cannot be extended to other, maybe more convenient smoothing terms without losing the theoretical minimizing property. The feature point correspondences (control points) have infinite support, i.e. all control points contribute to the deformation of other points. Thus, it is rather difficult to predict or change local behavior using TPS.

As mentioned in section 2.3.2, a local transformation should fulfill the properties of a diffeomorphism. Unfortunately, a TPS is no diffeomorphic mapping, but it can be extended to one as shown by Camion and Younes [24] in the form of *geodesic interpolating splines*. They have been successfully applied to Medical Image Analysis by Twining and Marsland [146].

C. Rotation Parameterization

C.1. Euler Angles

A minimal (and maybe the most intuitive) parameterization of a rotation matrix is given by three Euler angles, α, β, γ , representing the 3 DOF. These angles represent the rotations around the cartesian coordinate axes in 3D, i.e. x-, y-, and z-axis. The order of rotation is important to keep consistent, we choose the ZYX^1 order, i.e. first rotate around x-axis ($\mathbf{R}_x(\alpha)$), then around y-axis ($\mathbf{R}_y(\beta)$), finally around z-axis ($\mathbf{R}_z(\gamma)$):

$$\mathbf{X}' = \mathbf{R}_z(\gamma)\mathbf{R}_y(\beta)\mathbf{R}_x(\alpha)\mathbf{X}, \quad (\text{C.1})$$

where the respective rotation matrices are given by

$$\mathbf{R}_x(\alpha) = \begin{bmatrix} 1 & 0 & 0 \\ 0 & \cos \alpha & -\sin \alpha \\ 0 & \sin \alpha & \cos \alpha \end{bmatrix}, \quad \mathbf{R}_y(\beta) = \begin{bmatrix} \cos \beta & 0 & \sin \beta \\ 0 & 1 & 0 \\ -\sin \beta & 0 & \cos \beta \end{bmatrix},$$

$$\mathbf{R}_z(\gamma) = \begin{bmatrix} \cos \gamma & -\sin \gamma & 0 \\ \sin \gamma & \cos \gamma & 0 \\ 0 & 0 & 1 \end{bmatrix},$$

the multiplication of them gives the rotation matrix

$$\mathbf{R} = \begin{bmatrix} c\beta c\alpha & -c\gamma s\alpha + s\gamma s\beta c\alpha & s\gamma s\alpha + c\gamma s\beta c\alpha \\ c\beta s\alpha & c\gamma c\alpha + s\gamma s\beta s\alpha & -s\gamma c\alpha + c\gamma s\beta s\alpha \\ -s\beta & s\gamma c\beta & c\gamma c\beta \end{bmatrix}, \quad (\text{C.2})$$

where $c\alpha = \cos \alpha$, $s\alpha = \sin \alpha$, etc.

With this equation we can calculate a rotation matrix given three angles and vice versa.

C.2. Gimbal Lock

A singularity exists, known as *Gimbal Lock*, which is the ambiguity to determine angles α, γ if $\beta = \pm\pi/2$. In this case, the rotation matrix looks like

$$\mathbf{R}(\beta = \pi/2) = \begin{bmatrix} 0 & -c\gamma s\alpha + s\gamma c\alpha & s\gamma s\alpha + c\gamma c\alpha \\ 0 & c\gamma c\alpha + s\gamma s\alpha & -s\gamma c\alpha + c\gamma s\alpha \\ -1 & 0 & 0 \end{bmatrix}. \quad (\text{C.3})$$

¹read from right to left, since we do left-sided matrix multiplications

Using simple trigonometry, we get

$$\mathbf{R}(\beta = \pi/2) = \begin{bmatrix} 0 & \sin(\gamma - \alpha) & \cos(\gamma - \alpha) \\ 0 & \cos(\gamma - \alpha) & -\sin(\gamma - \alpha) \\ -1 & 0 & 0 \end{bmatrix}, \quad (\text{C.4})$$

which is a rotation with angle $\delta = \gamma - \alpha$. Since there are many combinations to get the same δ from γ and α , there is an ambiguity, which has to be considered when converting rotation matrices to α, β, γ . For $\beta = -\Pi/2$ there is an analogous calculation. As convention, in both cases ($\beta = \pm\Pi/2$) we choose $\alpha = 0$, thus resolving for this ambiguity.

C.3. Euler Angles in Rigid Registration

For the task of rigid registration, we usually alter the Euler angles and form a rotation matrix to transform an image or point. That is, the Euler representation of the rotation is changed during the (non gradient-based) optimization process, the rotation matrix just has to be built from the new parameters for energy term evaluation. In this direction, no ambiguity arises. Since we are never converting a rotation matrix to Euler angles in the registration process, only for visualization purposes, our results are not flawed by the Gimbal Lock.

If we use a gradient-based optimizer, the parameterization has to be used for building the first (and maybe second) derivative of the energy term. In this case, the ambiguity of Euler Angles is important and another parameterization of a rotation matrix should be used. Since all our rigid registration algorithms use a direct optimizer, which is not using the gradient of the energy term, we preferred the intuitive representation of rotations to a rotation reparameterization.

There are other representations of rotations, e.g. unit quaternions, or axis-angle representation (via the Rodriguez formula). However, these representations have four parameters and are constrained by vector unit length, while the minimal number of parameters for a rotation is three. Thus, if we run a parameter optimization, the parameter space increases by one, which might influence convergence rate and numerical stability of the registration.

Since we do not have to suffer from the Gimbal Lock (as the Computer Graphics community does) and since Euler Angles are minimal in terms of rotation parameterization, we use them throughout the thesis and discard other possible rotation parameterizations.

D. Real-Time Respiratory Motion Tracking

We propose a method for real-time estimation of the apparent 2D displacement of the hepatic arteries, which is illustrated in Figure 7.3 for roadmap projection. By *apparent displacement* we refer to the translational motion of the blood vessels projected onto the fluoroscopy image plane. However, in fluoroscopy images, the vessels and thus their motion is only visible, if the vessels are contrasted. Therefore, our approach approximates the apparent displacement of the vessels by tracking the catheter motion in 2D fluoroscopy. By updating the 2D-3D registration result this way, a realistic image fusion is achieved with respect to the current catheter position.

In the following, we will summarize the proposed method and show some preliminary results. A extensive study and more details on the numerical implementation to fulfill the real-time constraint are given in [3].

D.1. Method

D.1.1. Motion Model

Clifford *et al.* [32] present an extensive assessment of respiratory hepatic motion based on nine previously published studies. All studies agree that the most significant component of liver motion is cranio-caudal translation. There exists disagreement in the literature about the significance of liver motion in anterior-posterior and lateral directions. Recent studies, which follow the motion of single or multiple points within the liver volume, indicate that respiration causes significant translational motion along both of these axes, whereas earlier studies, which evaluate the motion of liver margins, suggest that clinically significant liver motion can be approximated effectively by cranio-caudal translation alone [32]. The tissue deformation caused by respiration is reported to be 3 mm on average. Rohlfing *et al.* [124, 125] estimate an average tissue deformation of 6-10 mm by comparison of rigid and non-rigid registration of the liver. However, they report that the rigid motion model i.e. translation and rotation accurately aligned the central area, while residual deformation occurs mostly in the periphery [32]. The same group reports that the rotations did not exceed 1.5 degrees. Considering these studies we approximate the apparent displacement of vessels due to respiration in 2D fluoroscopy images using a global translational model that covers translations in both x- and y-directions in the image plane. Our method does not account for local vessel deformations currently.

D.1.2. Approximation of Vessel Motion by Catheter Motion

As non-contrasted hepatic arteries are not visible in 2D fluoroscopy images, our approach approximates their apparent 2D respiratory displacement from catheter mo-

tion. Since the catheter is located within the vessels, its motion inevitably comprises the vessel motion. However, the catheter motion is further complicated by deformations. Because of the branched and elastic nature of the vessels a considerable deformation of the catheter occurs while being advanced by the interventional radiologist. For the robustness of the algorithm against these catheter deformations we propose an appropriate dynamic template update strategy.

D.1.3. Motion Tracking on Enhanced Images

Fluoroscopic images have a high SNR due to the low radiation dose used for acquisition. In order to enhance the catheter and suppress noise, a filtering is applied to the original fluoroscopy images. Regarding the width of a catheter, we apply a modified Marr-Hildreth filter, as proposed by Palti-Wasserman *et al.* [114].

After the filtering step the apparent 2D displacement of the catheter is estimated by template matching. Thereby, the displacement $\mathbf{d} = (d_x, d_y)$ of a structure between two frames is computed by defining a template \mathcal{T} in one frame containing this structure and by finding the region which matches it in the other frame \mathcal{I} with respect to a chosen similarity measure. Because of its robustness against noise and linear illumination changes we use the Correlation Coefficient (CC) as a similarity measure. For estimating the global translational motion we only consider a small part of the catheter, which has to contain both a vertical and a horizontal component in order to avoid the well-known aperture problem. In the initialization step of the tracking algorithm we ask the interventional radiologist to draw a small rectangle in the first frame covering such a part of the catheter. Then, a template matching is performed in a search region bigger than the largest expected translation induced by respiratory motion (up to 9mm in x- and 45 mm in y-direction, refer to Clifford *et al.* [32]). For tracking the motion between consecutive frames the search region is translated with the last computed displacement for each frame and the template matching is invoked in a smaller search region (up to 17 mm in x- and 25 mm in y-direction proved to be sufficient in our experiments). With this technique, the search region is kept small, which provides an acceleration in runtime of the algorithm and also decreases the probability of matching the catheter with other line-like structures such as bones. Moreover, the large influence of the catheter within the small template assures a reliable response of the CC for estimating the motion induced by breathing.

D.1.4. Dynamic Template Update

Using the same template for the entire intervention involves the assumption that the appearance of the catheter part contained in the template does not change over time. As the appearance of the catheter changes due to its deformation induced by the radiologist's movement, the algorithm will fail in general using only the template created from the first frame. In order to deal with possible catheter deformations we update the template if there is a considerable change in the structure contained in the template. We perform the template update if the difference between best CC values

of the initial and current frame becomes too large. As the new template we use the region that yields the maximum score of CC in the previous frame.

D.2. Results

The accuracy of the algorithm and its robustness against noise and catheter deformation is tested using both simulated and clinical image sequences.

D.2.1. Simulation Studies

In order to perform a quantitative analysis with a known ground truth, we generate image sequences by artificially superimposing a catheter onto real 2D fluoroscopy sequences of 15 frames. In these images, the catheter is manually removed and the corresponding region is inpainted by bilinear interpolation. By using clinical images and real catheter intensities, we assure that the simulated images are realistic (Fig. D.2.1). The position of the catheter is changed over the frames by a translation in y direction, which is to be corrected with our method. Starting with zero displacement, over the first 7 frames, the total displacement is increased by 4.8 mm between single frames, and in the second 7 frames, it is decreased by the same amount, resulting in a rough approximation of the respiratory motion visible in the images. This results in a maximal displacement of 33.6 mm. Using this setting, we perform two tests: one in which the added catheter is deformed, and a second, in which the robustness to noise is tested.

The accuracy of the algorithm in presence of catheter deformation is tested on the described sequence in 12 tests with different magnitudes of deformation (1.2-14.6 mm), resulting in a total of 180 simulated frames. To this end, the artificial catheter is deformed, before adding it to the background sequence. The deformation is performed by randomly moving 100 points of a free-form deformation (FFD) model based on cubic B-splines.

For all magnitudes of catheter deformation, the mean error of the computed displacements remains small (0.26-1.21mm).

The influence of noise is tested by adding different amounts of Gaussian noise to the sequence presented above in 10 tests, resulting in 150 simulated image frames. In this test, no deformation is added to the catheter. Note that the simulated images also contain the regular amount of signal dependent Poisson noise present in the X-ray beams, since they are created by manipulating clinical image sequences. By an additional Gaussian noise with variance of between 0.1% and 5% of the maximum image intensity (Fig. D.2.1) the mean error of the algorithm is between 0.00 mm and 0.89 mm.

D.2.2. Patient Studies

In order to evaluate the accuracy of the algorithm on real data we segment the catheter in 164 frames of a clinical image sequence and measure the fraction of catheter

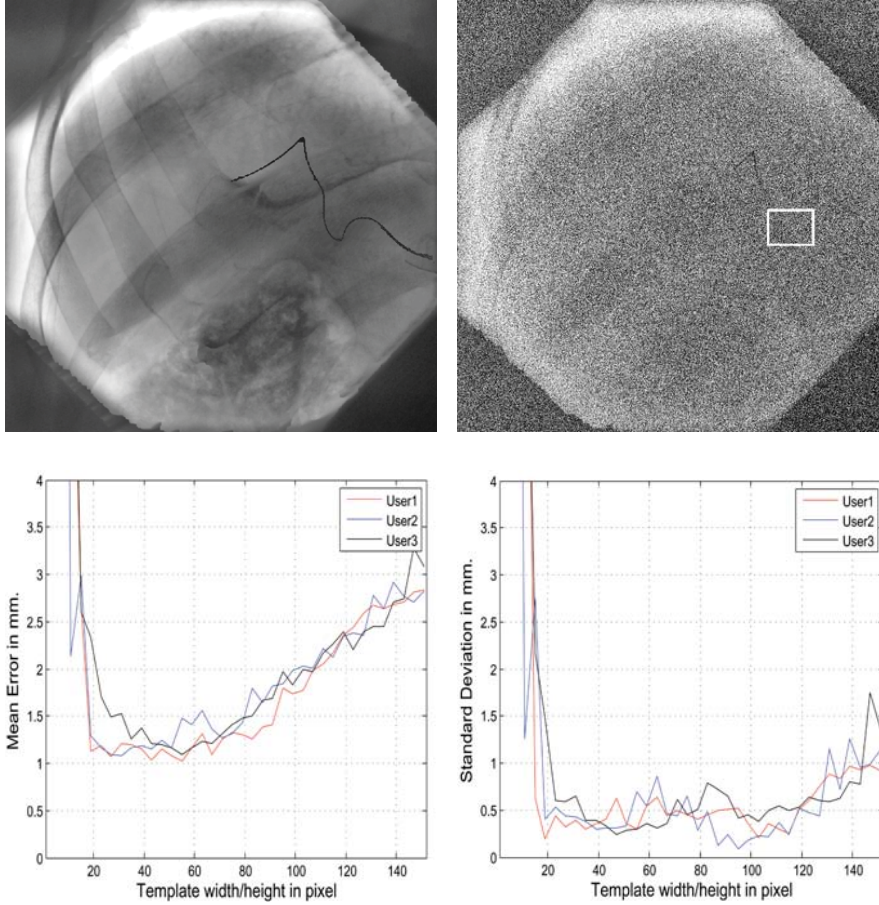


Figure D.1.: (a) shows a frame from a simulated image sequence with known catheter displacements. (b) displays the effect of additional Gaussian noise in the simulated image sequence, whereas the rectangular region is used as template by motion tracking. (c) and (d) illustrate the average and standard deviation of the error in patient data study with respect to template size.

contained in the vessel by computing $|N_C \cap N_R|/|N_C|$, with N_C and N_R being the segmented pixels of the catheter and the roadmap respectively. Our motion correction improves the catheter overlap from 36% to 70%. The influence of template size and location on the success of the algorithm is studied on 4 clinical fluoroscopy image sequences (with a total of 571 frames). For that, three inexperienced users select three points on the catheter for each sequence. Centered at each point 38 templates with different sizes between 3×3 pixels and 150×150 pixels are created. During the tests the size of the search region is set to the size of the template plus an extension in x and y direction of 20 and 40 pixels, respectively. The algorithm is then performed using each template. In the absence of an absolute ground truth, we compare the

results to the displacements determined by manually defined motion correction. For each user the average and standard deviation of the mean error over all frames is displayed in Fig. D.2.1 and D.2.1 respectively. The error in one frame is computed as $\|\mathbf{d}_e - (\mathbf{d}_{p_1} + \mathbf{d}_{p_2} + \mathbf{d}_{p_3})/3\|$, where \mathbf{d}_e denotes the expected displacement and \mathbf{d}_{p_1} , \mathbf{d}_{p_2} , \mathbf{d}_{p_3} denote the computed displacements using template centered at points p_1 , p_2 and p_3 , respectively. For all templates of size between 20×20 and 80×80 the error of the algorithm is in average 1.25 mm with a standard deviation less than 0.44 mm. Such an error is visually barely noticeable. and admissible for hepatic artery catheterizations. This study shows that the method still leads to near-optimal results for a large range of template sizes and for different template locations. Thus, we can conclude that the method does not require a precise template creation but involves just a simple user interaction, which is admissible for hepatic artery catheterizations as confirmed by our clinical partners.

E. List of Symbols

Energies

\mathcal{E}	the energy term
\mathcal{D}	the data term
\mathcal{S}	the regularization term

Graphs

G^d	a graph with node set V^d and edge set E^d , where d represents the spatial dimension of nodes in V^d . The graph consists of bifurcation points $\mathbf{B} \in V_b^d$ and sampling points $\mathbf{X} \in V_s^d$. $V^d = V_b^d \cup V_s^d$, $V_b^d \cap V_s^d = \emptyset$. Sampling nodes always have two neighbors, i.e. their degree is 2.
$\Pi_{i,j}$	a segment between two bifurcation nodes $\mathbf{B}_i, \mathbf{B}_j$, only consisting of sampling nodes and edges between them.
G^t	a topological graph, only consisting of bifurcation nodes and edges between them, i.e. $G^t = (V_b^d, E^t)$, where $E^t \subset V_b^d \times V_b^d$.

Images

\mathcal{I}	an image, i.e. an intensity mapping from a spatial domain to a real number $\Omega \rightarrow \mathbb{R}$
$\nabla \mathcal{I}$	the gradient of image \mathcal{I}
$\mathcal{H}_{\mathcal{I}}$	the Hessian matrix (second derivative) of image \mathcal{I}

Projections

\mathbf{P}	a projection matrix, i.e. a mapping from \mathbb{P}^3 to \mathbb{P}^2
\mathbf{K}	the calibration matrix of a pinhole camera
\mathbf{R}	a rotation matrix
\mathbf{t}	a translation vector
$f_{\mathbf{P}}$	a projection function, i.e. a mapping from \mathbb{R}^3 to \mathbb{R}^2 defined by the projection matrix \mathbf{P}

Statistics

X	a (multivariate) random variable
\mathcal{X}	a value of a (multivariate) random variable X
$P(\mathcal{X})$	the probability of random variable X having the value \mathcal{X} (abbreviation to $P(X = \mathcal{X})$)
$P(\mathcal{X} \mathcal{Y})$	the probability of random variable X having the value \mathcal{X} given that variable Y has the value \mathcal{Y} (abbreviation to $P(X = \mathcal{X} Y = \mathcal{Y})$)
$\mathcal{G}(\mu, \sigma)$	Gaussian distribution with mean μ and standard deviation σ
$G_{\sigma}(\mathcal{X})$	Gaussian distribution with zero mean and standard deviation σ evaluated at \mathcal{X} .

Transformations

φ	a transformation, which is usually a vector-valued function
$\nabla\varphi$	the first derivative of φ
\mathbf{J}_{φ}	the Jacobian matrix of φ . This is equal to the first derivative of φ , i.e. $\mathbf{J}_{\varphi} = \nabla\varphi$.
φ_i	the transformation at a particular point \mathbf{x}_i
Θ	a transformation parameter

Vectors and Matrices

\mathbf{x}	some 2D vector, i.e. $\mathbf{x} = (x, y)^\top$
\mathbf{X}	some 3D vector, i.e. $\mathbf{X} = (x, y, z)^\top$
$\hat{\mathbf{x}}$	a homogeneous 2D vector, i.e. $\hat{\mathbf{x}} = (x, y, w)^\top \in \mathbb{P}^2$
$\hat{\mathbf{X}}$	a homogeneous 3D vector, i.e. $\hat{\mathbf{X}} = (x, y, z, w)^\top \in \mathbb{P}^3$
\mathbf{M}	a matrix

F. List of Abbreviations

Medical Terms

HCC	Hepatocellular Carcinoma
ROI	Region of Interest
TACE	Transarterial Chemoembolization
TIPS	Transjugular Intrahepatic Portosystemic Shunt

Medical Imaging Modalities

CT	Computed Tomography
CTA	Computed Tomography Angiography
DSA	Digitally Subtracted Angiography
HU	Hounsfield Unit
MR	Magnetic Resonance (Imaging/Tomography)
MRA	Magnetic Resonance (Imaging/Tomography) Angiography
MRA TOF	MRA Time of Flight
MRA PC	MRA Phase Contrast
US	Ultrasound

Similarity Measures

CC	Correlation Coefficient
ECC	Entropy Correlation Coefficient
GD	Gradient Difference
GC	Gradient Correlation
MI	Mutual Information
NCC	Normalized Cross Correlation
PI	Pattern Intensity
SM	Similarity Measure
SSD	Sum of Square Differences

(Numerical) Algorithms

ART	Algebraic Reconstruction Technique
FBP	Filtered Back Projection
HSA	Hybrid Simulated Annealing
ICP	Iterative Closest Point
IIP	Iterative Inverse Perspective
LAP	Linear Assignment Problem
SVD	Singular Value Decomposition

Deformations

FFD	Free Form Deformation
TPS	Thin Plate Spline

Projections

CCS	Camera Coordinate System
DRR	Digitally Reconstructed Radiograph
MIP	Maximum Intensity Projection
WCS	World Coordinate System

Errors

PD	projection distance
RMSE	Root Mean Square Error
RPD	reprojection distance
TRE	target registration error

Miscellaneous

FPS	frames per second
GPU	Graphics Processing Unit
SNR	signal-to-noise ratio

G. List of Publications

International Journals

GROHER, M., JAKOBS, T.F., PADOY, N., AND NAVAB, N. Planning and Intraoperative Visualization of Liver Catheterizations: New CTA Protocol and 2D-3D Registration Method. *Academic Radiology* **14** (11), pp. 1324–1339, 2007.

NAVAB, N., AND GROHER, M. Novel Navigation and Advanced Visualization Techniques for Abdominal Catheterization. *Hospital Imaging and Radiology Europe* **2** (4), pp.29-30, 2008.

GROHER, M., ZIKIC, D., AND NAVAB, N. Deformable Registration of 3D Vessel Structures to a Single Projection Image. Submitted to *IEEE Transactions on Medical Imaging*.

International Conferences

UNGER, C., GROHER, M., AND NAVAB, N. Image Based Rendering for Motion Compensation in Angiographic Roadmapping. *IEEE Computer Society Conference on Computer Vision and Pattern Recognition (CVPR)*, Anchorage, USA, 2008.

ZIKIC, D., GROHER, M., KHAMENE, A., AND NAVAB, N. Deformable Registration of 3D Vessel Structures to a Single Projection Image. *SPIE Medical Imaging*, San Diego, USA, 2008.

ATASOY, S., GROHER, M., ZIKIC, D., GLOCKER, B., WAGGERSHAUSER, T., PFISTER, M., AND NAVAB, N. Real-Time Respiratory Motion Tracking: Roadmap Correction for Hepatic Artery Catheterizations. *SPIE Medical Imaging*, San Diego, USA, 2008.

GROHER, M., BENDER, F., HOFFMANN, R.T., AND NAVAB, N. Segmentation-Driven 2D-3D Registration for Abdominal Catheter Interventions. *Medical Image Computing and Computer-Assisted Intervention (MICCAI)* (2007), pp. 527-535.

GROHER, M., PADOY, N., JAKOBS, T.F., AND NAVAB, N. New CTA Protocol and 2D-3D Registration Method for Liver Catheterization. In *Medical Image Computing and Computer-Assisted Intervention (MICCAI)* (2006), pp. 873–881.

National Conferences

GROHER, M., HOFFMANN, R.T, ZECH, C.J., REISER, M., NAVAB, N. An Efficient Registration Algorithm for Advanced Fusion of 2D/3D Angiographic Data. *In Bildverarbeitung fuer die Medizin (BVM) (2007).*

KOENIG, L., GROHER, M., KEIL, A., GLASER, CH., REISER, M., NAVAB, N. Semi-Automatic Segmentation of the Patellar Cartilage in MRI. *In Bildverarbeitung fuer die Medizin (BVM) (2007).*

GROHER, M., JAKOBS, T.F., REISER, M., NAVAB, N. Advanced 2D-3D Registration Method for Transarterial Chemoembolizations. *5. Jahrestagung der Deutschen Gesellschaft für Computer-und Roboter-Assistierte Chirurgie (CURAC) (2006).*

GROHER, M., JAKOBS, T.F., PADOY, N., NAVAB, N. Towards a Feature-based 2D-3D Registration Method of CTA and 2D Angiograms for Liver Tumor Chemoembolizations. *4. Jahrestagung der Deutschen Gesellschaft für Computer-und Roboter-Assistierte Chirurgie (CURAC) (2005).*

BAUERNSCHMITT, R., SCHIRMBECK, E.U., GROHER, M., KEITLER, P., BAUER, M., NAJAFI, H., KLINKER, G., LANGE, R. Navigierte Platzierung endovaskulärer Aortenstents. *Z Kardiologie 93 S3: 116 (2004).*

Bibliography

- [1] ALPERIN, N., LEVIN, D. N., AND PELIZZARI, C. A. Retrospective registration of X-ray angiograms with MR images by using vessels as intrinsic landmarks. *Journal of Magnetic Resonance Imaging (JMRI)* 4 (1994), 139–144.
- [2] ALT, H., AND GODAU, M. Computing the Fréchet distance between two polygonal curves. *International Journal of Computational Geometry and Applications (IJCGA)* 5 (1995), 75–91.
- [3] ATASOY, S. Real-time respiratory motion tracking: Roadmap correction for endovascular interventions. Master's thesis, Technische Universität München, 2007.
- [4] AYLWARD, S., AND JOMIER, J. Rigid and deformable vasculature-to-image registration: A hierarchical approach. In *Proc. Int'l Conf. Medical Image Computing and Computer Assisted Intervention (MICCAI)* (2004), vol. 3216 of *Lecture Notes in Computer Science*, Springer, pp. 829–836.
- [5] AYLWARD, S., JOMIER, J., WEEKS, S., AND BULLITT, E. Registration and analysis of vascular images. *Int'l Journal of Computer Vision (IJCV)* 55 (2003), 123–138.
- [6] AYLWARD, S. R., AND BULLITT, E. Initialization, noise, singularities, and scale in height ridge traversal for tubular object centerline extraction. *IEEE Trans. on Medical Imaging (TMI)* 21, 2 (2002), 61–75.
- [7] BANSAL, R., STAIB, L. H., CHEN, Z., RANGARAJAN, A., KNISELY, J., NATH, R., AND DUNCAN, J. S. Entropy-based, multiple -portal-to-3DCT registration for prostate radiotherapy using iteratively estimated segmentation. In *Proc. Int'l Conf. Medical Image Computing and Computer Assisted Intervention (MICCAI)* (1999), *Lecture Notes in Computer Science*, Springer, pp. 567–578.
- [8] BELONGIE, S., MALIK, J., AND PUZICHA, J. Shape matching and object recognition using shape contexts. *IEEE Trans. Pattern Anal. Mach. Intell. (PAMI)* 24 (2002), 509–522.
- [9] BENAMEUR, S., MIGNOTTE, M., PARENT, S., LABELLE, H., SKALLI, W., AND DE GUISE, J. 3D/2D registration and segmentation of scoliotic vertebra using statistical models. *Computerized Medical Imaging and Graphics* 27 (2003), 321–337.
- [10] BENDER, F. Segmentation, 2D-3D registration, and uncertainty propagation for dynamic roadmapping in angiographic interventions. Master's thesis, Technische Universität München, 2007.

- [11] BESL, P. J., AND MCKAY, D. A method for registration of 3-D shapes. *IEEE Trans. Pattern Anal. Mach. Intell. (PAMI)* 14 (1992), 239–256.
- [12] BIRKFELLNER, W., SEEMANN, R., FIGL, M., HUMMEL, J., EDE, C., HOMOLKA, P., YANG, X., NIEDERER, P., AND BERGMANN, H. Fast DRR generation for 2D/3D registration. In *Proc. Int'l Conf. Medical Image Computing and Computer Assisted Intervention (MICCAI)* (2005), pp. 960–967.
- [13] BITTER, I., KAUFMAN, A., AND SATO, M. Penalized-distance volumetric skeleton algorithm. *IEEE Trans. on Visualization and Computer Graphics* 7, 3 (July-Sept. 2001), 195–206.
- [14] BLUM, H., AND NAGEL, R. N. Shape description using weighted symmetric axis features. *Pattern Recognition* 10, 3 (1978), 167–180.
- [15] BOOKSTEIN, F. L. Principal warps: Thin-plate splines and decomposition of deformations. *IEEE Trans. Pattern Anal. Mach. Intell. (PAMI)* 11 (1989), 567–585.
- [16] BORGEFORS, G. Distance transformations in digital images. *Comput. Vis., Graph., Image Processing* 34 (1986), 344–371.
- [17] BOUIX, S., SIDDIQI, K., AND TANNENBAUM, A. Flux driven automatic centerline extraction. *Medical Image Analysis* 9 (2005), 209–221.
- [18] BRONŠTEIN, I. N., SEMENDJAEV, K. A., MUSIOL, G., AND MÜHLIG, H. *Taschenbuch der Mathematik*, 5 ed. Deutsch, 2000.
- [19] BROWN, L. G. A survey of image registration techniques. *ACM Comput. Surv.* 24, 4 (1992), 325–376.
- [20] BROX, T., ROSENHAHN, B., AND WEICKERT, J. Three-dimensional shape knowledge for joint image segmentation and pose estimation. In *Pattern recognition : 27th DAGM Symposium* (2005), Lecture Notes in Computer Science, Springer, pp. 109–116.
- [21] BULLITT, E., LIU, A., AYLWARD, S., COFFEY, C., STONE, J., MUKHERJI, S., AND PIZER, S. Registration of 3D cerebral vessels with 2D digital angiograms: Clinical evaluation. *Academic Radiology* 6 (1999), 539–546.
- [22] BURT, P. Fast filter transforms for image processing. *Computer Vision, Graphics, and Image Processing* 16 (1981), 20–51.
- [23] BYRNE, V., COLOMINAS, C., HIPWELL, J., COX, T., NOBLE, J., PENNEY, G., AND HAWKES, D. Assessment of a technique for 2D-3D registration of cerebral intra-arterial angiography. *British Journal of Radiology* 77 (2004), 123–128.
- [24] CAMION, V., AND YOUNES, L. Geodesic interpolating splines. In *Proc. of the 3rd Int'l Workshop on Energy Minimization Methods in Computer Vision and Pattern Recognition (EMMCVPR)* (London, UK, 2001), Springer, pp. 513–527.

- [25] CAN, A., SHEN, H., TURNER, J., TANENBAUM, H., AND RAYSAM, B. Rapid automated tracing and feature extraction from retinal fundusimages using direct exploratory algorithms. *IEEE Transactions on Information Technology in Biomedicine* 3, 2 (1999), 125–138.
- [26] CASELLES, V., KIMMEL, R., AND SAPIRO, G. Geodesic active contours. *Int'l Journal of Computer Vision (IJCV)* 22, 1 (1997), 61–79.
- [27] CHAN, H., CHUNG, A., YU, S., AND WELLS, W. 2D-3D vascular registration between digital subtraction angiographic (DSA) and magnetic resonance angiographic (MRA) images. In *Proc. of the IEEE International Symposium on Biomedical Imaging* (2004), vol. 1205 of *Lecture Notes in Computer Science*, IEEE, pp. 708–711.
- [28] CHAN, T., AND VESE, L. Active contours without edges. *IEEE Trans. on Image Processing* 10, 2 (Feb. 2001), 266–277.
- [29] CHARNOZ, A., AGNUS, V., MALANDAIN, G., NICOLAU, S., TAJINE, M., AND SOLER, L. Design of robust vascular tree matching: validation on liver. In *Proc. Int'l Conf. Information Processing in Medical Imaging (IPMI)* (2005), vol. 3565 of *Lecture Notes in Computer Science*, Springer, pp. 443–455.
- [30] CHOI, Y., AND LEE, S. Injectivity conditions of 2D and 3D uniform cubic B-Spline functions. *Graphical Models* 62, 6 (2000), 411–427.
- [31] CHUI, H., AND RANGARAJAN, A. A new point matching algorithm for non-rigid registration. *Computer Vision and Image Understanding* 89 (2003), 114–141.
- [32] CLIFFORD, M., BANOVAC, F., LEVY, E., AND CLEARY, K. Assessment of hepatic motion secondary to respiration for computer assisted interventions. *Computer Aided Surgery* 7, 5 (2002), 291–299.
- [33] COMANICIU, D. Nonparametric information fusion for motion estimation. In *Proc. Conf. Computer Vision and Pattern Recognition (CVPR)* (2003), pp. 59–66.
- [34] CONDURACHE, A., AND AACH, T. Vessel segmentation in angiograms using hysteresis thresholding. In *9th IAPR Conference on Machine Vision Applications (MVA2005)* (Tsukuba, May 16–18 2005), IAPR (ISBN: 4-901122-04-5), pp. 269–272.
- [35] CONDURACHE, A., AACH, T., GRZYBOWSKI, S., AND MACHENS, H.-G. Vessel segmentation and analysis in laboratory skin transplant micro-angiograms. In *Proc. 8th IEEE Symposium on Computer-Based Medical Systems (CBMS)* (23-24 June 2005), pp. 21–26.
- [36] CROWLEY, J. L. *A Representation for Visual Information*. PhD thesis, Carnegie Mellon University, 1981.

- [37] DEMPSTER, A. P., LAIRD, N. M., AND RUBIN, D. B. Maximum likelihood from incomplete data via the EM algorithm. *Journal of the Royal Statistical Society. Series B (Methodological)* 39, 1 (1977), 1–38.
- [38] DESCHAMPS, T., AND COHEN, L. Fast surface and tree structure extraction of vascular objects in 3D medical images. In *Fifth International Conference on Curves and Surfaces* (Saint-Malo, France, June 2002), pp. 103–112.
- [39] DEY, J., AND NAPEL, S. Targeted 2D/3D registration using ray normalization and a hybrid optimizer. *Medical Physics* 33, 12 (2006), 4730–4738.
- [40] EBERLY, D. *Ridges in Data and Image Analysis*. Kluwer, 1996.
- [41] FELDMAR, J., AYACHE, N., AND BETTING, F. 3D-2D projective registration of free-form curves and surfaces. In *Proc. Int'l Conf. of Computer Vision (ICCV)* (1995), vol. 20-23, IEEE, pp. 549–556.
- [42] FISCHER, B., AND MODERSITZKI, J. Curvature based image registration. *Journal of Mathematical Imaging and Vision* 18, 1 (2003), 81–85.
- [43] FISHMAN, E. K. Cardiac CT: Where are we today and where are we going? *Applied Radiology Online (Supplement)* 35 (2006), 5–9.
- [44] FISHMAN, E. K., AND LAWLER, L. P. CT angiography: Principles, techniques and study optimization using 16-slice multidetector CT with isotropic datasets and 3D volume visualization. *Critical Reviews in Computed Tomography* 45 (2004), 355–388.
- [45] FLEUTE, M., AND LAVALLEE, S. Nonrigid 3-D/2-D registration of images using statistical models. In *Proc. Int'l Conf. Medical Image Computing and Computer Assisted Intervention (MICCAI)* (London, UK, 1999), Springer, pp. 138–147.
- [46] FRANGI, A., NIESSEN, W., HOOGEVEEN, R., VAN WALSUM, T., AND VIERGEVER, M. Model-based quantitation of 3-D magnetic resonance angiographic images. *IEEE Trans. on Medical Imaging (TMI)* 18, 10 (Oct. 1999), 946–956.
- [47] FRANGI, A. F., NIESSEN, W. J., VINCKEN, K. L., AND VIERGEVER, M. A. Multiscale vessel enhancement filtering. In *Proc. Int'l Conf. Medical Image Computing and Computer Assisted Intervention (MICCAI)* (1998), vol. 1496 of *Lecture Notes in Computer Science*, Springer, pp. 130–137k.
- [48] FRANKEN, E., RONGEN, P., VAN ALMSICK, M., AND TER HAAR ROMENY, B. M. Detection of electrophysiology catheters in noisy fluoroscopy images. In *Proc. Int'l Conf. Medical Image Computing and Computer Assisted Intervention (MICCAI)* (2006), vol. 4191 of *Lecture Notes in Computer Science*, Springer, pp. 25–32.

- [49] FRANKEN, E., VAN ALMSICK, M., RONGEN, P., FLORACK, L., AND TER HAAR ROMENY, B. M. An efficient method for tensor voting using steerable filters. In *Eurp'n Conference of Computer Vision (ECCV)* (2006), pp. 228–240.
- [50] FRIDMAN, Y., PIZER, S. M., AYLWARD, S., AND BULLITT, E. Extracting branching tubular object geometry via cores. *Medical Image Analysis* 8 (2004), 169–176.
- [51] GOLD, S., AND RANGARAJAN, A. A graduated assignment algorithm for graph matching. *IEEE Trans. Pattern Anal. Mach. Intell. (PAMI)* 18, 4 (1996), 377–388.
- [52] GONZALEZ, R. C., AND WOODS, R. E. *Digital Image Processing*. Prentice Hall, 2002.
- [53] GOOYA, A., LIAO, H., MATSUMIYA, K., MASAMUNE, K., AND DOHI, T. Effective statistical edge integration using a flux maximizing scheme for volumetric vascular segmentation in MRA. In *Proc. Int'l Conf. Information Processing in Medical Imaging (IPMI)* (2007).
- [54] GORGES, S., KERRIEN, E., BERGER, M.-O., TROUSSET, Y., PESCATORE, J., ANXIONNAT, R., AND PICARD, L. Model of a vascular C-Arm for 3D augmented fluoroscopy in interventional radiology. In *Proc. Int'l Conf. Medical Image Computing and Computer Assisted Intervention (MICCAI)* (2005), pp. 214–222.
- [55] GRANGER, S., AND PENNEC, X. Multi-scale EM-ICP: A fast and robust approach for surface registration. In *Proceedings of the 7th European Conference on Computer Vision-Part IV (ECCV'02)* (London, UK, 2002), Springer-Verlag, pp. 418–432.
- [56] GROCHOW, K., MARTIN, S. L., HERTZMANN, A., AND POPOVIC, Z. Style-based inverse kinematics. In *ACM Transactions on Graphics (Proc. of SIGGRAPH 2004)* (2004).
- [57] GROHER, M., BENDER, F., HOFFMANN, R., AND NAVAB, N. Segmentation-driven 2D-3D registration for abdominal catheter interventions. In *Proc. Int'l Conf. Medical Image Computing and Computer Assisted Intervention (MICCAI)* (2007), pp. 527–535.
- [58] GROHER, M., JAKOBS, T., PADOY, N., AND NAVAB, N. Planning and intraoperative visualization of liver catheterizations: New CTA protocol and 2D-3D registration method. *Academic Radiology* 14, 11 (2007), 1324–1339.
- [59] GROHER, M., PADOY, N., JAKOBS, T., AND NAVAB, N. New CTA protocol and 2D-3D registration method for liver catheterization. In *Proc. Int'l Conf. Medical Image Computing and Computer Assisted Intervention (MICCAI)* (2006), pp. 873–882.

- [60] HADAMARD, J. Sur les problèmes aux dérivées partielles et leur signification physique. *Princeton University Bulletin* (1902), 49–52.
- [61] HAJNAL, J., HILL, D., AND HAWKES, D., Eds. *Medical Image Registration*. CRC Press, 2001.
- [62] HAJNAL, J., HILL, D., AND HAWKES, D., Eds. *Medical Image Registration*. CRC Press, 2001, ch. Registration Methodology: Concepts and Algorithms, pp. 40–70.
- [63] HAJNAL, J., HILL, D., AND HAWKES, D., Eds. *Medical Image Registration*. CRC Press, 2001, ch. Non-Rigid Registration: Concepts, Algorithms and Applications, pp. 281–301.
- [64] HAMADEH, A., LAVALLE, S., AND CINQUIN, P. Automated 3-dimensional computed tomographic and fluoroscopic image registration. *Computer Aided Surgery* 3 (1998), 11–19.
- [65] HARALICK, B. M., LEE, C.-N., OTTENBERG, K., AND NÖLLE, M. Review and analysis of solutions of the three point perspective pose estimation problem. *Int'l Journal of Computer Vision (IJCV)* 13, 3 (1994), 331–356.
- [66] HARTLEY, R., AND ZISSERMAN, A. *Multiple View Geometry in Computer Vision*. Cambridge University Press, 2003.
- [67] HILL, D. L. G., MAURER, C. R., STUDHOLME, C., FITZPATRICK, J. M., AND HAWKES, D. J. Correcting scaling errors in tomographic images using a nine degree of freedom registration algorithm. *Journal of Computer Assisted Tomography* 22, 2 (1998), 317–323.
- [68] HIPWELL, J., PENNEY, G., MCLAUGHLIN, R., RHODE, K., SUMMERS, P., COX, T., BYRNE, J., NOBLE, J., AND HAWKES, D. Intensity based 2D-3D registration of cerebral angiograms. *IEEE Trans. on Medical Imaging (TMI)* 22 (2003), 1417–1426.
- [69] HORN, B., AND SCHUNK, B. Determining optical flow. *Artificial Intelligence* 17 (1981), 185–203.
- [70] JOMIER, J., BULLITT, E., VAN HORN, M., PATHAK, C., AND AYLWARD, S. 3D/2D model-to-image registration applied to TIPS surgery. In *Proc. Int'l Conf. Medical Image Computing and Computer Assisted Intervention (MICCAI)* (2006), pp. 662–670.
- [71] KAK, A. C., AND SLANEY, M. *Principles of Computerized Tomographic Imaging*. IEEE Press, 1999.
- [72] KASS, M., WITKIN, A., AND TERZOPOULOS, D. Snakes: Active contour models. In *Proc. Int'l Conf. of Computer Vision (ICCV)* (1988), pp. 261–268.

- [73] KERRIEN, E., BERGER, M.-O., MAURINCOMME, E., LAUNAY, L., VAILLANT, R., AND PICARD, L. Fully automatic 3D/2D subtracted angiography registration. In *Proc. Int'l Conf. Medical Image Computing and Computer Assisted Intervention (MICCAI)* (Sep 1999), vol. 1679 of *Lecture Notes in Computer Science*, Springer, pp. 664–671.
- [74] KERRIEN, E., VAILLANT, R., LAUNAY, L., BERGER, M.-O., MAURINCOMME, E., AND PICARD, L. Machine precision assessment for 3D/2D digital subtracted angiography images registration. In *Proc. SPIE Medical Imaging* (1998), vol. 3338, pp. 39–49.
- [75] KHAMENE, A., BLOCH, P., WEIN, W., SVATOS, M., AND SAUER, F. Automatic registration of portal images and volumetric CT for patient positioning in radiation therapy. *Medical Image Analysis* 10 (2006), 96–112.
- [76] KIRBAS, C., AND QUEK, F. A review of vessel extraction techniques and algorithms. *ACM Computing Surveys* 36, 2 (2004), 81–121.
- [77] KITA, Y., WILSON, D., AND NOBLE, J. Real-time registration of 3D cerebral vessels to X-ray angiograms. In *Proc. Int'l Conf. Medical Image Computing and Computer Assisted Intervention (MICCAI)* (1998), vol. 1496 of *Lecture Notes in Computer Science*, Springer, pp. 1125–1133.
- [78] KOENDERINK, J. J. The structure of images. *Biological Cybernetics* 50 (1984), 363–370.
- [79] KOLLER, T. M., GERIG, G., SZEKELY, G., AND DETTWILER, D. Multiscale detection of curvilinear structures in 2-D and 3-D image data. In *Proc. Int'l Conf. of Computer Vision (ICCV)* (1995).
- [80] KRISSIAN, K., MALANDAIN, G., AYACHE, N., VAILLANT, R., AND TROUSSET, Y. Model based detection of tubular structures in 3D images. *Computer Vision and Image Understanding* 80, 2 (2000), 130–171.
- [81] KRUGER, R. A. Image data acquisition, processing, storage and display. *Cardiovascular and Interventional Radiology* 6 (1983), 183–186.
- [82] LAM, L., LEE, S.-W., AND SUEN, C. Thinning methodologies—a comprehensive survey. *IEEE Trans. Pattern Anal. Mach. Intell. (PAMI)* 14, 9 (Sept. 1992), 869–885.
- [83] LANGE, T., WENCKEBACH, T., LAMECKER, H., SEEBASS, M., HÜNERBEIN, M., AND SCHLAG, P.-M. Registration of different phases of contrast-enhanced CT/MRI data for computer-assisted liver surgery planning. *Int'l Journal of Medical Robotics and Computer Assisted Surgery* 1 (2005), 6–20.
- [84] LASHOF, R. The tangent bundle of a topological manifold. *The American Mathematical Monthly* 79, 10 (December 1972), 1090–1096.

- [85] LEPETIT, V., LAGGER, P., AND FUA, P. Randomized trees for real-time key-point recognition. In *Proc. Conf. Computer Vision and Pattern Recognition (CVPR)* (2005).
- [86] LINDEBERG, T. *Scale-Space Theory in Computer Vision*. Kluwer, 1994.
- [87] LINDEBERG, T. Scale-space: A framework for handling image structures at multiple scales. In *CERN School of Computing* (1996).
- [88] LIU, A., BULLITT, E., AND PIZER, S. 3D/2D registration via skeletal near projective invariance in tubular objects. In *Proc. Int'l Conf. Medical Image Computing and Computer Assisted Intervention (MICCAI)* (1998), vol. 1496 of *Lecture Notes in Computer Science*, Springer, pp. 952–963.
- [89] LIVYATAN, H., YANIV, Z., AND JOSKOWICZ, L. Robust automatic C-Arm calibration for fluoroscopy-based navigation: A practical approach. In *Proc. Int'l Conf. Medical Image Computing and Computer Assisted Intervention (MICCAI)* (2002).
- [90] LORENSEN, W. E., AND CLINE, H. E. Marching cubes: A high resolution 3D surface construction algorithm. In *SIGGRAPH '87: Proceedings of the 14th annual conference on Computer graphics and interactive techniques* (New York, NY, USA, 1987), ACM Press, pp. 163–169.
- [91] LORENZ, C., CARLSEN, I.-C., BUZUG, T., FASSNACHT, C., AND WEESE, J. Multi-scale line segmentation with automatic estimation of width, contrast and tangential direction in 2D and 3D medical images. In *CVRMed-MRCAS* (1997), pp. 233–242.
- [92] LORIGO, L. M., FAUGERAS, O., GRIMSON, W. E. L., R.KERIVEN, KIKINIS, R., AND WESTIN, C. F. Co-dimension 2 geodesic active contours for MRA segmentation. In *IPMI* (1999).
- [93] LOWE, D. Distinctive image features from scale-invariant keypoints. *Proc. Int'l Conf. of Computer Vision (ICCV) 20* (2004), 91–110.
- [94] MADSEN, K., NIELSEN, H. B., AND TINGLEFF, O. *Methods for non-linear least squares problems* (2nd ed.), 2004.
- [95] MAINTZ, J., AND VIERGEVER, M. A survey of medical image registration. *Medical Image Analysis* 2, 1 (1998), 1–36.
- [96] MALANDAIN, G. *Filtrage, topologie et mise en correspondance d'images medicales multidimensionnelles*. PhD thesis, Ecole Centrale de Paris, 1992.
- [97] MALANDAIN, G., AND BERTRAND, G. Fast characterization of 3D simple points. In *Int'l Conf. on Pattern Recognition (ICPR)* (1992).

- [98] MANNIESING, R., VIERGEVER, M. A., AND NIESSEN, W. J. Vessel enhancing diffusion a scale space representation of vessel structures. *Medical Image Analysis* 10, 6 (2006), 815–825.
- [99] MARQUARDT, D. W. An algorithm for least-squares estimation of nonlinear parameters. *Journal of the Society for Industrial and Applied Mathematics* 11, 2 (1963), 431–441.
- [100] MCLAUGHLIN, R., HIPWELL, J., HAWKES, D., NOBLE, J., BYRNE, J., AND COX, T. A comparison of 2D-3D intensity-based registration and feature-based registration for neurointerventions. *Proc. Int'l Conf. Medical Image Computing and Computer Assisted Intervention (MICCAI)* 22, 11 (2002), 517–24.
- [101] MCLAUGHLIN, R. A., HIPWELL, J. H., HAWKES, D. J., NOBLE, J. A., BYRNE, J. V., AND COX, T. C. S. A comparison of a similarity-based and a feature-based 2-D-3-D registration method for neurointerventional use. *IEEE Trans. on Medical Imaging (TMI)* 24, 8 (2005), 1058–1066.
- [102] MEIJERING, E. *Image Enhancement in Digital X-Ray Angiography*. PhD thesis, University of Utrecht, the Netherlands, 2000.
- [103] MODERSITZKI, J. *Numerical Methods for Image Registration*. Oxford University Press, 2004.
- [104] NAIN, D., YEZZI, A., AND TURK, G. Vessel segmentation using a shape driven flow. In *Proc. Int'l Conf. Medical Image Computing and Computer Assisted Intervention (MICCAI)* (2004), Lecture Notes in Computer Science, Springer, pp. 51–59.
- [105] NAVAB, N., BEN-HASHEMI, A., MITSCHKE, M. M., HOLDSWORTH, D. W., FAHRIG, R., FOX, A., AND GRAUMANN, R. Dynamic geometrical calibration for 3d cerebral angiography. In *Proc. SPIE Medical Imaging* (1996).
- [106] NAVAB, N., AND GROHER, M. Novel navigation and advanced visualization techniques for abdominal catheterization. *Hospital Imaging and Radiology Europe* 2, 4 (2008), 29–30.
- [107] NELDER, J. A., AND MEAD, R. A. A simplex method for function minimization. *Computer Journal* 7 (1965), 308–313.
- [108] NICOLAU, S., PENNEC, X., SOLER, L., AND AYACHE, N. An accuracy certified augmented reality system for therapy guidance. In *Proc. of the 8th European Conference on Computer Vision (ECCV 04), Part III* (Prague, May 2004), vol. LNCS 3023, pp. 79–91.
- [109] OLABARRIAGA, S., BREEUWER, M., AND NIESSEN, W. Evaluation of hessian-based filters to enhance the axis of coronary arteries in CT images. In *Computer Assisted Radiology and Surgery (CARS)* (2003), pp. 1191–1196.
- [110] ORR, M. J. L. Introduction to radial basis function networks. Tech. rep., Centre of Cognitive Science, University of Edinburgh, 1996.

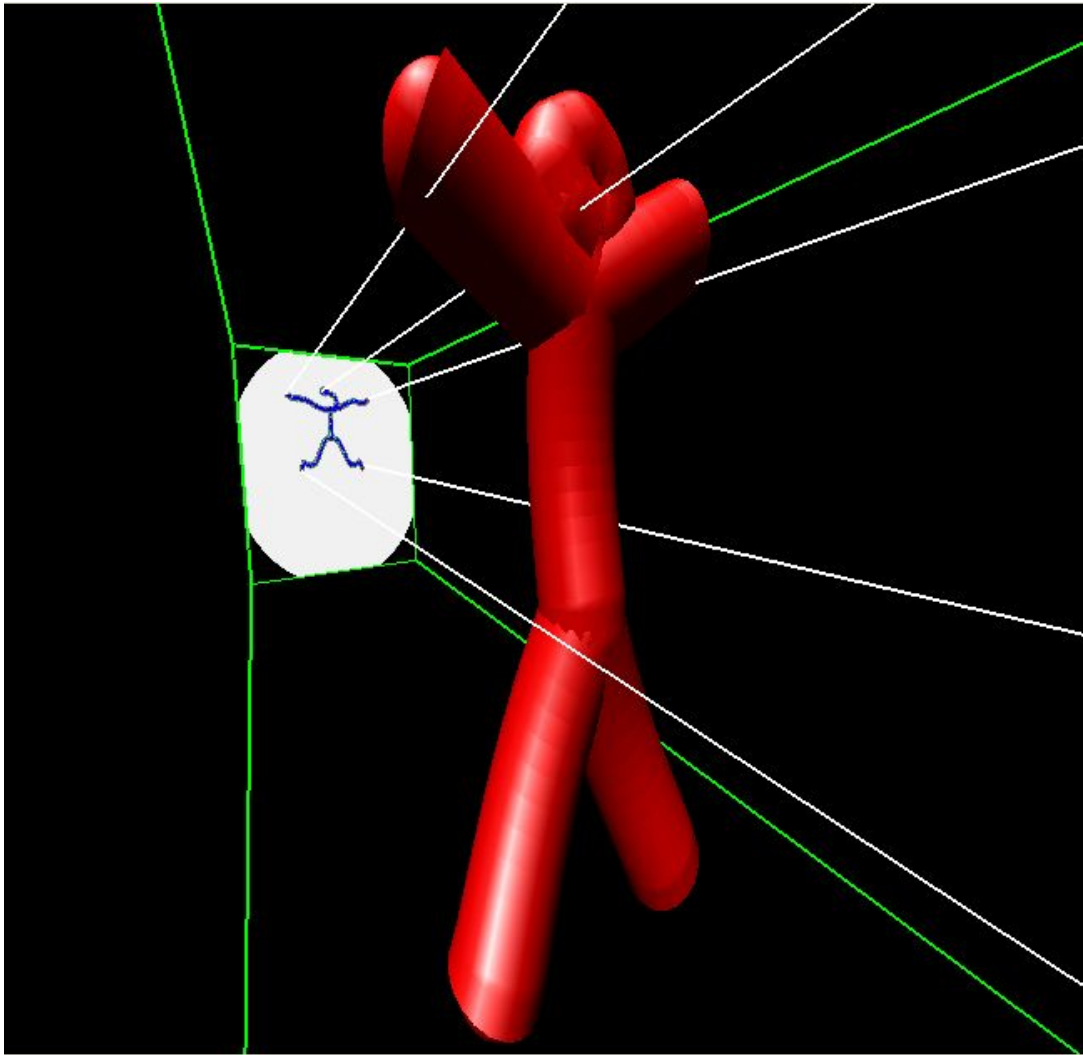
- [111] OSHER, S., AND SETHIAN, J. A. Fronts propagating with curvature-dependent speed: Algorithms based on Hamilton-Jacobi formulations. *Journal of Computational Physics* 79 (1988), 12–49.
- [112] PADOY, N. Hepatic vessel extraction for 2D/3D registration. Master's thesis, Technische Universität München, 2005.
- [113] PALÁGYI, K., SORANTIN, E., BALOGH, E., KUBA, A., HALMAI, C., ERDÖHELYI, B., AND HAUSEGGER, K. A sequential 3d thinning algorithm and its medical applications. In *Proc. Int'l Conf. Information Processing in Medical Imaging (IPMI)* (2001), vol. 2028 of *Lecture Notes in Computer Science*, Springer, pp. 409–415.
- [114] PALTI-WASSERMAN, D., BRUKSTEIN, A., AND BEYAR, R. Identifying and tracking a guide wire in the coronary arteries during angioplasty from x-ray images. *IEEE Trans. on Biomedical Engineering. (TBE)* 44, 2 (1997).
- [115] PAPADIMITRIOU, C., AND STEIGLITZ, K. *Combinatorial Optimization*. Prentice-Hall, Inc., Englewood Cliffs, NJ, 1982.
- [116] PENNEY, G., EDWARDS, P., KING, A., BLACKALL, J., BATCHELOR, P., , AND HAWKES, D. A stochastic iterative closest point algorithm (stochastICP). In *Proc. Int'l Conf. Medical Image Computing and Computer Assisted Intervention (MICCAI)* (2001), vol. 2208 of *Lecture Notes in Computer Science*, pp. 762–769.
- [117] PENNEY, G. P. *Registration of Tomographic Images to X-ray Projections for Use in Image Guided Interventions*. PhD thesis, University of London, 1999.
- [118] PENNEY, G. P., WEESE, J., LITTLE, J. A., DESMEDT, P., HILL, D. L. G., AND HAWKES, D. J. A comparison of similarity measures for use in 2D-3D medical image registration. *IEEE Trans. on Medical Imaging (TMI)* 17, 4 (1998), 586–595.
- [119] PERONA, P., AND MALIK, J. Scale-space and edge detection using anisotropic diffusion. *IEEE Trans. Pattern Anal. Mach. Intell. (PAMI)* 12 (1990), 629–639.
- [120] PHAM, D., XU, C., AND PRINCE, J. Current methods in medical image segmentation. *Annu. Rev. Biomed. Eng.* 2 (2002), 315–337.
- [121] PIZER, S. M., EBERLY, D., MORSE, B. S., AND FRITSCH, D. S. Zoom-invariant vision of figural shape: The mathematics of cores. *Computer Vision and Image Understanding* 69 (1998), 55–71.
- [122] POHL, K. M., FISHER, J., GRIMSON, KIKINIS, R., AND WELLS, W. M. A bayesian model for joint segmentation and registration. *NeuroImage* 31, 1 (May 2006), 228–239.
- [123] PRESS, W., TEUKOLSKY, S., VETTERLING, W., AND FLANNERY, B. *Numerical Recipes in C*. Cambridge University Press, New York, 1993.

- [124] ROHLFING, T., MAURER, C., O'DELL, W., AND ZHENG, J. Modeling liver motion and deformation during the respiratory cycle using intensity-based free-form registration of gated MR images. In *Proc. SPIE Medical Imaging* (2001).
- [125] ROHLFING, T., MAURER, C. R., O'DELL, W. G., AND ZHONG, J. Modeling liver motion and deformation during the respiratory cycle using intensity-based nonrigid registration of gated MR images. *Medical Physics* 31, 3 (2004), 427–432.
- [126] ROHR, K., STIEHL, H. S., SPRENGEL, R., BUZUG, T. M., WEESE, J., AND KUHN, M. H. Landmark-based elastic registration using approximating thin-plate splines. *IEEE Trans. on Medical Imaging (TMI)* 20, 6 (2001), 526–534.
- [127] RUECKERT, D., ALJABAR, P., HECKEMANN, R., HAJNAL, J., AND HAMMERS, A. Diffeomorphic registration using B-splines. In *Proc. Int'l Conf. Medical Image Computing and Computer Assisted Intervention (MICCAI)* (2006), pp. 702–709.
- [128] RUECKERT, D., SONODA, L., HAYES, C., HILL, D., LEACH, M., AND HAWKES, D. Nonrigid registration using free-form deformations: application to breast MR images. *IEEE Trans. on Medical Imaging (TMI)* 18, 8 (Aug. 1999), 712–721.
- [129] RUSSAKOFF, D. B., ROHLFING, T., RUECKERT, K. M. D., HO, A., ADLER, J. R., AND MAURER, C. R. Fast generation of digitally reconstructed radiographs using attenuation fields with application to 2D-3D image registration. *IEEE Trans. on Medical Imaging (TMI)* 24, 11 (2005), 1441–1454.
- [130] SALAZAR, R., AND TORAL, R. Simulated annealing using hybrid monte carlo. *Journal of Statistical Physics* 89, 5/6 (1997), 1047–1060.
- [131] SATO, Y., NAKAJIMA, S., ATSUMI, H., KOLLER, T., GERIG, G., YOSHIDA, S., AND KIKINIS, R. 3D multi-scale line filter for segmentation and visualization of curvilinear structures in medical images. *Medical Image Analysis* 2, 2 (1998), 143–168.
- [132] SCHAAP, M., SMAL, I., METZ, C., VAN WALSUM, T., AND NIESSEN, W. Bayesian tracking of elongated structures in 3D images. In *Proc. Int'l Conf. Information Processing in Medical Imaging (IPMI)* (2007).
- [133] SEIBERT, J. A. Flat-panel detectors: how much better are they? *Pediatric Radiology* 36, 2 (2006), 173–181.
- [134] SELLE, D., PREIM, B., SCHENK, A., AND PEITGEN, H.-O. Analysis of vasculature for liver surgery planning. *IEEE Trans. on Medical Imaging (TMI)* 21, 8 (2002), 1344–1357.
- [135] SHAPIRO, L., AND HARALICK, R. Structural descriptions and inexact matching. *IEEE Trans. Pattern Anal. Mach. Intell. (PAMI)* 3 (1981), 504–519.

- [136] SMYTH, J., SUTTON, D., AND HOUSTON, J. Evaluation of the quality of CT-like images obtained using a commercial flat panel detector system. *Biomedical Imaging and Intervention Journal* 2, 4 (2006), e48.
- [137] STEGER, C. An unbiased detector of curvilinear structures. *IEEE Trans. Pattern Anal. Mach. Intell. (PAMI)* 20, 2 (1998), 113–125.
- [138] STUDHOLME, C., LITTLE, J. A., PENNEY, G. P., HILL, D. L. G., , AND HAWKES, D. J. Automated multimodality registration using the full affine transformation: Application to MR and CT guided skull base surgery. In *Proc. 4th Int'l Conf. Visualization in Biomedical Computing (VBC'96)* (1996), pp. 601–606.
- [139] SURI, J. S., LIU, K., REDEN, L., AND LAXMINARAYAN, S. A review on MR vascular image processing algorithms: Acquisition and prefiltering: Part I. *IEEE Trans. on Information Technology in Biomedicine* 6, 4 (2002), 324–337.
- [140] SURI, J. S., LIU, K., REDEN, L., AND LAXMINARAYAN, S. A review on MR vascular image processing: Skeleton versus nonskeleton approaches: Part II. *IEEE Trans. on Information Technology in Biomedicine* 6, 4 (2002), 338–350.
- [141] TER HAAR ROMENY, B., Ed. *Geometry-Driven Diffusion in Computer Vision*. Kluwer Academic Publishers, 1994, ch. Linear Scale Space I: Basic Theory, pp. 1–38.
- [142] TOMAŽEVIČ, D., LIKAR, B., AND PERNUŠ, F. 3-D/2-D registration by integrating 2-D information in 3-D. *IEEE Trans. on Medical Imaging (TMI)* 25 (2006), 17–27.
- [143] TORY, M. Mental registration of 2D and 3D visualizations (an empirical study). In *Proceedings of the IEEE Visualization conference* (Seattle, Washington, USA, October 19-24 2003), p. 49.
- [144] TURBELL, H. *Cone-Beam Reconstruction Using Filtered Backprojection*. PhD thesis, Linköping University, Sweden, SE-581 83 Linköping, Sweden, February 2001. Dissertation No. 672, ISBN 91-7219-919-9.
- [145] TURGEON, G.-A., LEHMANN, G., GUIRAUDON, G., DRANGOVA, M., HOLDSWORTH, D., AND PETERS, T. 2D-3D registration of coronary angiograms for cardiac procedure planning and guidance. *Medical Physics* 32 (2005), 3737–3749.
- [146] TWINING, C. J., AND MARSLAND, S. Constructing diffeomorphic representations for the groupwise analysis of non-rigid registrations of medical images. *IEEE Trans. on Medical Imaging (TMI)* 23, 8 (2004), 413–425.
- [147] UMEYAMA, S. Least-squares estimation of transformation parameters between two point patterns. *IEEE Trans. Pattern Anal. Mach. Intell. (PAMI)* 13, 4 (1991), 376–380.

- [148] VAN DE KRAATS, E., PENNEY, G., TOMAZEVIC, D., VAN WALSUM, T., AND NIESSEN, W. Standardized evaluation methodology for 2-D-3-D registration. *IEEE Trans. on Medical Imaging (TMI)* 24, 9 (2005), 1177–1189.
- [149] VASILEVSKIY, A., AND SIDDIQI, K. Flux maximizing geometric flows. *IEEE Trans. Pattern Anal. Mach. Intell. (PAMI)* 24, 12 (2002), 1565–1579.
- [150] VERMANDEL, M., BETROUNI, N., PALOS, G., GAUVRIT, J.-Y., VASSEUR, C., AND ROUSSEAU, J. Registration, matching, and data fusion in 2D/3D medical imaging: Application to DSA and MRA. In *Proc. Int'l Conf. Medical Image Computing and Computer Assisted Intervention (MICCAI)* (2003), vol. 2878 of *Lecture Notes in Computer Science*, Springer, pp. 778–785.
- [151] VON SIEBENTHAL, M., SZÉKELY, G., GAMPER, U., BOESIGER, P., LOMAX, A., AND CATTIN, P. 4D MR imaging of respiratory organ motion and its variability. *Phys. Med. Biol.* 52 (February 2007), 1547–1564.
- [152] WAHBA, G. *Spline Models for Observational Data (C B M S - N S F Regional Conference Series in Applied Mathematics)*. Society for Industrial & Applied Mathematics, 1990.
- [153] WANG, S., ROSENFELD, A., AND WU, A. A medial axis transformation for grayscale pictures. *IEEE Trans. Pattern Anal. Mach. Intell. (PAMI)* 4, 4 (July 1982), 419–421.
- [154] WEICKERT, J., AND SCHNÖRR, C. A theoretical framework for convex regularizers in pde-based computation of image motion. *Int'l Journal of Computer Vision (IJCV)* 45, 3 (2001), 245–264.
- [155] WILSON, D., AND NOBLE, J. An adaptive segmentation algorithm for time-of-flight MRA data. *Medical Imaging, IEEE Transactions on* 18, 10 (Oct. 1999), 938–945.
- [156] WITKIN, A. Scale-space filtering. In *Int. Joint Conf. Artificial Intelligence* (Karlsruhe, West Germany, 1983), pp. 1019–1021.
- [157] WUNSCH, P., AND HIRZINGER, G. Registration of CAD-models to images by iterative inverse perspective matching. In *Intn'l Conf. on Pattern Recognition* (1996), vol. 1, pp. 78–83.
- [158] XU, C., AND PRINCE, J. L. Snakes, shapes, and gradient vector flow. *IEEE Transactions on Image Processing* 7 (1998), 359–369.
- [159] YAN, P., AND KASSIM, A. A. MRA image segmentation with capillary active contours. *Medical Image Analysis* 10, 3 (2006), 317–329.
- [160] YAO, J., AND TAYLOR, R. Assessing accuracy factors in deformable 2D/3D medical image registration using a statistical pelvis model. In *Proc. Int'l Conf. of Computer Vision (ICCV)* (Washington, DC, USA, 2003), IEEE Computer Society, p. 1329.

-
- [161] YAO, J., TAYLOR, R., GOLDBERG, R., KUMAR, R., BZOSTEK, A., VORHIS, R., KAZANZIDES, P., AND GUEZIEC, A. A C-Arm fluoroscopy-guided progressive cut refinement strategy using a surgical robot. *Computer Aided Surgery (CAS)* 5, 6 (2000), 373–90.
- [162] ZAHLTEN, C., JÜRGENS, H., AND PEITGEN, H.-O. Reconstruction of branching blood vessels from CT-data. In *Eurographics Workshop of Visualization in Scientific Computing* (1994), Springer, pp. 161–168.
- [163] ZHANG, Z. Iterative point matching for registration of free-form curves and surfaces. *Int'l Journal of Computer Vision (IJCV)* 13 (1994), 119–152.
- [164] ZIKIC, D. Variational deformable registration for medical applications. Master's thesis, Technische Universität München, 2006.
- [165] ZIKIC, D., GROHER, M., KHAMENE, A., AND NAVAB, N. Deformable registration of 3D vessel structures to a single projection image. In *Proc. SPIE Medical Imaging* (2008), in press.



The End.